



TECHNISCHE
UNIVERSITÄT
WIEN

DIPLOMARBEIT

Quantum dynamical screening of the local magnetic moment for different families of Fe-based superconductors

Ausgeführt am
Institut für Festkörperphysik
der Technischen Universität Wien

unter der Anleitung von:
Associate Prof. Dr. Alessandro Toschi
und:
Daniel Springer PhD.

durch

Clemens Watzenböck, BSc.
Matrikelnummer 01127685
Gilmgasse 3/17, 1170 Wien

Datum

Unterschrift

Abstract

We investigate the local magnetic susceptibilities of prototypical iron based superconductors. In particular we are interested to understand the impact of strong electronic correlations on the time-resolved dynamics of the local magnetic moment. We therefore study five materials (*LaFeAsO*, *BaFe₂As₂*, *LiFeAs*, *KFe₂As₂*, *FeTe*), all known to be Hund's metals, which strongly differ in their respective degree of correlation. The theoretical calculations are based on ab-initio DFT+DMFT calculations using maximally localized Wannier projections, both on the *d*- as well as the *dp*-model. The corresponding interaction parameters have been determined through constraint random phase approximation (cRPA). From our results we are able to identify and explain a material- and therefore correlation- dependent trend of the magnetic susceptibility. Our analysis of the time-resolved spin-correlation function provides the key to qualitatively disentangle different mechanisms governing the local spin dynamics of these systems. Moreover, our findings for the investigated compounds help to understand the origin of the mismatch between inelastic neutron scattering (INS) experiments and the ab-initio theoretical calculations.

Abstrakt in deutscher Fassung

Wir untersuchen die lokale magnetische Suszeptibilität von prototypischen eisenhaltigen Supraleitern. Dabei sind wir vor allem an dem Einfluss von starken Korrelationen auf die zeit-aufgelöste Dynamik des lokalen magnetischen Momentes interessiert. Darum haben wir fünf Materialien untersucht (*LaFeAsO*, *BaFe₂As₂*, *LiFeAs*, *KFe₂As₂*, *FeTe*), welche sich bekanntermaße als Hund-Metalle verhalten, und deren Korrelationsgrad stark materialabhängig ist. Die theoretischen Rechnungen basieren auf einer ab-initio lokale Dichteanäherung kombiniert mit einer dynamischen Molekularfeldtheorie (DFT+DMFT) Rechnung. Wobei sowohl maximal lokalisiert Wannier-Projektionen im *d*- als auch im *dp*-/*dpp*-Modell verwendet wurden. Die entsprechenden Wechselwirkungsparameter wurden durch eine (cRPA) Rechnung ermittelt. Ausgehend von unseren Resultaten waren wir in der Lage den material- und daher korrelations- abhängigen Trend der magnetischen Suszeptibilität zu identifizieren. Unsere Analyse der zeit-aufgelösten Spin-Korrelationsfunktion lieferte essentielle Informationen, um die Mechanismen hinter der Spindynamik qualitative zu entwirren. Unsere Erkenntnisse können außerdem dazu verwendet werden um den Unterschied zwischen den inelastischen Neutronen Streuexperimenten (INS) und ab-initio Rechnungen besser zu verstehen.

1	Introduction:	5
2	Theory and methods:	9
2.1	Quantum Field Theory in the context of Solid-State-Physics	9
2.2	Ab initio calculations: DFT + DMFT	11
2.2.1	Model-Hamiltonians in this thesis	14
2.3	Properties of Correlation-functions	16
2.3.1	Properties in imaginary time and Matsubara frequencies	16
2.3.2	Properties in real time and real frequencies	22
2.3.3	Special properties: Limiting cases	26
2.4	Analytical continuation	30
2.4.1	A first attempt	31
2.4.2	Maximum entropy method:	31
2.4.3	"Kink" selection criteria for α	32
2.4.4	Sparse modeling	35
3	Parameters and Assumptions for DFT+DMFT	37
3.1	Target orbitals $\epsilon^i(\vec{k})$	37
3.1.1	Filling n_0 :	40
3.2	Coulomb-overlap integrals (cRPA)	42
3.2.1	Average U , J and V	45
3.3	Double Counting Correction (DCC)	46
3.4	Temperature	47
4	Results: DMFT	49
4.1	<i>LaFeAsO</i>	49
4.1.1	One-particle-properties in the <i>d</i> -model	49
4.1.2	One-particle-properties in the <i>dpp</i> -model	52
4.1.3	Model comparison of the two-particle-properties: Spin-spin susceptibilities	54
4.1.4	Occupations and local magnetic momentum	59
4.2	<i>Ba₂Fe₂As</i>	62
4.2.1	One-particle-properties in the <i>d</i> -model	62
4.2.2	One-particle-properties in the <i>dp</i> -model	65
4.2.3	Model comparison of the two-particle-properties: Spin-spin susceptibilities	67
4.2.4	Occupations and local magnetic momentum	72
4.3	<i>LiFeAs</i>	76
4.3.1	One-particle-properties in the <i>d</i> -model	76
4.3.2	One-particle-properties in the <i>dpp</i> -model	78
4.3.3	Model comparison of the two-particle-properties: Spin-spin susceptibilities	80
4.3.4	Occupations and local magnetic momentum	85
4.4	<i>KFe₂As₂</i>	88
4.4.1	One-particle-properties in the <i>d</i> -model	88
4.4.2	One-particle-properties in the <i>dpp</i> -model	90
4.4.3	Model comparison of the two-particle-properties: Spin-spin susceptibilities	92
4.4.4	Occupations and local magnetic momentum	97
4.5	<i>FeTe</i>	100
4.5.1	One-particle-properties in the <i>d</i> -model	100
4.5.2	One-particle-properties in the <i>dpp</i> -model	102

4.5.3	Model comparison of the two-particle-properties: Spin-spin susceptibilities	104
4.5.4	Occupations and local magnetic momentum	110
5	Results: Comparison and discussion of Materials and Models	113
6	Conclusions and outlook	129

Chapter 1

Introduction:

Superconductivity (SC) is one of the most interesting phenomena in solid-state physics. Since its discovery in *Hg* at 4.183K by Heike Kamerlingh Owens in 1911 [1], it has been the dream of physicist to increase the superconductivity transition temperature, ideally towards the limit of room-temperature. Shortly after the initial discovery a vast number of other compounds were also found to be superconducting at very low-temperatures with $T_c < 30K$. The microscopic mechanism behind this phenomena of "conventional" superconductivity was explained, more than 40 years later, in 1957 by Bardeen, Cooper and Schrieffer (BCS) [2] in terms of an retarded electron-phonon coupling.

The discovery of superconductivity in cuprates in 1986 has unveiled a new class of superconductors [3] for which the theoretical explanation still remains highly controversial. In fact, while the BCS-theory, being a mean-field theory, can only be at a first glance "safely" applied to weakly correlated materials, the cuprates, are strongly correlated electron systems, challenge many of the theory and experimental old paradigms. posed a new challenge to theorist and experimentalists alike. Perhaps with an equally great surprise came with the discovery of unconventional SC in *iron-based superconductors* (Fe-SC) in 2006 [4]. This discovery was again breaking the common the common wisdom (or more correctly the one of the "Matthias rule" [5]) that magnetism was an antagonist of superconductivity: Especially compounds containing elements with *large local magnetic moments*, like *Fe*, were not to expected to experience SC.

While the phase-diagram of the iron-based SC looks strikingly similar to the cuprate phase diagram (see Fig. 1.1), it is quite unclear whether the physical origin of superconductivity is similar [6].

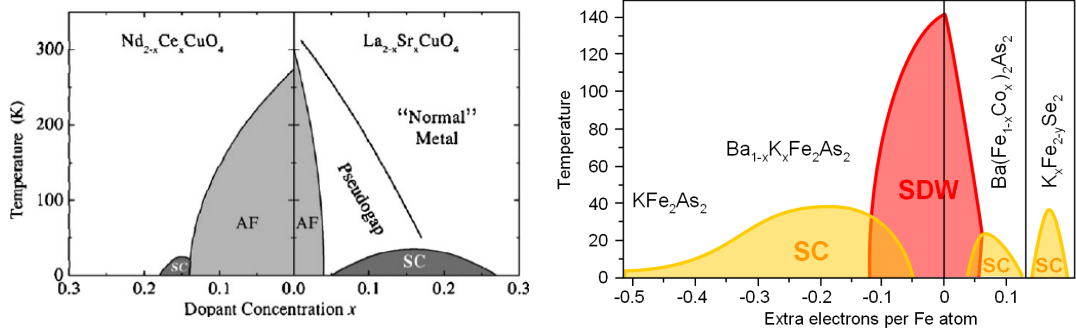


Figure 1.1: Generic phase diagrams for the cuprates [7] (left) and Fe -SC [8] (right).

In the case of the cuprates, SC appears when doping a Mott-insulating parent compound (vertical $x = 0$ line in the phase-diagrams above). For the materials of interest to this thesis, the Fe -SC, the situation is different: Superconductivity appears from doping an metallic spin-density-wave (SDW) parent-compound upon the superconducting regime. Above their Néel-temperature both classes of materials are paramagnetic. This clearly indicates an overall lower correlation level than the cuprates, which could have been associated to an easier theoretical treatment. This *not* the case, however, because of the pronounced multi-orbital nature of the Fe -based SC¹. The interplay of the (somewhat reduced) correlation process makes the theoretical description nevertheless rather challenging. In particular correlation effects might appear different at the one- and two-particle level. And, in fact, this poses theoretical and numerical challenges. At the one-particle level experimental evidence suggested that the local density approximation (LDA), is not completely off in describing the electronic structure of several Fe -SC. Nonetheless, angular-resolved-photo-emission spectroscopy (ARPES) measurements found a mass-enhance, for $LaFeAsO$, of about a factor of 2 compared to the LDA values. Correlation effects appear, however, much more strongly at the two-particle (2P) level. The spin-spin-susceptibility $\text{Im} \chi(\omega)$ measured in an inelastic neutron scattering (INS) experiment differs drastically from the values obtained by local (spin) density approximation L(S)DA. At the same time the spin-spin-susceptibility is, especially for the Fe -SC, a very important quantity. While unconventional high-temperature SC is (presently) not understood, it was pointed out that in Fe -SC, *spin-excitations may be responsible for electron pairing and superconductivity*[9].

The work of this master thesis is inspired by earlier calculations [10], where the spin-spin-susceptibility and the local magnetic moment was calculated for $LaFeAsO$ with an ab-initio local density approximation (LDA) plus dynamical mean field theory (DMFT) calculation. As it can be seen from $\text{Im} \chi(\omega)$ in their work, reproduce in Fig. 1.2, a large peak appears in $\text{Im} \chi(\omega)$ at $\omega \approx 0.2\text{eV}$. The presence of such a peak was associated to the formation of a local, strongly fluctuating magnetic moment in an itinerant background, well described by the term *Hund's metal*[11].

¹For example in $LaFeAsO$ one of the prototypical Fe -SC, 4 of the 5 d -orbitals are close to the Fermi-energy and very close in energies (with an overall crystal-field of few meVs).

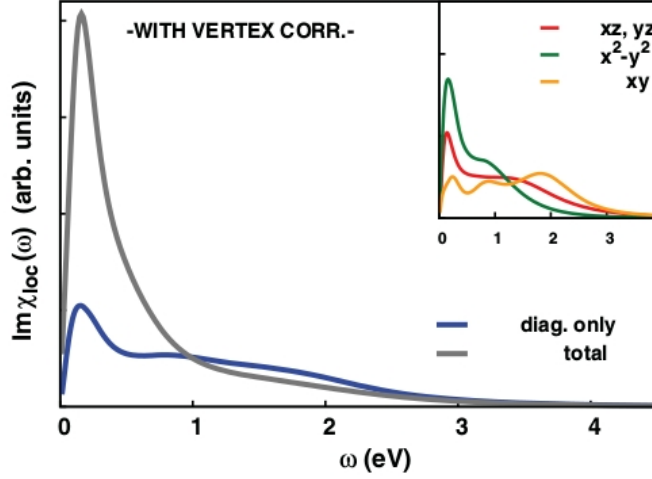


Figure 1.2: Local magnetic spin-susceptibility for $LaFeAsO$ (LDA+DMFT calculation). The graph is reproduced from [10].

In this earlier work, however, many additional approximations were made (consistently with the state of the art of algorithmic developments) a simplified 4-orbital model was used for the Wannier-projections[12], with density-density-type interaction for the DMFT part. This had limited the previous analysis to the less correlated case of $LaFeAsO$, where these approximations could be somewhat justified. In the meantime, *Quantum Monte Carlo* (QMC) solvers for DMFT problems have improved drastically. This allows us to extend the previous works to more complicated models (5-orbitals) and interaction Hamiltonians (SU(2) symmetric). These algorithmic improvements allow to study not only $LaFeAsO$, but also prototypical examples for the different classes ("families") of $Fe-SC$.

The families of Fe-based SC: Although a vast number of $Fe-SC$ is known today, their parent compounds can be classified by only seven types of crystalline structures (description and classification from [8]). We refer to them in the following as *families* of $Fe-SC$.

- 1111-type materials ($LnFePnO$, Ln: lanthanide, Ae $FeAsF$, Ae: alkaline earth, Pn: P , As)
- 122-type materials (AFe_2Pn_2 , AE: alkaline earth (alkali metal, Eu))
- 111-type materials ($AFePn$, A: alkali metal)
- 11-type materials ($Fe_{1+x}Ch$, Ch: Se , Te)
- Materials with thick blocking layer (32522-type ($AE_3M_2O_5Fe_2Pn_2$, M: Al , Sc)) (42622-type ($AE_4M_2O_6Fe_2Pn_2$, M: Sc , V , Cr)) (homologous type ($Ca_{n+1}Sc_nO_yFe_2As_2$: n=3, 4, 5))
- Materials containing additional arsenic ($Ca_{1-x}La_xFeAs_2$) ($Ca_{10}(M_4As_8)(Fe_2As_2)_5$, (M: Pr , Ir))

- 245-type materials ($A_{1-x}Fe_{2-y}Se_2$: $A=K, Cs, Rb, Tl$)

In this thesis we will focus especially on the first four families, since more experimental data is available for these classes. We chose for our theoretical analysis representative candidates from these four families. From the 1111-family we chose consistent with the previous work, $LaFeAsO$, the prototypical 1111-material. From the 122-family we chose $BaFe_2As_2$ and KFe_2As_2 . Notice that later is technical not a parent compound, but a 122-material with 100% doping of K . For the 111-family we chose $LiFeAs$ and for the 11-family, the simplest lattices structure, we chose $FeTe$. The choice of $BaFe_2As_2$ from the 122-family is especially promising with respect to a comparison to experiment, since the local-spin-susceptibility has been measured by means of INS experiments up to 400meV[13].

Quantum fluctuations and the *big moment* puzzle: While for the other materials no INS-experiments up to a comparable energy-ranges are currently available, measurements of the local magnetic moment are given in there literature. The results depending on the material in question, ranging from 0.3-0.6 μ_B ($LaFeAsO$)[14][15] via 0.9 μ_B ($BaFe_2As_2$)[16] up to 2.2 μ_B ($FeTe$)[14]. These are in contrast to LSDA predictions of $\approx 2\mu_B$, almost independent from the material[10]. A solution for this "*big moment puzzle*" was put forward in [10], for $LaFeAsO$ in terms of *quantum dynamical screening* of the local moment on Fe . It was, however, not possible at the time to verify if the proposed solution could really work, because the calculations were limited to $LaFeAsO$. The study presented in this master-thesis, extending the DFT+DMFT calculations of one- and two- particle properties to several families of Fe-based SC, aims to demonstrate the applicability of the proposed interpretation, by analyzing the different material trends. In addition to that, extended calculations will also allow to examine more qualitative the somewhat heuristic explanation of the quantum dynamical screening of the moment, through a precise quantification of the time-scales controlling the spin dynamics in all the materials considered.

Chapter 2

Theory and methods:

In chapter 2.1 we first give a brief overview of some of the quantum field theoretical (QFT) methods used in this thesis. This it is mainly intended as an introduction to the notation used in the following chapters, rather than a thorough review. For a more detailed discussion of the application of QFT to solid state physics we refer to [17]. In chapter 2.2, we provide a brief description of the ab-initio DFT+DMFT.

In chapter 2.3.1 we illustrate some of the basic relations of bosonic diagonal correlation functions, to which the spin-spin response function belongs, in greater detail. We will focus especially on the connection between "imaginary-time-" and the dissipative part of a correlation function, because these kind of relations are of significant importance for the interpretation of our numerical results (chapter 4 and 5). Eventually, we devote section 2.4 to provide a brief introduction to the methods of analytical continuation used in this thesis.

2.1 Quantum Field Theory in the context of Solid-State-Physics

It may seem, at a first sight, surprising that an intrinsically non-relativistic theory (Notice that we always use the Schrödinger- rather than the Dirac-equation) requires concepts of Quantum Field Theory (QFT). The main reason is that solving the Schrödinger equation for a system with $\mathcal{O}(10^{23})$ (interacting) particles is a hopeless endeavor. In solid-state physics, one is, however, mainly interested in expectation values and correlation functions, for which a systematic way of computation exists in QFT even in the presence of infinite degrees of freedom.

The central quantity in thermal quantum field theory in the context of solid-state-physics is the imaginary¹ time Green's function

$$G_{i_1, i_2}(\tau_1, \tau_2) = (-1) \langle \mathcal{T} \hat{c}_{i_1}(\tau_1) \hat{c}_{i_2}^\dagger(\tau_2) \rangle. \quad (2.1)$$

The operators $\hat{c}_i/\hat{c}_i^\dagger$ annihilate/ create particles with quantum-numbers i . The expectation-values $\langle \dots \rangle$ is understood as a trace over the (grand-canonical density-matrix. The time-ordering

¹For computational reasons it is favorable to do as many calculations in imaginary- rather than in real time, as possible. The translation of imaginary-time- to real-time-quantities will be discussed in more detail in section 2.3.1 and 2.4.

operator \mathcal{T} orders operators chronologically from left to right

$$\mathcal{T}\hat{A}(\tau_1)\hat{B}(\tau_2) = \theta(\tau_1 - \tau_2)\hat{A}(\tau_1)\hat{B}(\tau_2) + \epsilon\theta(\tau_2 - \tau_1)\hat{B}(\tau_2)\hat{A}(\tau_1),$$

with $\epsilon = -(/+)$ for fermionic (/bosonic) \hat{A} and \hat{B} . Due to time-translation symmetry $G(\tau_1, \tau_2) = G(\tau_1 - \tau_2) \equiv G(\tau)$. In general, it is more convenient to perform computations in imaginary frequencies, so called Matsubara-frequencies ($i\omega_n$), rather than in imaginary time. We use the convention

$$\begin{aligned} G(\tau) &= \frac{1}{\beta} \sum_{n=-\infty}^{\infty} e^{-i\omega_n \tau} G(i\omega_n) \\ G(i\omega_n) &= \int_0^{\beta} d\tau e^{i\omega_n \tau} G(\tau). \end{aligned} \quad (2.2)$$

Another important quantity in QFT, as well as in quantum many-body theory, is the self-energy Σ . It is related to the full Green's function G and the non-interacting Green's function G_0 via the Dyson equation

$$\Sigma(i\omega_n) = G_0^{-1}(i\omega_n) - G^{-1}(i\omega_n).$$

and describes the changes of the propagation of one added/removed particle due to the electron-electron interaction. An analogous relation holds in real frequencies.

Connection to Fermi-liquid theory:

The surprising fact that some properties of a system of interacting fermions can be qualitatively described by a non-interacting theory, albeit with renormalized parameters can be understood rigorously from a diagrammatic point of view. While a full derivation is beyond the scope of this thesis and can be found in *Abrikosov's* textbook[17], we only give here approximations for quasi-particle excitation life-times, mass-renormalization and energy-shifts here. These relations are used extensively for the analysis of the numerical data given in chapter 4 and 5.

We start by recalling that the spectral function $\mathcal{A}(\omega)$ gives a direct link between theory and (ARPES/IARPES)-experiments. It is related to the full Green's function via

$$\mathcal{A}(\omega, \vec{k}) = -\frac{1}{\pi} \text{Im} G^R(\omega, \vec{k}) = -\frac{1}{\pi} \text{Im} G(i\omega_n \rightarrow \omega + i0^+, \vec{k}).$$

Where $G^R(\omega, \vec{k})$ is the retarded Green's function. Inserting the Dyson-equation we get²

$$\mathcal{A}(\omega, \vec{k}) = \frac{-1}{\pi} \frac{\text{Im} \Sigma(\omega, \vec{k})}{(\omega - \epsilon_{\vec{k}} - \text{Re} \Sigma)^2 + (\text{Im} \Sigma(\omega))^2}$$

Excitations close to the Fermi-energy ϵ_F (usually set to zero) can be understood by a Taylor-expansion of $\Sigma(\omega)$ around ϵ_F . Since, in this work we only apply these relations to (local) DMFT results only, we neglect the \vec{k} dependence.

$$\Sigma(\omega) \cong \overbrace{\Sigma(0)}^{\equiv -i\gamma + \text{Re} \Sigma} + \omega \left(\frac{\partial}{\partial \omega} \Sigma(\omega) \right) \Big|_{\omega=0}. \quad (2.3)$$

We should keep in mind, nonetheless, that a DMFT-calculation, as many other many-body algorithms, give as a result the self-energy in Matsubara-frequencies $\Sigma(z = i\omega_n)$ and not the needed real frequency object $\Sigma(z = \omega)$. In practice, one often needs to extract the Fermi-liquid parameters by fitting a polynomial function through the first few Matsubara- frequencies.

²Assuming that $\text{Im} \Sigma \neq 0$. Else-wise additional $i0^+$ terms need to be considered explicitly.

While the value at $\omega = 0$ can then be directly plugged into Eq. 2.3, the derivatives need to be transformed by the Cauchy-Riemann differential equation

$$\begin{aligned}\frac{\partial}{\partial \omega_n} \text{Im} \Sigma(i\omega_n) &= \frac{\partial}{\partial \omega} \text{Re} \Sigma(\omega) \equiv -\alpha \\ \frac{\partial}{\partial \omega_n} \text{Re} \Sigma(i\omega_n) &= -\frac{\partial}{\partial \omega} \text{Im} \Sigma(\omega).\end{aligned}\quad (2.4)$$

By symmetry considerations (not shown here) the second equation gives zero at $\omega = 0$. The first is related to the renormalization factor Z by

$$Z = \frac{1}{1 + \alpha}$$

Inserting Eq. 2.3 into the spectral function gives

$$\mathcal{A}(\omega) = \frac{Z}{\pi} \frac{Z\gamma}{[\omega - Z(\epsilon + \text{Re} \Sigma(0))]^2 + Z^2\gamma^2}.$$

This shows that $\text{Re} \Sigma(i\omega_n = 0)$ "shifts" energy-levels. $\text{Im} \Sigma(i\omega = 0)$ leads to a finite width of the spectral function and thus to finite quasi-particle excitation life-times. The derivative $\frac{\partial}{\partial \omega_n} \text{Im} \Sigma(\omega_n)$, which enters in the definition of Z , renormalizes the spectral weight and rescales the (new) energies, which correspond to an effective renormalization of the electron-mass.

2.2 Ab initio calculations: DFT + DMFT

In this subsection, we give a very brief introduction of density-functional-theory and dynamical mean-field theory. Parts of the DFT section are based on the PhD thesis of N. Parragh[18], one of the key-developers of "w2dynamics"[19], the QMC-program we used. The DFT data was generated with "VASP"[20] and "wannier90"[12] by our colleagues in Würzburg. The cRPA-results used for the DMFT calculation were taken from [21]. More details can be found in the given references.

DFT+DMFT is an ab-initio way of tackling one of the most interesting and difficult problems in contemporary physics, namely the electronic properties of materials, in which the kinetic and interaction energy-scales are of the same order of magnitude[22]. The first method, density-functional theory has achieved great success in calculating electronic orbital-structures for a wide class of materials. DFT is based on the Hohenberg-Kohn theorem, which states that an external potential and thus the total energy and all ground-state properties of a system are a unique functional of the density ρ . While the existence of such a (universal) functional is proven, its explicit form is unknown. To make this more clear we go through all terms one by one.

$$E[\rho] = E_{\text{kin}}[\rho] + E_{\text{ion}}[\rho] + E_{\text{H}}[\rho] + E_{\text{xc}}[\rho].$$

The Hartree-functional $E_{\text{H}}[\rho]$ as well as the ionic energy functional $E_{\text{ion}}[\rho]$ can be explicitly written as

$$E_{\text{H}}[\rho] = \frac{1}{2} \int d\vec{r} \int d\vec{r}' V_{\text{ee}}(\vec{r}, \vec{r}') \rho(\vec{r}) \rho(\vec{r}')$$

and

$$E_{\text{ion}}[\rho] = \int d\vec{r} V_{\text{ion}}(\vec{r}) \rho(\vec{r}).$$

On the other hand, the kinetic part, $E_{\text{kin}}[\rho]$ is intrinsically unknown. This is due to $E_{\text{kin}} \propto |\nabla\psi|^2$, the kinetic energy depends on the phase of the wave-function whereas the density $\rho \propto |\psi|^2$ does not. The question "Given a density ρ , what is its kinetic energy?" is therefore impossible to answer. Kohn and Sham (KS), however, made some progress by realizing that the question "Given a density ρ , that can be split up into one particle auxiliary wave-functions ϕ_i , what is its kinetic energy?" has a definite answer. The KS-density then fulfills $\rho = \sum_i |\phi_i(\vec{r})|$. A variation of the functional $E[\rho[\phi_i]]$ with respect to the one particle auxiliary wave-functions $\phi_i(\vec{r})$, under the equality constraint of normalized wave-functions leads to the KS-equations

$$\left[-\frac{1}{2m_e} \nabla^2 + V_{\text{ion}}(\vec{r}) + \int d\vec{r}' V_{\text{ee}}(\vec{r} - \vec{r}') \rho(\vec{r}') + \frac{\delta E_{\text{ex}}[\rho]}{\delta \rho(\vec{r})} \right] \phi_i(\vec{r}) = \epsilon_i \phi_i(\vec{r}).$$

The Lagrange-multipliers $\{\epsilon_i\}$ are, in the solid-state community, established as "energies" of the KS-orbitals.

The only remaining problem is the choice of the so called exchange-correlation potential $E_{\text{ex}}[\rho]$. The exchange-part comes from the Fock-term (anti-symmetrization of the wave-function), which needs to be included in $E_{\text{ex}}[\rho]$. The correlation-part comes from all other interaction terms that go beyond the already included Hartree-term. $E_{\text{ex}}[\rho]$ is not known. Some of the widely used ones in the solid-state theory community (like LDA) have the jellium model a starting point. The jellium model, which assumes that the charge in a system is homogeneously spread (like jelly) is, however, not ideal for strongly-localized orbitals, like $3d$ - and $4f$ - orbitals. The dynamical mean field theory (DMFT) on the other hand captures the local part of interactions fully, but at a cost of significantly higher numerical effort. A combination of DFT with DMFT might therefore be useful a realistic treatment of electronic calculations in these classes of materials.

DMFT was developed by the model-Hamiltonian community to solve the Hubbard-model[23] in non-perturbative parameter-regimes, i.e. where the hopping amplitude t and local interaction energy U are of the same order of magnitude. It can be formally be derived by rescaling the hopping in the limit of infinite dimensions (or equivalently the number of neighbors) in such a way that the competition between the terms of the Hamiltonian remains non-trivial[24]. The second important step, which made DMFT so successful, came from mapping the Hubbard-Model in this limit onto the Anderson impurity model (AIM)[25]. It can be achieved by imposing the equality of the (local) self energy, or equivalently the (local) Green's function. For the AIM a number of efficient solvers are available like the Hirsch-Fye continuous time Quantum Monte-Carlo Method³, Exact Diagonalization, ...). The DMFT-self-consistency cycle is sketched in Fig.2.1

³For all the calculations the Continues-time Quantum Monte-Carlo (CT-QMC) Method in Hybridization-expansion was used within this thesis[19].

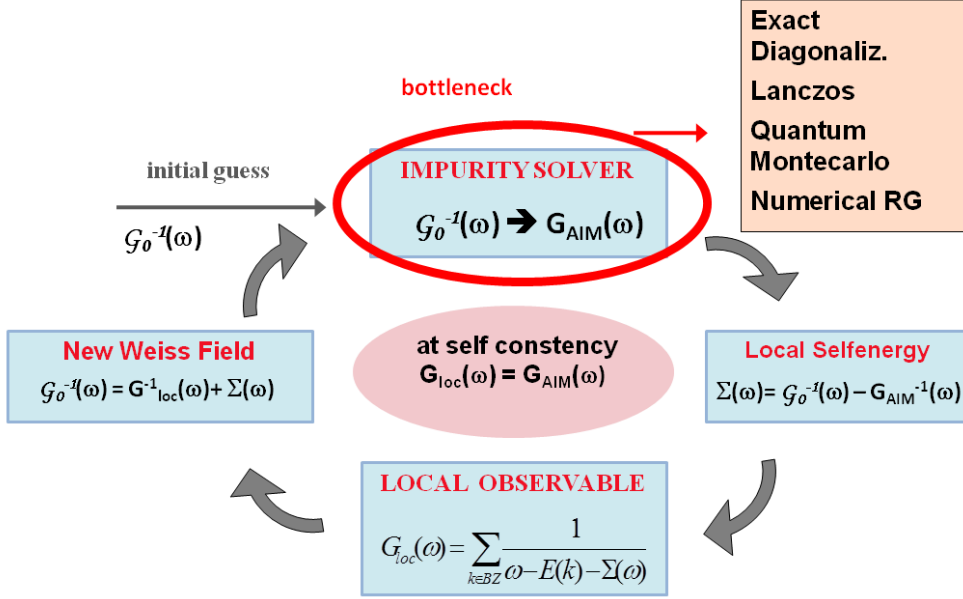


Figure 2.1: Illustration of the self-consistency cycle of the dynamical mean field theory. The *bottleneck* of the algorithm is the solution of the Anderson impurity model which is needed in every cycle. For all results in the DMFT results in this thesis a *continues time Quantum Monte-Carlo in Hybridization expansion (QMC)*[26] solver was used as an impurity solver. (Figure reproduced from [27])

We briefly recall here the definitions of the local Green's-function $G_\sigma(i\omega_n)$, the dynamical mean field $\mathcal{G}_\sigma(i\omega_n)$ and the local self-energy $\Sigma_\sigma(i\omega_n)$ (e.g. from [22])

$$G_\sigma^i(i\omega_n) = \langle c_\sigma^i(i\omega_n) c_\sigma^{i\dagger}(i\omega_n) \rangle_{\mathcal{A}[\mathcal{G}]} \quad (2.5)$$

$$\Sigma_\sigma(i\omega_n) = \mathbf{G}_\sigma(i\omega_n)^{-1} - \mathbf{G}_\sigma(i\omega_n)^{-1} \quad (2.6)$$

$$\mathbf{G}_\sigma(i\omega_n) = \frac{1}{N_k} \sum_{\vec{k}}^{\text{1.BZ}} \frac{1}{i\omega_n + \mu - \mu_{DC} - \Sigma_\sigma(i\omega_n) - \mathbf{H}_{\vec{k}}} \quad (2.7)$$

The bold notation indicates matrices in the orbital-space. Eq. 2.5 denotes the determination of the impurity Green's function, by creating/annihilating particles on the impurity of the auxiliary AIM associated to the DMFT cycle, where the quantum-statistical mechanics are governed by the action \mathcal{A} , which is a functional of the Weiss-field \mathcal{G} . The self-consistency is imposed in the following way:

First we start with some initial conditions for the dynamical mean field \mathcal{G} . By solving (2.5) with CT-QMC-HYB we obtain the local (impurity) Green's function. Then, by using the

Dyson equation (2.6), we calculate the self energy from the impurity Green's function G and the dynamical mean field \mathcal{G} . Finally, we use the self-consistency equation (2.7) to calculate the 'new' Green's function of the material under consideration and by applying the Dyson equation (2.6) again to get the 'new' dynamical mean field. The procedure repeats until convergence is reached.

Combining the two methods:

A crucial step when combining the DFT- with the DMFT-calculation is transforming the DFT-basis functions into the local DMFT-orbitals. To capture the majority of the Coulomb interaction, by a purely local term, strongly localized orbitals are necessary. One therefore uses a maximally localized linear combination of the DFT-orbitals, known as maximally localized Wannier-functions (MLWF). As a localization criteria one can use

$$\min \sum_n \left[\langle \vec{0}n | \hat{r}^2 | \vec{0}n \rangle - \langle \vec{0}n | \hat{r} | \vec{0}n \rangle^2 \right],$$

where $|\vec{R}, n\rangle$ are (to be determined) maximally localized Wannier-functions (MLWF), centered around \vec{R} , form the chosen target orbitals close to the Fermi-level. The (hopping-terms) are then extracted via the corresponding KS-Hamiltonian \mathcal{H}_{KS} as

$$t_{mn}(\vec{R}) = \langle \vec{0}m | \mathcal{H}_{KS} | \vec{R}n \rangle. \quad (2.8)$$

It is clear, that the definition of an effective one-particle Hamiltonian in the Wannier basis is not sufficient for performing a DMFT calculation. A consistent determination of the corresponding interaction parameters is also essential. In practice, effective interaction parameters are often approximated by a constraint random phase (cRPA) calculation, by calculating overlap integrals between the MLFW and the cRPA interaction operator $W_r(\vec{r}, \vec{r}', \omega)$ at zero frequency. The constraint being that the target manifold's contribution is cut out to avoid double counting.

The effective orbital dependent Coulomb- interaction (U) and exchange parameters (J) are given by

$$\begin{aligned} U_{ml}(\vec{R}) &= \langle \vec{0}m | \langle \vec{0}m | \hat{W}_r | \vec{R}n \rangle | \vec{R}n \rangle \\ J_{ml}(\vec{R}) &= \langle \vec{0}m | \langle \vec{0}n | \hat{W}_r | \vec{R}n \rangle | \vec{R}m \rangle. \end{aligned} \quad (2.9)$$

Details about the cRPA calculation for the materials in this thesis can be found in [21]. For a general review on cRPA in the context of DFT+DMFT we refer to [22].

2.2.1 Model-Hamiltonians in this thesis

Once the interaction terms (e.g. from an cRPA calculation) and the hopping terms are known one can turn to solving the corresponding Hubbard model. Another important step is the extraction of the already in the DFT-calculation included interactions (for the target orbitals). While this is still an extensively debated problem several (approximate) solutions have been proposed. We will come back to this problem, and the solutions we chose for the Fe-based SC in Chapter 3. Before turning to the explicit Hamiltonians we used in this mater thesis, we

would like to take a look at a generic multi-orbital Hubbard-Hamiltonian with particle number conserving local two-particle interaction:

$$\begin{aligned} H &= \sum_{iljm} t_{ilmjm} \hat{c}_{il}^\dagger \hat{c}_{jm} + \sum_{ilmno} U_{i,lmno} \hat{c}_{il}^\dagger \hat{c}_{im}^\dagger \hat{c}_{in} \hat{c}_{io} \\ &= \hat{H}_{\text{DFT}} - \sum_{i,l} \mu_{il}^{DC} \hat{n}_{il} + \sum_{ilmno} U_{i,lmno} \hat{c}_{il}^\dagger \hat{c}_{im}^\dagger \hat{c}_{in} \hat{c}_{io}. \end{aligned} \quad (2.10)$$

Indices i, j give the position of a lattice-site. The others ($lmno$) correspond to the orbitals. The DC-correction term is denoted as μ_{il}^{DC} . To make a connection with the matrix-notation in the previous paragraph (for $\vec{R} = 0$) we note that

$$\begin{aligned} U_{i,mm'mm'} &= U_{mm'} \\ U_{i,mm'm'm} &= J_{mm'} \quad \text{for } m \neq m'. \end{aligned} \quad (2.11)$$

The full interaction term given in Eq. 2.10 is, however, rarely used for DFT+DMFT calculations. The main reason being that efficient and stable⁴ impurity-solvers exist for simplified models where the orbital dependence is neglected. For the calculations in this thesis we have exploited the following three interaction Hamiltonians for the 5 Fe- d -orbitals:

$$\begin{aligned} \hat{H}_{avg}^{d-d} &= U \sum_{m=1}^5 \hat{n}_{m\downarrow} \hat{n}_{m\uparrow} + \sum_{m \neq m'} (V - J \delta_{\sigma\sigma'}) \hat{n}_{m\sigma} \hat{n}_{m'\sigma'} \\ \hat{H}_{avg}^K &= U \sum_{m=1}^5 \hat{n}_{m\downarrow} \hat{n}_{m\uparrow} + \sum_{m \neq m'} (V - J \delta_{\sigma\sigma'}) \hat{n}_{m\sigma} \hat{n}_{m'\sigma'} \\ &\quad - J \sum_{m \neq m'} c_{m\uparrow}^\dagger c_{m\downarrow}^\dagger c_{m'\downarrow} c_{m'\uparrow} + c_{m\uparrow}^\dagger c_{m\downarrow}^\dagger c_{m'\downarrow} c_{m'\uparrow} \\ \hat{H}_f &= \frac{1}{2} \sum_{lmno} U_{lmno} \sum_{\sigma\sigma'} \hat{c}_{l\sigma}^\dagger \hat{c}_{m\sigma'}^\dagger \hat{c}_{n\sigma'} \hat{c}_{o\sigma} \end{aligned} \quad (2.12)$$

The first one, known as density-density-interaction, conserves the total particle number N , the total spin in z-direction S_z and occupation numbers $n_{m\sigma}$. The second is the Kanamori-Hamiltonian. It conserves N , S_z and the pseudo-spin quantum-number PS [28]. The difference to \hat{H}^{d-d} is the inclusion of spin-flips and pair-hopping, which restore the $SU(2)$ symmetry of the interaction term. Both are shown, and used in this thesis, with averaged U and J values.

$$\begin{aligned} U &= \frac{1}{(2l+1)} \sum_i U_{ii} \\ J &= \frac{1}{2l(2l+1)} \sum_{\substack{ij \\ i \neq j}} J_{ij} \\ U &= U - 2J. \end{aligned} \quad (2.13)$$

The third Hamiltonian \hat{H}_f , which is in principle more realistic, is referred to in this thesis as "full U ". It only conserves N and S_z . Density-density- and Kanamori-interactions can be regarded as all special (approximate) cases of full U interaction.

⁴E.g. one can show that for a Segment solver (for dens.-dens.- interaction) no sign-problem can occur.

2.3 Properties of Correlation-functions

In this section we will show some basic properties of correlation functions "diagonal" in the bosonic operators \hat{A} , because the spin-spin correlation function which is of interest in this work belongs to this class.

First, we show that $\chi_{AA}(\tau)$ in imaginary time is real-valued, positive and concave, before using these properties to show that $\chi_{AA}(i\omega_n) \in \mathbb{R}^+$. We then discuss fundamental properties of the susceptibilities on the real time-axis, namely the Kubo-Martin-Schwinger-relation and the Fluctuation-Dissipation theorem. These basic properties are then used to derive the connection between $\chi_{AA}(\tau)$ and $\chi_{AA}^{av./ret.}(\omega)$. Further, we show a more general relation between $\chi_{AA}(\tau)$ and $\chi_{AA}^{av./ret.}(\omega)$ to be used if $\chi(\tau)$ is known only numerically. To get familiar with the derived relations, we discuss some model cases, namely the "Atomic Limit" and the "Harmonic-oscillator". These will make it easier to interpret the obtained DFT+DMFT for the Fe-based SC in chapter 4 and 5.

2.3.1 Properties in imaginary time and Matsubara frequencies

"Time"-translation symmetry:

For a time independent Hamiltonian invariance of the trace under cyclical permutations yields $\langle \hat{A}(t)\hat{B}(0) \rangle = \langle \hat{A}(0)\hat{B}(-t) \rangle$.

For imaginary time τ , one can derive instead

$$\begin{aligned} \langle \hat{A}(\tau)\hat{B} \rangle &= \frac{1}{Z} \text{Tr} e^{-\beta\hat{H}} \left(e^{\tau\hat{H}} \hat{A} e^{-\tau\hat{H}} \right) \hat{B} \\ &= \frac{1}{Z} \text{Tr} e^{-\beta\hat{H}} e^{\tau\hat{H}} \hat{A} \left(e^{-\tau\hat{H}} \hat{B} e^{\tau\hat{H}} \right) e^{-\tau\hat{H}} \\ &= \frac{1}{Z} \text{Tr} e^{-\beta\hat{H}} \hat{A} \left(e^{-\tau\hat{H}} \hat{B} e^{\tau\hat{H}} \right) \\ &= \langle \hat{A}\hat{B}(-\tau) \rangle, \end{aligned} \tag{2.14}$$

where we inserted a $\mathbf{1} = e^{+\tau\hat{H}}e^{-\tau\hat{H}}$ in the second line, used cyclicity of the trace in the third line and the obvious fact that $[\hat{H}, \hat{H}] = 0$ in the fourth line. This shows that time-translation symmetry holds for real time as well as imaginary times. One can even combine the two as

$$\langle \hat{A}(t+i\tau)\hat{B}(0) \rangle = \langle \hat{A}(0)\hat{B}(-t-i\tau) \rangle,$$

for $\beta > \tau > -\beta$.

Periodicity in β :

Defining a general susceptibility in imaginary time as

$$\chi_{AB}(\tau) = \langle \mathcal{T} \hat{A}(\tau)\hat{B}(0) \rangle = \theta(\tau) \langle \hat{A}(\tau)\hat{B}(0) \rangle + \theta(-\tau) \langle \hat{B}(0)\hat{A}(\tau) \rangle \tag{2.15}$$

with $\beta > \tau > -\beta$ one can use the invariance of the trace under cyclical permutations to show for $\tau > 0$ that

$$\begin{aligned} \chi_{AB}(\tau - \beta) &= \langle \mathcal{T} \hat{A}(\overbrace{\tau - \beta}^{<0})\hat{B} \rangle = \langle \hat{B}\hat{A}(\tau - \beta) \rangle = \frac{1}{Z} \text{Tr} e^{-\beta\hat{H}} \hat{B} e^{(\tau-\beta)\hat{H}} \hat{A} e^{-(\tau-\beta)\hat{H}} \\ &= \frac{1}{Z} \text{Tr} e^{-\beta\hat{H}} e^{\tau\hat{H}} \hat{A} e^{-\tau\hat{H}} \hat{B} \\ &= \langle \hat{A}(\tau)\hat{B}(0) \rangle = \chi_{AB}(\tau). \end{aligned} \tag{2.16}$$

One can therefore restrict the imaginary time-domain to $0 \leq \tau \leq \beta$.

Positiveness and real valuedness:

This property only hold for certain choices of \hat{A} and \hat{B} , e.g. for $\hat{A} = \hat{B}$. We therefore refer to it as a property of "diagonal" correlation-functions. Writing down a general diagonal susceptibility (for $\tau > 0$) in a matrix-element representation⁵ we get

$$\begin{aligned}\chi_{AA}(\tau > 0) &= \frac{1}{Z} \text{Tr} e^{-\beta \hat{H}} \hat{A}(\tau) \hat{A}(0) \\ &= \frac{1}{Z} \sum_n \langle n | e^{-\beta \hat{H}} \hat{A}(\tau) \sum_m |m\rangle \langle m| \hat{A}(0) |n\rangle \\ &= \frac{1}{Z} \sum_{n,m} e^{-\beta E_n} e^{\tau(E_n - E_m)} \langle n | \hat{A} |m\rangle \langle m | \hat{A} |n\rangle \\ &= \frac{1}{Z} \sum_{n,m} e^{-\beta E_n} e^{\tau(E_n - E_m)} |\langle n | \hat{A} |m\rangle|^2\end{aligned}\quad (2.17)$$

Since everything on the right-hand side of the above equation is real-valued and positive we have shown that $\chi_{AA}(\tau) \in \mathbb{R}^+$.

Mirror-symmetry around $\beta/2$:

Again this property only holds for $\hat{A} = \hat{B}$. To see this symmetry it is convenient to start from Eq. 2.17 by inserting $\tau = \beta/2 + \Delta\tau$.

$$\begin{aligned}\chi_{AA}(\tau = \beta/2 + \Delta\tau) &= \frac{1}{Z} \sum_{n,m} e^{-\beta E_n} e^{(\beta/2 + \Delta\tau)(E_n - E_m)} |\langle n | \hat{A} |m\rangle|^2 \\ &= \frac{1}{Z} \sum_{n,m} e^{-\beta/2(E_n + E_m)} e^{\Delta\tau(E_n - E_m)} |\langle n | \hat{A} |m\rangle|^2 \quad (n \leftrightarrow m) \\ &= \frac{1}{Z} \sum_{n,m} e^{-\beta/2(E_n + E_m)} e^{-\Delta\tau(E_n - E_m)} |\langle n | \hat{A} |m\rangle|^2 \\ &= \chi_{AA}(\tau = \beta/2 - \Delta\tau),\end{aligned}\quad (2.18)$$

where we have exchanged the (dummy-)indices n and m in the second line of Eq. 2.18. The last property follows from observing that the second line is the same as the third line, but for negative $\Delta\tau$.

Moreover combining the mirror-symmetry around $\beta/2$ with the above shown periodicity, implies a symmetry around $\tau = 0$ $\chi(-\tau) = \chi(\tau)$, which can also be directly derived from (imaginary-) time-translation symmetry.

Concavity:

Differentiating Eq. 2.17 twice gives

$$\frac{d^2}{d\tau^2} \chi_{AA}(\tau) = \frac{1}{Z} \sum_{n,m} e^{-\beta E_n} (E_n - E_m)^2 e^{\tau(E_n - E_m)} |\langle n | \hat{A} |m\rangle|^2, \quad (2.19)$$

which is evidently greater or equal to 0. From this, we can immediately deduce that (unless $\chi(\tau) = \text{const.}$) there is at most one minimum (in the region from 0 to β , which is located at $\tau = \beta/2$).

⁵Unless mentioned otherwise we use the notation that $|n\rangle$ is an eigenvector of \hat{H} . Because \hat{H} is Hermitian $\{|n\rangle\}$ are complete $\sum_{i=1}^{\dim \hat{H}} |n\rangle \langle n| = \mathbf{1}$

Fourier-series and Matsubara frequencies:

Since $\chi_{AB}(\tau)$ is an integrable periodic function, it can be represented by a Fourier series. One must keep in mind that $\chi_{AB}(\tau)$ is not necessarily defined for $|\tau| > \beta$. The infinite Fourier-series is then built on periodically continued function for $|\tau| > \beta$. The Fourier-components of $\chi_{AB}(\tau)$ are usually denoted as $\chi_{AB}(i\omega_n)$ and are related to $\chi_{AB}(\tau)$ by

$$\chi_{AB}(\tau) = \frac{1}{\beta} \sum_{n=-\infty}^{\infty} \chi_{AB}(i\omega_n) e^{-i\omega_n \tau}. \quad (2.20)$$

The symmetry $\chi(\tau + \beta) = \chi(\tau)$ imposes $e^{-i\omega_n \beta} = 1$, and therefore the only frequencies allowed are

$$\omega_n = \frac{2\pi n}{\beta}.$$

These are known as bosonic Matsubara frequencies. The inverse transformation is:

$$\chi_{AB}(i\omega_n) = \int_0^\beta d\tau \chi_{AB}(\tau) e^{i\tau \omega_n} \quad (2.21)$$

 $\chi_{AA}(i\omega_n)$ is real valued

One can show:

$$\begin{aligned} \text{Im } \chi_{AA}(i\omega_n) &= \int_0^\beta d\tau \chi_{AA}(\tau) \sin(\omega_n \tau) \\ &= \left(\int_0^{\beta/2} d\tau \chi_{AA}(\tau) \sin(\omega_n \tau) + \int_{\beta/2}^\beta d\tau \chi_{AA}(\tau) \sin(\omega_n \tau) \right) = 0. \end{aligned} \quad (2.22)$$

The second term in the bracket cancels the first. To show this we substitute (and rename) $\tau \rightarrow \beta - \tau$ in the second term which leads (via $d\tau \rightarrow -d\tau$ and after changing the boundaries accordingly) to

$$- \int_{\beta/2}^0 d\tau \overbrace{\chi_{AA}(\tau)}^{\chi_{AA}(\beta - \tau)} \overbrace{\sin(\omega_n \tau)}^{-\sin(\omega_n(\beta - \tau))} = - \int_0^{\beta/2} d\tau \chi_{AA}(\tau) \sin(\omega_n \tau). \quad (2.23)$$

and thus

$$\text{Im } \chi_{AA}(i\omega_n) = 0.$$

 $\chi(i\omega_n)$ is positive:

To show this we first use the fact that due to the symmetry around $\beta/2$ the Fourier-integral reduces to

$$\chi_{AA}(i\omega_n) = \int_0^\beta d\tau \chi_{AA}(\tau) e^{i\omega_n \tau} = 2 \int_0^{\beta/2} d\tau \chi_{AA}(\tau) \cos \omega_n \tau.$$

Second, we need to remember that $\chi_{AA}(\tau)$ is a concave, positive function with exactly one minimum at $\beta/2$ and therefore monotonically decreasing in the region $0 < \tau < \beta/2$. We then slice the integral into n regions⁶ (visualized for $n = 3$ and $n = 4$ in Fig. 2.2) as

⁶For $n \geq 1$. For $n = 0$ positivity is trivial.

$$\begin{aligned}
\chi_{AA}(i\omega_n) &= 2 \left(\int_0^{\frac{\beta/2}{n}} d\tau \chi_{AA}(\tau) \cos \omega_n \tau + \int_{\frac{\beta/2}{n}}^{2\frac{\beta/2}{n}} d\tau \chi_{AA}(\tau) \cos \omega_n \tau + \dots + \int_{\frac{(n-1)\beta/2}{n}}^{\beta/2} d\tau \chi_{AA}(\tau) \cos \omega_n \tau \right) \\
&\equiv 2 \left(\sum_{m=1}^n a_m \right).
\end{aligned} \tag{2.24}$$

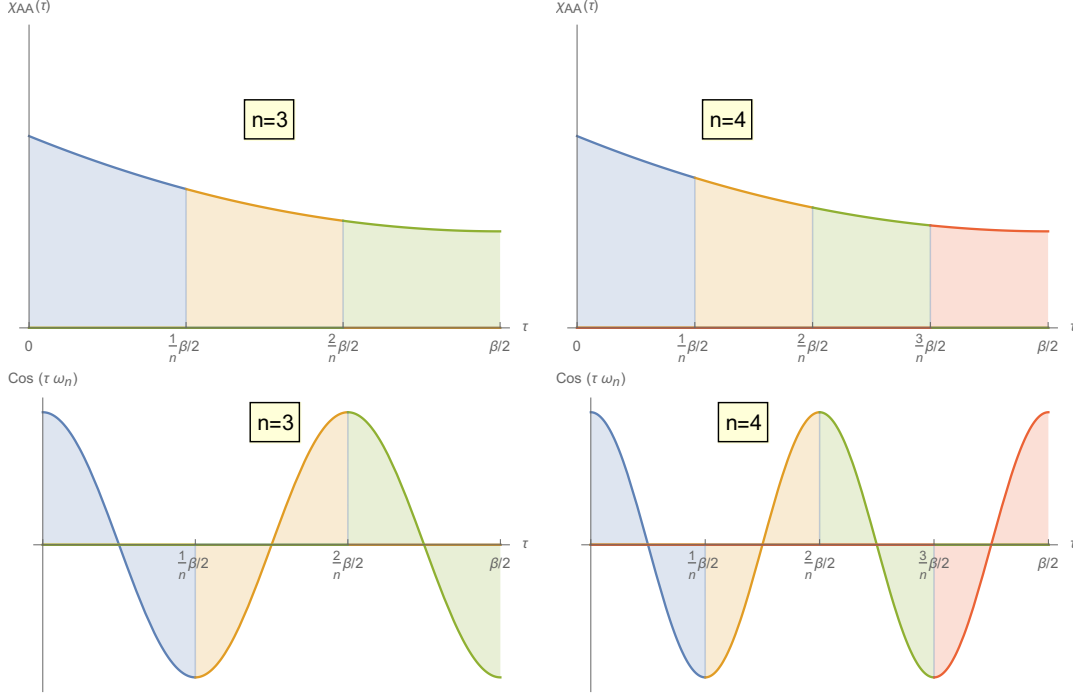


Figure 2.2: Visualization of the integrals for $\chi(i\omega_{n=3})$ (left) and $\chi(i\omega_{n=4})$ (right). The top figures show a representation of a real-valued positive concave function in the region $0 < \tau < \beta$ split up in the regions needed for Eq. 2.24. The sub-figures at the bottom show the second part of the integral in Eq. 2.24 split up into the appropriate regions.

The implicitly defined a_i 's fulfill

$$\begin{aligned}
(i) \quad & a_1 > 0 \\
(ii) \quad & \text{sign}(a_m) = (-1)^{m+1} \\
(iii) \quad & |a_m| > |a_{m+1}|.
\end{aligned} \tag{2.25}$$

Property (i), (ii) and (iii) follow from the fact that $\chi_{AA}(\tau)$ is strictly decreasing and positive and that $\cos(\omega_n \frac{m\beta/2}{n}) = -\cos(\omega_n \frac{(m+1)\beta/2}{n})$.

This shows that if n is even

$$\chi_{AA}(i\omega_n) = 2 \left(\overbrace{a_1 + a_2}^{>0} + \overbrace{a_3 + a_5}^{>0} + \dots + \overbrace{a_{n-1} + a_n}^{>0} \right) > 0, \tag{2.26}$$

and if n is odd

$$\chi_{AA}(i\omega_n) = 2 \left(\overbrace{a_1 + a_2}^{>0} + \overbrace{a_3 + a_5}^{>0} + \dots + \overbrace{a_n}^{>0} \right) > 0. \quad (2.27)$$

Thus

$$\chi_{AA}(i\omega_n) \in \mathbb{R}^+. \quad (2.28)$$

We can check this by looking at Fig. 2.2. An integral over (a multiplication of the two functions) of the blue region plus an integral over the yellow region is greater than zero. And the same is true for any consecutive regions after. If n is odd the last region (green for the $n = 3$ case) we get another positive contribution.

Lehmann representation in Matsubara frequencies

A very useful expression to show basic properties of correlation functions is the Lehmann-representation. Specifically we will use it to show the connection between $\chi(i\omega_n)$ and $\chi(\omega)$, which can be used if an analytical expression is known, and the connection between $\chi(\tau)$ and $\chi(\omega)$, if no analytical expression is known. All methods of analytical continuation of QMC-data (like MaxEnt, SpM, ...) are based on these relations. Moreover, we show some possible simplifications for diagonal correlation functions in the next sub-chapter.

For $\tau > 0$ one can write $\chi(\tau)$ as

$$\begin{aligned} \chi_{AB}(\tau) &= \langle \hat{A}(\tau) \hat{B} \rangle = \frac{1}{Z} \sum_{n,m} \langle n | e^{-\beta \hat{H}} e^{\tau \hat{H}} \hat{A} e^{-\tau \hat{H}} | m \rangle \langle m | \hat{B} | n \rangle \\ &= \frac{1}{Z} \sum_{n,m} e^{-\beta E_n} e^{\tau (E_n - E_m)} \overbrace{a_{nm} b_{mn}}^{\equiv \omega_{nm}}, \end{aligned} \quad (2.29)$$

where we inserted a complete $\mathbf{1} = \sum_m |m\rangle \langle m|$ in the first line and used the abbreviations $a_{nm} = \langle n | \hat{A} | m \rangle$. Fourier-transforming the above equation gives

$$\begin{aligned} \chi_{AB}(i\omega_n) &= \frac{1}{Z} \sum_{n,m} (1 - e^{-\beta \omega_{nm}}) e^{-\beta E_n} a_{nm} b_{mn} \frac{1}{\omega_{nm} - i\omega_n} \\ &= \int_{-\infty}^{\infty} d\omega' \frac{S(\omega')}{\omega' - i\omega_n} \end{aligned} \quad (2.30)$$

where we used the spectral function

$$S(\omega) = \frac{1}{Z} (1 - e^{-\beta \omega}) \sum_{n,m} a_{nm} b_{mn} e^{-\beta E_n} \delta(\omega - \omega_{nm}). \quad (2.31)$$

Eq. 2.30 is known as the Lehmann-representation. We will later show that $\chi(\omega)$ can be expressed by a similar integral over the *same* spectral function $S(\omega)$. This will allow us to show the relation between $\chi(i\omega)$ and $\text{Im} \chi(\omega)$ for an analytically known $\chi(\tau)$. To show the other relation, which can also be used if $\chi(\tau)$ is not analytically known, we need to transform the Lehmann-representation of $\chi(i\omega_n)$ back into imaginary time

$$\begin{aligned} \chi_{AB}(\tau) &= \frac{1}{\beta} \sum_n e^{-i\omega_n \tau} \chi_{AB}(i\omega_n) \\ &= \int_{-\infty}^{\infty} d\omega S(\omega) \left(\frac{1}{\beta} \sum_n \frac{e^{-\tau \omega_n}}{\omega - i\omega_n} \right) \\ &= \int_{-\infty}^{\infty} d\omega S(\omega) \frac{e^{-\omega \tau}}{1 - e^{-\beta \omega}}. \end{aligned} \quad (2.32)$$

In the first second line of Eq. 2.32 we inserted the Lehmann-representation and exchanged integration and summation. Moreover, we used that

$$\frac{1}{\beta} \sum_n \frac{e^{-\tau\omega_n}}{\omega - i\omega_n} = \frac{e^{-\tau\omega}}{1 - e^{-\beta\omega}},$$

since

$$\oint dz \frac{1}{z - \epsilon} \frac{e^{-\tau z}}{1 - e^{-z\beta}} = 0 = 2\pi i \left(\sum_n \frac{1}{\beta} \frac{e^{-\tau\omega_n}}{i\omega_n - \epsilon} + \frac{e^{-\epsilon\tau}}{1 - e^{-\beta\epsilon}} \right),$$

by the residual theorem.

2.3.2 Properties in real time and real frequencies

Kubo-Martin-Schwinger (KMS) relation

Before turning to the Lehman-representation of $\chi^{R/A}(\omega)$ we will briefly derive another very useful theorem, the KMS relation. When deriving the Lehman-representation, or the Fluctuation Dissipation theorem one can derive the KMS-relation without additional effort. We start from the spectral representation of the two elementary constituents of any (two-point-) correlation function, which are the $D^>$ and $D^<$ functions and defined as

$$\begin{aligned} D^>(t) &\equiv \langle \hat{A}(t) \hat{B}(0) \rangle = \frac{1}{Z} \sum_{n,m} e^{-\beta E_n} \langle n | e^{i\hat{H}t} \hat{A}(0) e^{-i\hat{H}t} | m \rangle \langle m | \hat{B}(0) | n \rangle \\ D^<(t) &\equiv \langle \hat{B}(0) \hat{A}(t) \rangle = \frac{1}{Z} \sum_{n,m} e^{-\beta E_n} \langle n | \hat{B}(0) | m \rangle \langle m | e^{i\hat{H}t} \hat{A}(0) e^{-i\hat{H}t} | n \rangle. \end{aligned} \quad (2.33)$$

Using the abbreviations

$$\begin{aligned} \omega_{mn} &\equiv (E_m - E_n) \\ a_{mn} &\equiv \langle m | \hat{A} | n \rangle \\ b_{mn} &\equiv \langle m | \hat{B} | n \rangle \end{aligned} \quad (2.34)$$

and renaming the dummy-indices ($n \rightleftharpoons m$) in the second equation we get

$$\begin{aligned} D^>(t) &= \frac{1}{Z} \sum_{n,m} e^{-\beta E_n} e^{-i\omega_{mn}t} a_{nm} b_{mn} \\ D^<(t) &= \frac{1}{Z} \sum_{n,m} e^{-\beta E_m} e^{-i\omega_{mn}t} a_{nm} b_{mn}. \end{aligned} \quad (2.35)$$

Fourier-transforming leads to

$$\begin{aligned} D^>(\omega) &= \frac{2\pi}{Z} \sum_{n,m} e^{-\beta E_n} \delta(\omega - \omega_{mn}) a_{nm} b_{mn} \\ D^<(\omega) &= \frac{2\pi}{Z} \sum_{n,m} e^{-\beta E_m} \delta(\omega - \omega_{mn}) a_{nm} b_{mn}, \end{aligned} \quad (2.36)$$

where we used:

$$\mathcal{F}(e^{-it\omega_{mn}}) = \int_{-\infty}^{\infty} dt e^{-it\omega_{mn}} e^{it\omega} = 2\pi \delta(\omega - \omega_{mn}) \quad (2.37)$$

From Eq. 2.36 one can immediately identify the so called Kubo-Martin-Schwinger relation

$$D^<(\omega) = D^>(\omega) e^{-\beta\omega}. \quad (2.38)$$

It should be stressed that the KMS relation is only valid in equilibrium. Out of equilibrium the deviation of $\frac{D^<(\omega)}{D^>(\omega)}$ from $e^{-\beta\omega}$ provides instead a measure how far the system is from thermalizing.

Lehmann-representation of $\chi^R(\omega)$ and $\chi^A(\omega)$

The Lehmann representation is a very general expression of two-point correlation functions in QFT. We will derive it briefly from Eq.2.36 and the definitions

$$\begin{aligned}\chi(t) &\equiv i \langle [\hat{A}(t), \hat{B}(0)] \rangle && \in \mathbb{R} \\ \chi^R(t) &\equiv \theta(t)\chi(t) \\ \chi^A(t) &\equiv -\theta(-t)\chi(t)\end{aligned} \quad (2.39)$$

Going to frequency-space each product with a θ function becomes a convolution. The Fourier-transforms of the θ -functions are

$$\begin{aligned}\tilde{\theta}^+(\omega) &\equiv (\mathcal{F}_t(\theta(t))) (\omega) = \frac{i}{\omega+i0^+} \\ \tilde{\theta}^-(\omega) &\equiv (\mathcal{F}_t(\theta(-t))) (\omega) = \frac{-i}{\omega-i0^+}.\end{aligned} \quad (2.40)$$

Which leads to

$$\begin{aligned}\chi^{R/A}(\omega) &= \frac{\pm i}{2\pi} \tilde{\theta}^\pm * (D^> - D^<) \\ &= \frac{\pm 1}{Z} \sum_{n,m} (e^{-\beta E_n} - e^{-\beta E_m}) a_{nm} b_{mn} \int d\omega' \frac{1}{\omega' \pm i0^+} \delta(\omega - \omega_{mn} - \omega') \\ &= \frac{\pm 1}{Z} \sum_{n,m} (e^{-\beta E_n} - e^{-\beta E_m}) a_{nm} b_{mn} \frac{1}{\omega - \omega_{mn} \pm i0^+},\end{aligned} \quad (2.41)$$

where we used standard-notation and denoted the convolution as $*$. Eq.2.41 can be rewritten as

$$\chi^{R/A}(\omega) = \int_{-\infty}^{\infty} d\omega' \frac{S(\omega')}{\omega' - \omega \mp i0^+}, \quad (2.42)$$

with the spectral function

$$S(\omega) = \frac{1}{Z} (1 - e^{-\beta\omega}) \sum_{n,m} a_{nm} b_{mn} e^{-\beta E_n} \delta(\omega - \omega_{mn}). \quad (2.43)$$

Eq.2.42 is the corresponding Lehmann-representation. Notice that the excitation-energies give the location of the poles of $\chi^{R/A}$ and that has no poles in the upper/(lower) half plane. Eq.2.43 is exactly the same expressions as in Eq.2.31. Q.E.D.

Thus if an analytical expression for $\chi(i\omega_n)$ is known one can get $\chi^{R/A}$ by simply replacing $i\omega_n$ by $\omega \pm i0^+$

$$\chi^{R/A}(\omega) = \chi(i\omega_n \rightarrow \omega \pm i0^+).$$

S can be real-valued for a certain choice of A and B , but it doesn't need to be. If it is, we find the property

$$\chi^R(\omega) = (\chi^A(\omega))^*.$$

For $\hat{A} = \hat{B}$ this is fulfilled since $(\langle n | \hat{A} | m \rangle \langle m | \hat{A} | n \rangle)^* = (\langle n | \hat{A} | m \rangle \langle m | \hat{A} | n \rangle)$. We may then extract the imaginary part of Eq.2.41 after using the Plemelj-Sokhotskii formula [29] as

$$\begin{aligned}\text{Im } \chi^{R/A}(\omega) &= \frac{\pm\pi}{Z} \sum_{n,m} (e^{-\beta E_n} - e^{-\beta E_m}) a_{nm} b_{mn} \delta(\omega - \omega_{mn}) \\ &= \pm\pi S(\omega)\end{aligned} \quad (2.44)$$

We should stress that this formula is only correct for certain choices of \hat{A} and \hat{B} . By comparing $\chi(\omega)$ with the $S(\omega)$ we find the general relation

$$\chi(\omega) = i2\pi S(\omega) = i (\text{Im } \chi^R(\omega) - \text{Re } \chi^A(\omega)).$$

So if the spectral function is real the (full) susceptibility (in ω) is purely imaginary. This is equivalent to a anti-symmetric susceptibility in real time. The retarded and advanced fulfill for this (special) case

$$\chi(\omega) = \pm 2i \operatorname{Im} \chi^{R/A}(\omega). \quad (2.45)$$

These expressions show that if we know the spectral function of a system we have access to the full information abouts the corresponding correlation properties.

Relation between $i \langle [\hat{A}(t), \hat{B}(0)] \rangle^R$ and $\langle \{\hat{A}(t), \hat{B}(0)\} \rangle$

A quite reasonable measure of fluctuations is given by the anti-commutator-correlation-function

$$F(t) \equiv \frac{1}{2} \langle \{\hat{A}(t), \hat{B}(0)\} \rangle \in \mathbb{R}. \quad (2.46)$$

To get its Fourier-transform we can use Eq. 2.36

$$\begin{aligned} F(\omega) &= D^> + D^< \\ &= \frac{\pi}{Z} \sum_{n,m} (e^{-\beta E_n} + e^{-\beta E_m}) a_{nm} b_{mn} \delta(\omega - \omega_{mn}) \\ &= (1 + e^{-\beta \omega}) \frac{\pi}{Z} \sum_{n,m} e^{-\beta E_n} a_{nm} b_{mn} \delta(\omega - \omega_{mn}) \end{aligned} \quad (2.47)$$

Comparing Eqn 2.47 to

$$\begin{aligned} \chi(\omega) &= i(D^> + D^<) \\ &= \frac{2i\pi}{Z} \sum_{n,m} (e^{-\beta E_n} - e^{-\beta E_m}) a_{nm} b_{mn} \delta(\omega - \omega_{mn}) \\ &= 2i(1 - e^{-\beta \omega}) \frac{\pi}{Z} \sum_{n,m} e^{-\beta E_n} a_{nm} b_{mn} \delta(\omega - \omega_{mn}), \end{aligned} \quad (2.48)$$

we find

$$\frac{F(\omega)}{-i\chi(\omega)} = \frac{1}{2} \coth(\beta/2\omega), \quad (2.49)$$

or

$$F(\omega) = \frac{1}{2} \coth(\beta/2\omega) (-i)\chi(\omega). \quad (2.50)$$

For certain choices of \hat{A} and \hat{B} , e.g. $\hat{A} = \hat{B}$ this reduces to

$$F(\omega) = \coth(\beta/2\omega) \operatorname{Im} \chi^R(\omega). \quad (2.51)$$

For these cases one can calculate $F(t)$ as

$$\begin{aligned} F(t) &= \frac{1}{\pi} \int_0^\infty d\omega \cos(\omega t) \coth(\beta/2\omega) \operatorname{Im} \chi^R(\omega) \\ &= \int_0^\infty d\omega \cos(\omega t) \coth(\beta/2\omega) S(\omega). \end{aligned} \quad (2.52)$$

Kramers Kronig-relations

We will only briefly state them for later reference. Let $f(t) = \theta(t)f(t) \in \mathbb{R}$ be a real-valued retarded function with an existing and sufficiently fast decaying Fourier-transform. Then $f(\omega)$ fulfills

$$\begin{aligned} \operatorname{Re} f(\omega) &= \frac{1}{\pi} \mathcal{P} \int_{-\infty}^\infty d\omega' \frac{\operatorname{Im} f(\omega')}{\omega' - \omega} \\ \operatorname{Im} f(\omega) &= \frac{-1}{\pi} \mathcal{P} \int_{-\infty}^\infty d\omega' \frac{\operatorname{Re} f(\omega')}{\omega' - \omega}. \end{aligned} \quad (2.53)$$

Sign of $S_{AA}(\omega)$:

$$S_{AA}(\omega) = \frac{1}{Z} (1 - e^{-\beta\omega}) \sum_{n,m} |a_{nm}|^2 e^{-\beta E_n} \delta(\omega - \omega_{mn}) . \quad (2.54)$$

In the expression above we find all terms to be positive except for those in the bracket. But we notice that

$$\begin{cases} (1 - e^{-\beta\omega}) > 0 & \text{if } \omega > 0 \\ (1 - e^{-\beta\omega}) < 0 & \text{if } \omega < 0. \end{cases} \quad (2.55)$$

So we find

$$\omega S_{AA}(\omega) > 0. \quad (2.56)$$

Eq. 2.56 has very important physical interpretation. It means that *dissipation is always positive* in a system. In the context of analytical continuation via MaxEnt it, moreover, allows us to interpret $\omega S(\omega)$ as a probability density, after proper normalization.

2.3.3 Special properties: Limiting cases

Atomic Limit

In the atomic limit the Hubbard model reduces to

$$\hat{H} = \sum_i \sum_{\alpha\beta\gamma\delta,\sigma\sigma'} U_i^{\sigma\sigma',\alpha\beta\gamma\delta} \hat{c}_{\alpha,\sigma}^{i\dagger} \hat{c}_{\beta,\sigma'}^i \hat{c}_{\gamma,\sigma'}^i \hat{c}_{\delta,\sigma}^i$$

Where the orbitals are labeled by $\alpha, \beta, \gamma, \delta$, and the atoms by i .

If, moreover, one assumes an interaction term of density-density-type, one finds find the particle number operators for each orbital to commute with the Hamiltonian $[\hat{n}^i, \hat{H}] = 0$.

Therefore, the particle number is a conserved quantity for all orbitals and the density-density correlation function becomes independent of τ . One can explicitly perform the trace to obtain

$$\begin{aligned} \mathcal{N}_{ij,\alpha\beta}^{\sigma\sigma'} &= \langle \hat{n}_i^\sigma(\tau) \hat{n}_j^{\sigma'}(0) \rangle = \langle \hat{n}_i^\sigma(0) \hat{n}_j^{\sigma'}(0) \rangle \\ &= \delta_{\sigma\sigma'} \delta_{ij} \delta_{\alpha\beta} \frac{e^{-\beta U}}{3+e^{-\beta U}} + (1 - \delta_{\sigma\sigma'} \delta_{ij} \delta_{\alpha\beta}) \frac{(1+e^{-\beta U})^2}{(3+e^{-\beta U})^2}. \end{aligned} \quad (2.57)$$

And for the local spin-spin susceptibility:

$$\begin{aligned} \chi^{\text{tot}}(\tau) &= \sum_{\alpha,\beta} \mathcal{N}_{ii,\alpha\beta}^{\uparrow\uparrow} + \mathcal{N}_{ii,\alpha\beta}^{\downarrow\downarrow} - \mathcal{N}_{ii,\alpha\beta}^{\uparrow\downarrow} - \mathcal{N}_{ii,\alpha\beta}^{\downarrow\uparrow} = \text{const.} \equiv C \\ \chi^{\text{diag}}(\tau) &= \sum_{\alpha} \mathcal{N}_{ii,\alpha\alpha}^{\uparrow\uparrow} + \mathcal{N}_{ii,\alpha\alpha}^{\downarrow\downarrow} - \mathcal{N}_{ii,\alpha\alpha}^{\uparrow\downarrow} - \mathcal{N}_{ii,\alpha\alpha}^{\downarrow\uparrow} = \text{const.} \end{aligned} \quad (2.58)$$

To establish the connection between $\chi(\tau)$ and $S(\omega)$ we can use Eq. 2.32 (shown again for better readability):

$$\chi^{\text{tot}}(\tau) = \int_{-\infty}^{\infty} d\omega S(\omega) \frac{e^{-\omega\tau}}{1-e^{-\beta\omega}}. \quad (2.59)$$

$\chi(\omega)$ can not have any contributions for finite frequencies. If it had some e.g. at $\epsilon > 0$ this would lead to a $\chi(\tau) \propto e^{-\epsilon\tau} \neq \text{const.}$. Thus the only possible form is

$$S(\omega) = \beta\omega\delta(\omega).$$

Transforming $\chi(\omega)$ onto the real time-axis leads to

$$\chi^{\text{tot}}(t) = 2\theta(t) \int_{-\infty}^{\infty} d\omega \sin(\omega t) S(\omega) = 0, \quad (2.60)$$

and

$$F(t) = \frac{1}{2} \int_{-\infty}^{\infty} d\omega \cos(\omega t) \coth(\beta/2\omega) S(\omega) = C. \quad (2.61)$$

This is an important result. The formation of a *local magnetic moment corresponds to a delta peak at $\omega = 0$* . While the susceptibility in real time is zero for this limiting case, as an effect of the commutator in its definition, the anti-commutator $F(t)$ better reflects the infinite life-time of the local spin.

A note of caution: For this limiting case different ways of analytical continuation give different results. One could for example calculate the Fourier-series

$$\chi^{\text{tot}}(i\omega_n) = \delta_{n0} C \beta.$$

Making a branch cut at the real axis and inverting the argument we get an expression with only *one* limit point:

$$f(z = \frac{1}{i\omega}) \equiv \chi(i\omega)$$

The limit point being at $z = 0$, (or equivalently $i\omega \rightarrow \infty$). By the identity theorem for holomorphic functions, $f(z)$ has a unique analytical continuation. To find the explicit form, one can calculate (all) derivatives at the limit point. By analyticity they exist, and the function's Laurent-series converges. For our case, all derivatives are zero. Therefore the analytical continuation is zero everywhere where it is defined. One may then be tempted to continue the function to the real axis and get $\chi^R(\omega) = 0$. The problem could be related to the fact that we performed a branch-cut precisely there.

The harmonic oscillator

We finish this subsection by taking a look one of the a physicists favorite toys: The harmonic oscillator.

The differential equation for a damped harmonic oscillator under a time-dependent force $f(t)$ is

$$\ddot{x} + 2\gamma\dot{x} + \omega_0^2 x = f(t)$$

Fourier-transforming the differential equation leads to

$$(\omega_0^2 - 2i\gamma\omega - \omega^2) x(\omega) = f(\omega)$$

or

$$x(\omega) = f(\omega) \frac{1}{(\omega_0^2 - 2i\gamma\omega - \omega^2) x(\omega)} \equiv f(\omega)\chi(\omega).$$

Where we defined the susceptibility of the harmonic oscillator. The roots of the denominator are at

$$\omega_{\pm} = -i\gamma \pm \sqrt{\omega_0^2 - \gamma^2}.$$

Since all poles are in the lower-half-plane we know that χ a retarded susceptibility. It's imaginary part can be used as a model for the spectral function

$$\text{Im } \chi(\omega) = \frac{2\gamma\omega}{(\omega_0 - \omega^2)^2 + 4\gamma^2\omega^2}. \quad (2.62)$$

We will see in chapter 4 how well some the spin-spin-susceptibility can be represented by this model. Transforming $\chi(\omega)$ back to time can be easily Cauchy's integral theorem.

$$\chi(t) = \begin{cases} \frac{e^{-\gamma t}}{\sqrt{\omega_0^2 - \gamma^2}} \sin(\sqrt{\omega_0^2 - \gamma^2} t) \theta(t) & \text{if } \omega_0^2 > \gamma^2 \\ \frac{e^{-\gamma t}}{\sqrt{\gamma^2 - \omega_0^2}} \sinh(\sqrt{\gamma^2 - \omega_0^2} t) \theta(t) & \text{if } \omega_0^2 < \gamma^2 \end{cases}$$

The two different solutions are usually referred to as the under- and over-damped regime. The decay life-times are $t_{\gamma} = \hbar/\gamma$ for $\omega_0^2 < \gamma^2$, and $t_{\tilde{\gamma}} = \hbar/(\gamma - \sqrt{\gamma^2 - \omega_0^2})$ for $\omega_0^2 > \gamma^2$.

$\chi(t)$ is due to its antisymmetry, i.e. the commutator of the operator in its definition, inconvenient to see the quantum-dynamical fluctuation-effects. The anti-commutator-correlation function F , instead can be expressed in ω by the fluctuation dissipation theorem and transformed into time via

$$\begin{aligned} F(t) &= \frac{1}{\pi} \int_0^\infty d\omega \cos(\omega t) \coth(\beta/2\omega) \chi^{R''}(\omega) \\ &= \frac{1}{2\pi} \int_{-\infty}^\infty d\omega \cos(\omega t) \coth(\beta/2\omega) \frac{2\gamma\omega}{(\omega_0 - \omega^2)^2 + 4\gamma^2\omega^2}. \end{aligned} \quad (2.63)$$

Performing this integral not so simple⁷. However, by using Cauchy's residue theorem, it can be solved. We close the contour-integration in a semicircle with infinite radius, referred to as "Hilfsweg", either above (for $t > 0$) or below (for $t < 0$). The "Hilfsweg" does not give a contribution to the integral. First we notice that the denominator can not be zero for real valued ω . Therefore the roots fulfill a mirror-symmetry at the imaginary and the real axis

$$\chi^i(z) = \frac{2\gamma z}{(z - Z)(z + Z)(z - Z^*)(z + Z^*)},$$

where we introduced a new function name to point out that while $\chi^i(\omega) = \text{Im} \chi(\omega)$ it can also be imaginary valued in the complex plane. (It is the analytical continuation of $\text{Im} \chi(\omega)$ in the complex plane. But since taking the imaginary part of a function is not an analytical mapping, it does not have a obvious connection to $\chi(z)$).

The mirror-symmetry of the poles comes from $F(t) = F(-t)$. For $t > 0$ we close the circle above, for $t < 0$ we close it below, but due to $F(t) = F(-t)$ the result will not change. For convenience we define $Z = \Omega + i\Gamma$ and close the circle above. We then have two poles enclosed from χ , but infinity many from $\coth(\beta/2z)$. The poles come from the Bose-Einstein-distribution and are located at $z = i\omega_n$.

$$\begin{aligned} F(t) &= \text{Re} \left[\frac{1}{2\pi} \oint dz \cos(zt) \coth(\beta/2z) \chi^i(z) \right] \\ &= \text{Re} \left[\frac{1}{2\pi} 2\pi i \sum_{n=1}^\infty \text{Res}_n + \text{Res}_\chi \right] \end{aligned} \quad (2.64)$$

Res_n can be expressed as

$$\text{Res}_n = \frac{1}{\beta} e^{i(\omega_n)t} \chi^i(i\omega_n),$$

and Res_χ (after some calculation) as

$$\begin{aligned} \text{Res}_\chi &= \frac{\gamma}{4\Gamma\Omega} (\coth(\beta/2Z)e^{iZt} - \coth(-\beta/2Z^*)e^{-iZ^*t}) \\ &= \frac{\gamma}{2\Gamma\Omega} \frac{\cos(\Omega t) \sin(\beta\Omega) + \sin(\Omega t) \sinh(\Gamma\beta)}{\cosh(\Gamma\beta) - \cos(\beta\Omega)} e^{-\Gamma t}. \end{aligned} \quad (2.65)$$

Inserting both in Eq. 2.64 we get as a final expression

$$F(t) = \frac{1}{\beta} \sum_{n=1}^\infty e^{-\omega_n t} i\chi^i(i\omega_n) + \frac{\gamma}{2\Gamma\Omega} \frac{\cos(\Omega t) \sin(\beta\Omega) + \sin(\Omega t) \sinh(\Gamma\beta)}{\cosh(\Gamma\beta) - \cos(\beta\Omega)} e^{-\Gamma t}, \quad (2.66)$$

with

$$i\chi^i(i\omega_n) = \frac{-2\gamma\omega_n}{(\omega_0^2 + \omega_n^2)^2 - 4\gamma^2\omega_n^2}.$$

⁷Actually a standard algebra program (**Mathematica**) claims that it does not converge.

From the above expressions one realizes that the life-time estimates for $F(t)$ is more complicated than for $\chi(t)$.

Of course one can might perform the numerical calculation instead. Rough estimates are given for the second term by \hbar/Γ . The first term would have as a leading order term an energy-scale $t = \hbar/\omega_{\tilde{n}}$. Where $\omega_{\tilde{n}}$ is the Matsubara-frequency closest to the maximum of $i\chi^i(i\omega_n)$ which is at $\omega_n = \frac{\sqrt{2\gamma^2 + 2\sqrt{\gamma^4 - \gamma^2\omega_0^2 + \omega_0^4} - \omega_0^2}}{\sqrt{3}}$.

2.4 Analytical continuation

We already derived the formula relating susceptibilities in imaginary time $\chi(\tau)$ with their spectral function $S(\omega)$ at lengths. For better readability we will repeat it here.

$$\begin{aligned}\chi(\tau) &= \int_{-\infty}^{\infty} d\omega \frac{e^{-\tau\omega}}{1-e^{-\beta\omega}} S(\omega) \\ &= \int_{-\infty}^{\infty} d\omega \frac{e^{-\tau\omega}}{1-e^{-\beta\omega}} \left[\frac{1}{2\pi i} \chi(\omega) \right].\end{aligned}\quad (2.67)$$

If one assumes that $S(\omega)$ is real valued (see discussion in the previous chapter) one obtains

$$\chi(\tau) = \int_{-\infty}^{\infty} d\omega \frac{e^{-\tau\omega}}{1-e^{-\beta\omega}} \left(\frac{1}{\pi} \text{Im} \chi^R(\omega) \right). \quad (2.68)$$

For the rest of this chapter, we will assume that \hat{A} and \hat{B} we chosen in a way that $S(\omega)$ is real valued.

Treating the singularity at $\omega = 0$ and other elementary manipulations:

An obvious problem when applying Eq. 2.67 to numerical data is the singularity at $\omega = 0$. We know, however, that the antisymmetric function S must (at least) behave as $\lim_{\omega \rightarrow 0} S(\omega) \propto \omega$. If it wouldn't, the measurable quantity $\chi(\tau = 0) = \langle \hat{A}\hat{B} \rangle$ would diverge. One can therefore recast Eq. 2.67 into

$$\chi(\tau) = \int_{-\infty}^{\infty} d\omega \left(\frac{e^{-\tau\omega}}{1-e^{-\beta\omega}} \omega \right) \overbrace{\left(\frac{S(\omega)}{\omega} \right)}^{\equiv A(\omega)}. \quad (2.69)$$

Now both brackets are well-behaved at $\omega = 0$. Symmetrizing the left bracket leads to

$$\begin{aligned}\chi(\tau) &= \int_{-\infty}^{\infty} d\omega \left(\frac{1}{2} \frac{e^{-\tau\omega} + e^{-(\beta-\tau)\omega}}{1-e^{-\beta\omega}} \right) A(\omega) \\ &= \int_0^{\infty} d\omega \left(\frac{e^{-\tau\omega} + e^{-(\beta-\tau)\omega}}{1-e^{-\beta\omega}} \right) A(\omega).\end{aligned}\quad (2.70)$$

To apply Eq. 2.70 to numerical data one needs to define a (not necessarily uniform) grid,

$$\begin{aligned}\chi_i &\equiv \chi(\tau_i) \\ A_j &\equiv A(\omega_j),\end{aligned}\quad (2.71)$$

which then automatically transforms Eq. 2.70 into a matrix-equation⁸

$$\begin{aligned}\chi(\tau_i) &\approx \sum_j \left(\Delta\omega_j \frac{e^{-\tau\omega_j} + e^{-(\beta-\tau_i)\omega_j}}{1-e^{-\beta\omega_j}} \omega_j \right) A(\omega_j). \\ \chi_i &\approx \sum_j K_{ij} A_j.\end{aligned}\quad (2.72)$$

As mentioned in the first chapter, numerical calculations are usually done either in imaginary time τ or in Matsubara frequencies $i\omega_n$ via a QMC-simulation. This means that $\chi(\tau_i) = \chi^{\text{exact}}(\tau_i) + \chi^{\text{error}}(\tau_i)$ is not known exactly, but deviates from its true value by an error $\chi^{\text{error}}(\tau_i)$. Inverting the integral 2.67 numerically is not possible since it is an ill-posed problem. This means that K has no inverse (e.g. $\det K = 0$.)⁹ Inverting Eq. 2.72 is equivalent to a numerically inversion of the Laplace-transformation, which is known to be an ill-defined problem.[30]

⁸We applied here a simple Riemann-sum. Generalizations to more sophisticated numerical integrations are straightforward.

⁹For an equal number of τ - and ω -grind-points

2.4.1 A first attempt

The usual approach, taught in elementary statistics lectures, to handle noisy incomplete data is to apply a χ^2 -fit. One assumes that at each point τ_i the data χ_i is centered around its true value by Gaussian distribution with mean zero and standard-deviation of σ_i . (Thus, assuming uncorrelated noise for different τ_i . If this is not the case one should diagonalize the covariance-matrix, transform data and spectral-function into this basis before continuing.[30]) A straightforward attempt to solve this problem might be to minimize the quadratic difference between

$$\bar{\chi}_i = K_{ij}A_j,$$

and the data χ_i

$$\chi^2 = \sum_i \frac{|\chi_i - \bar{\chi}_i|^2}{\sigma_i^2}.$$

Determining the spectral function $A(\omega)$ by minimizing χ^2 would work, however, rather poorly for a reasonably large number of ω_j 's. In general, if the number of fitting-parameters (number of A_j 's) is of the same order of magnitude as the number of data-points (number of χ_i 's) a fitting procedure will over-fit. Usually, the necessary number frequency-points will be larger than the number of data-points, since a (possibly quite spiky-function) on an interval from zero to infinity needs to be represented rather than (a smooth convex function on) an interval from zero to $\beta/2$. Nonetheless, if one has a very specific idea about the $A(\omega)$ (e.g. an model to extract effective lifetimes of spin-excitations) with few free parameters, minimizing χ^2 can still be an reasonable approach.

2.4.2 Maximum entropy method:

In this subsection we follow closely the derivations of the work by Jarrell[30].

A number of more general methods for preventing over-fitting have been developed. The Maximum-Entropy method, which is probably the best established method for analytical continuation of QMC data, maximizes (instead of minimizing χ^2) the functional $F[\alpha, A, m]$

$$\begin{aligned} F[A, m, \alpha] &= \alpha S[A, m] - \frac{1}{2}\chi^2[A] \\ \left. \frac{\delta F}{\delta A} \right|_{A^{\text{opt}}} &= 0. \end{aligned} \tag{2.73}$$

Here S is the generalized Shannon-Jaynes entropy

$$S[A, m] = \int d\omega \left(A(\omega) - m(\omega) - A(\omega) \ln \left(\frac{A(\omega)}{m(\omega)} \right) \right). \tag{2.74}$$

The model function $m(\omega)$ incorporates prior knowledge. Notice, that in the absence of data, the maximum of F is at $A(\omega) = m(\omega)$. It should be remarked that explicit form of the entropy term S is based on information theory incorporating the knowledge that $A(\omega)$ is a positive additive distribution. The functional F can be derived from maximizing the conditional probability $P(A|\chi)$.

The most probable parameter $\hat{\alpha}$ is determined for the *classical* MaxEnt (in the terminology of [30]) via probabilistic arguments. In *Bryan's approach* (in the terminology of [31]) a spectral function $A[\chi, \alpha]$ for each α -value is calculated, as well as a probability for each α value $P(\alpha)$. The final spectrum is then computed as

$$A[\chi] = \int d\alpha P(\alpha) A[\chi, \alpha].$$

Since $P(\alpha)$ is usually sharply peaked around $\hat{\alpha}$ (just one parameter determined by a large number of data) Bryan's approach and classic MaxEnt agree usually very well with one another.

Normalization:

MaxEnt interprets $A(\omega)$ as a probability density. This requires besides positivity (which is givens since $\omega S(\omega) > 0$) normalization. Normalization can be achieved by using the KK-relation

$$\begin{aligned} \int_{-\infty}^{\infty} d\omega A(\omega) &= \int_{-\infty}^{\infty} d\omega \frac{S(\omega)}{\omega} \\ &= \int_{-\infty}^{\infty} d\omega \frac{\frac{1}{\pi} \text{Im} \chi^R(\omega)}{\omega} \\ &= \text{Re} \chi^R(0) \\ &= \chi(i\omega_n = 0) \\ &= \int_0^{\beta} d\tau \chi(\tau). \end{aligned} \tag{2.75}$$

It is therefore sufficient to normalize the data $\chi(\tau)$.

As a very simple check, one may apply this to the previously discussed atomic limit $\int_{-\infty}^{\infty} \frac{S(\omega)}{\omega} = \int_{-\infty}^{\infty} \frac{C\beta\omega\delta(\omega)}{\omega} = C\beta = \chi(i\omega = 0)$. It is reassuring to find Eq. 2.75 to be valid also in this pathological case. However, one should be careful. E.g., when performing the KK-relation integrals and limits can not be exchanged. For example if we would attempt to calculate (in the atomic limit) $\text{Re} \chi^R(0) = \lim_{\omega \rightarrow 0} \text{Re} \chi^R(\omega) = \lim_{\omega \rightarrow 0} 0 = 0$, this would yield a wrong renormalization.

2.4.3 "Kink" selection criteria for α

In this subsection we introduce an alternative way of determining the parameter α . The main reason for using this technique (scaling-invariance of the error) will be motivated and explained in detail.

In the previous section we mentioned that in the absence of data MaxEnt would simply give the model $m(\omega)$ as a result. Since no data is equivalent to $\alpha \gg \frac{1}{2} \frac{\chi^2}{S}$, we see that for large α the data would be under-fitted. For $\alpha \ll \frac{1}{2} \frac{\chi^2}{S}$, instead, MaxEnt would reduce to a simple χ^2 fit, which would over-fit the data. The main question, then, is how to determine the appropriate α . Fig. 2.3 shows $\chi^2(\alpha)$ in a log-log-plot. The main-feature of interest is the region where the (logarithmic) slope of χ^2 changes drastically. In this region, we find the under-fitting to stop, and the data to be taken into account appropriately. The corresponding "optimal" α can be extracted by re-plotting the function as shown on the right side of Fig 2.3.

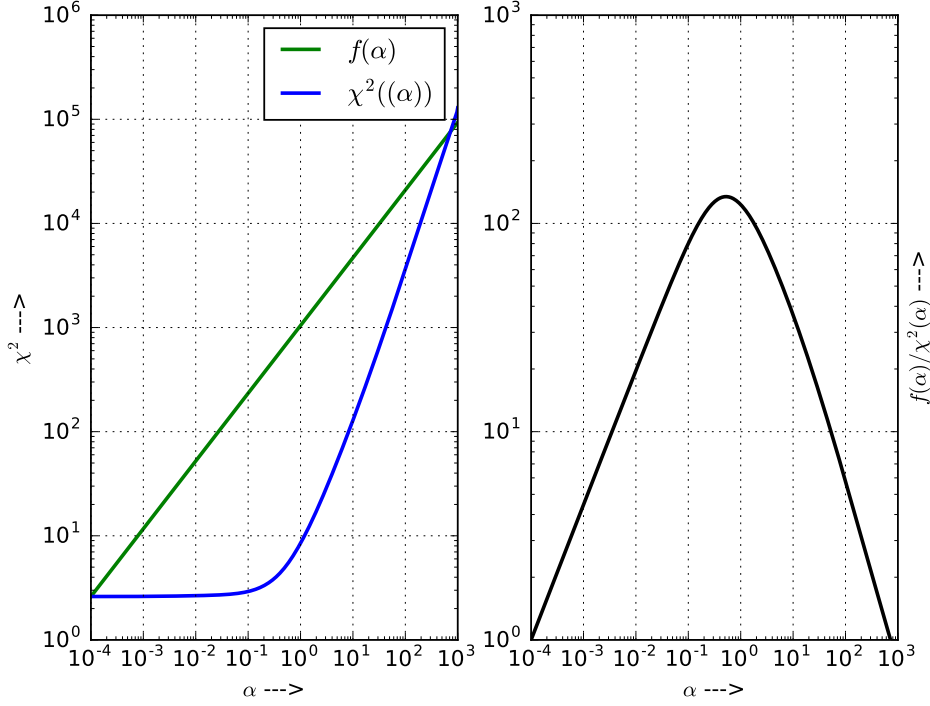


Figure 2.3: Log-log-plot of the quadratic difference between the data and the fit χ^2 over the parameter α .

Since the optimal α is selected by determining the "kink" in the log-log-plot of $\chi^2(\alpha)$ we refer to it as "*kink*" selection criteria.

This is especially useful when facing a problem where the standard-errors σ_i are only known up to a scaling-factor s . The fact that the resulting spectral-function is invariant from the scaling-factor s , can be seen from

$$\begin{aligned}
 F[A, m, s, \alpha] &= - \int d\tau \frac{(\chi(\tau) - \int d\omega K(\tau, \omega) A(\omega))^2}{(s \sigma(\tau))^2} + \alpha S[A] \\
 &= \frac{1}{s^2} \left[- \int d\tau \frac{(\chi(\tau) - \int d\omega K(\tau, \omega) A(\omega))^2}{(\sigma(\tau))^2} + \underbrace{\alpha s^2}_{\tilde{\alpha}} S[A] \right]. \quad (2.76) \\
 &= \frac{1}{s^2} F[A, m, \tilde{\alpha}]
 \end{aligned}$$

So $A^s(\omega)$ (which one would determine from $\frac{\delta}{\delta A} F[A, s, m] = 0$) is the same as $A(\omega)$ for $\alpha \rightarrow \tilde{\alpha}$. However, α is not a free parameter, so $A^s(\omega) = A(\omega)$. In practice, slight deviations between $A^s(\omega)$ and $A(\omega)$ can occur due to discretized α , ω , and τ .

We have used the "Kink" selection-criteria for the analytical continuation of the spin-spin-susceptibilities.

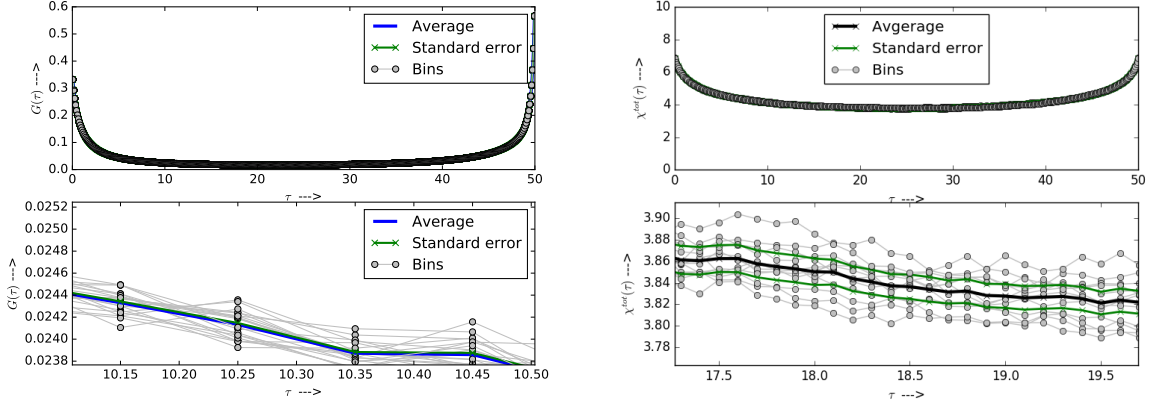


Figure 2.4: QMC-bins (connected gray lines) and average values (blue/black) for $G^{3z^2-r^2}(\tau)$ (left) and $\chi^{\text{tot}}(\tau)$ (right). Each "bin" corresponds to a measurement of $\chi(\tau)$ on a separate processor-core with the same parameters. The data is taken from our DFT+DMFT calculation, for $FeTe$ in the d -only model with *full* U interaction and FLL DCC. (See sec. 3). Only 12 bins are shown. In the real calculation 64 were used for the bootstrap procedure.

Fig. 2.4 shows QMC-bins (gray) and average values (red) and standard-errors for $G(\tau)$ (left panel) and $\chi(\tau)$ (right panel). In the left panel (G) the assumption of independent $G(\tau_i)$ measurements for each bin is a reasonable (each gray line-crosses the red line several times). While the same does not apply to the right panel (χ). For completely independent measurements (and locally constant χ)¹⁰ a gray line should have a 50% chance of crossing the average. We find most of the bins to never cross the average. Each curve, however, is reasonably smooth. Calculating an error-estimate (e.g. by a bootstrap-algorithm) would give a value that is significantly too large. This would be an example where the error is not known only up to a scaling factor s , and the "kink"-selection criteria may have advantages.

¹⁰Which is reasonably well fulfilled for a small distance between neighboring τ_i 's.

2.4.4 Sparse modeling

This section is adapted from [32] to our notation. One of the newer methods for the analytical continuation of imaginary-time data is sparse-modeling[32]. It starts by applying a singular value decomposition (SVD) of the matrix K (after proper discretization in ω and τ) into a diagonal matrix S and two orthogonal matrices

$$K = USV^t.$$

U and V define automatically a basis in τ and ω . Transforming the data χ as well as the spectral function A into this basis yields

$$\begin{aligned} \chi' &= U^t \chi \\ A' &= V^t A \end{aligned} \quad (2.77)$$

Instead of finding the minimum of the functional Eq. 2.73 the function

$$F(A') = \frac{1}{2} \|\chi' - SA'\|_2^2 + \lambda \|A'\|_1,$$

where $\|\cdot\|_1$ denotes the L_1 ("taxicab") norm. The positive parameter λ , which takes the role of α , can be determined by the kink-method. The main advantage of this method is that the additional term makes F convex. So one can find the minimum of F without difficulty. The resulting function, however, will not be the most probable spectral function for a given the dataset. The L_1 regularization leads to very efficient basis that approximately describes the physical problem.

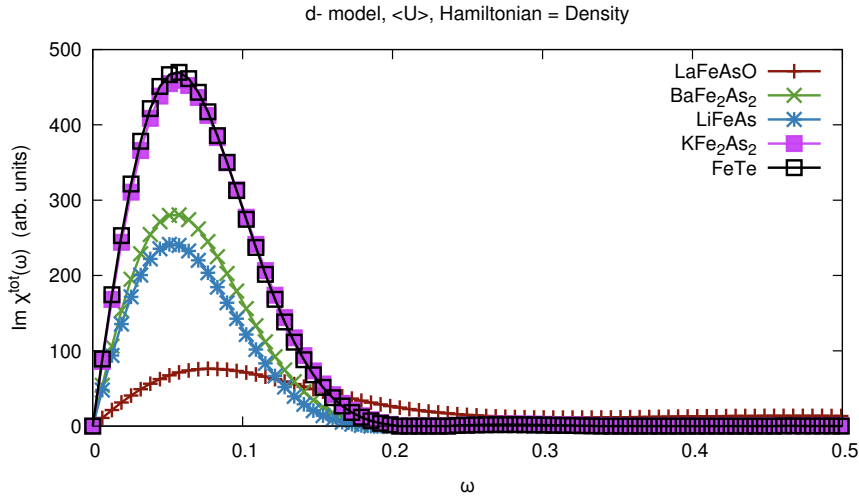


Figure 2.5: Comparison of $\text{Im } \chi^{tot}(\omega)$ obtained via SpM .

In our numerical analysis, we find the SpM approach to have problems if a peak is located below $\approx 50\text{meV}$. (See Fig. 2.5). We think that basis-elements corresponding to a low-energy peak are particularly targeted by the L_1 regularization. If this is correct, it would mean that SpM is not capable of describing the formation of a local magnetic moment.

Chapter 3

Parameters and Assumptions for DFT+DMFT

In this chapter we will discuss the general setup and the underlying assumptions of our study. In particular we will illustrate the ab-initio input of our DMFT calculation, namely the DFT and cRPA data obtained by the Würzburg group. Our own DMFT results are shown in the next chapter while the comparison between the different parent compounds, representative of the most important families of Fe-based SC, is given in chapter 5.

The first step of a DFT+DMFT calculation is defining the low-energy (target) orbital manifold, which will be considered for the d/dp DMFT treatment. Once this choice is made the main parameters in the Hamiltonian are the total number of electrons in the target-orbital manifold (n_0), the (DFT) dispersion relation $\epsilon^i(\vec{k})$, the Coulomb-overlap integrals for all orbitals (U , J and V) an appropriate double-counting correction μ_{DCC} and the inverse temperature β . We will discuss the values for the different parameters and the underlying assumptions in detail in the following sections.

3.1 Target orbitals $\epsilon^i(\vec{k})$

The target-orbital manifold for DMFT calculation are naturally the most correlated ones closest to the Fermi-energy. For all the Fe -SC materials under consideration in this work the $3d$ -orbitals of iron are the ones of interest. However, the p -manifold of the corresponding pnictogene-/ chalcogen- element(s) might also display a not negligible hybridization with the five $3d$ -orbitals of Fe . This poses the question of the most appropriate choice of target space for these compounds. At a first glance it might seem evident to prefer a larger Wannier-basis-set, which includes also the corresponding pnictogene-/ chalcogen p -orbitals, known as dp -/ dpp -*model*, over a Wannier-basis set containing only the Fe d -orbitals, known as d -*model* since it being closer to the solid-state Hamiltonian. However, to take the p -manifold fully into account is computationally unfeasible, at DMFT/ Cluster-DMFT level, since the dimension of the Hilbert-space scales exponentially with the number of orbitals. Thus, it is (at the moment) only possible to take the Fe d -orbital fully (at the level of a Hubbard Hamiltonian) into account. The p -orbitals, whose complete inclusion would require non-local interactions

beyond the simple DMFT-level¹, are usually considered at the DFT level, which hence will be reflected, in the appearance of the DMFT Hamiltonian, at the corresponding orbital-dependent dispersion relation $\epsilon^i(\vec{k})$, where i is the orbital index. As for the cRPA estimate of the interaction, one should also keep in mind that, a larger number of target-orbitals will also reduce the screening, and thus enhance U, J and V values of the Hubbard-interaction with respect to the corresponding d -only models.

Hence, in general, how to choose the "optimal" target space (e.g. d - vs dp - / dpp) for a DFT+DMFT calculation of a specific material can become a very hard question to answer. (For a general discussion of this problem, we refer to[33][34]).

To address this question in the specific cases of interest we calculated all of the materials considered in this work with both models.

The DFT-orbital structure for all our materials was obtained by Martin Edelmann (Würzburg group) via *Vienna Ab initio simulation package* (VASP) [20] (green in the following figures) and later fitted to the maximally localized function (of d - or dp - / dpp - type) via the software package *wannier90* (red in the following figures). These maximally localized orbitals are assumed to build the local basis for the subsequent DMFT treatment.

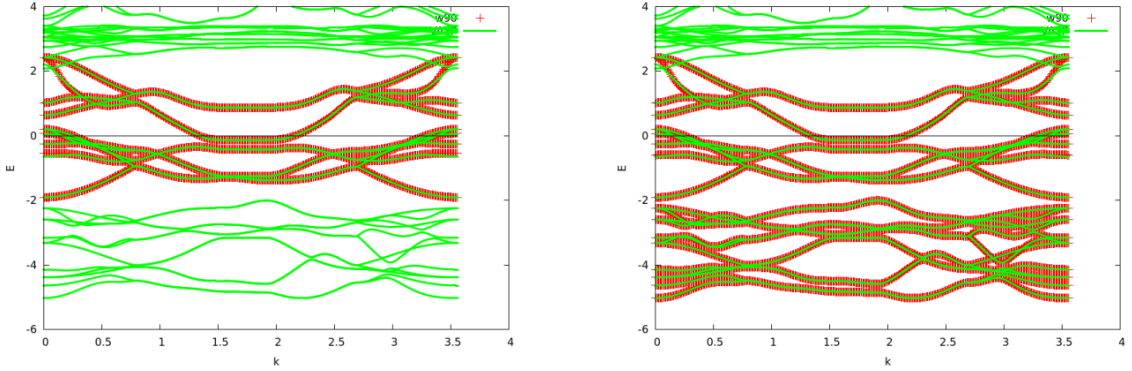


Figure 3.1: Comparison of the orbital fit of the electronic dispersion for the d -model (left) and the dpp -model (right) for LaFeAsO.

In Fig. 3.1 we see that the d -bands for LaFeAsO of Fe are reasonably well separated from the p -manifolds of arsenic and oxygen. The p bands are located (accordingly of an DFT calculation) well below the Fermi-energy which is set to zero. The d -model seems to fit the total orbital structure already very well. This would suggest that using the d -model is well justified for LaFeAsO. If one, however, wants to go beyond the d -model, additional features must be considered. The oxygen p -bands are not well separated from the arsenic p -bands. Including only one of them (e.g. only the arsenic $4p$ -bands) would lead to wrong results. One needs to include either both p - manifolds, resulting in the so called dpp -model, or none of them.

In figure 3.2 we see that the d -bands for LiFeAs of Fe are not as well separated as for LaFeAsO. We also find that the dp -model improves the matching of the electronic-structure. See e.g. that the difference between the green and the red curve at the proximity of $k=3.2$.

¹Moreover at the DMFT level non-local interactions are reduced to the Hartree-contribution which are already included in DFT.

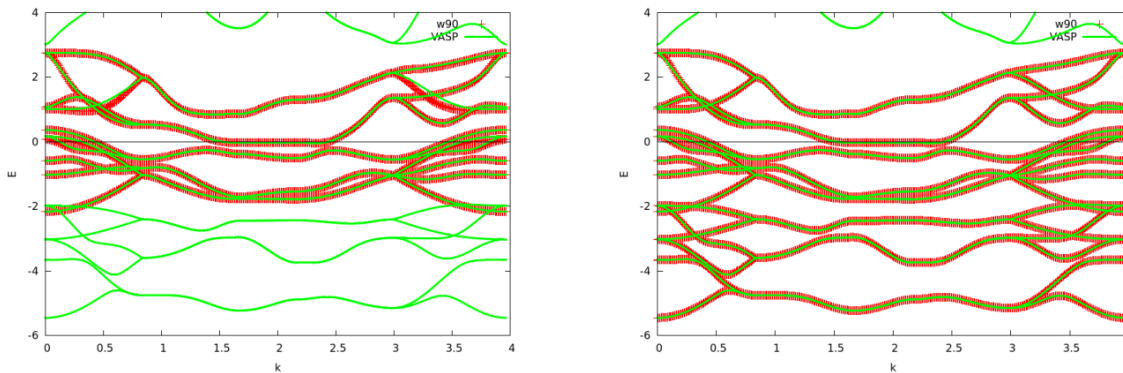


Figure 3.2: Comparison of the orbital fit of the electronic dispersion for the d -model (left) and the dp -model (right) for LiFeAs.

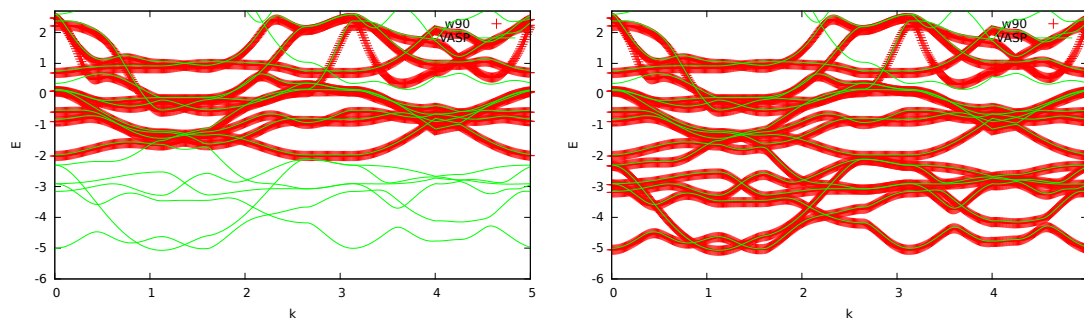


Figure 3.3: Comparison of the orbital fit of the electronic dispersion for the d -model (left) and the dp -model (right) for BaFe₂As₂.

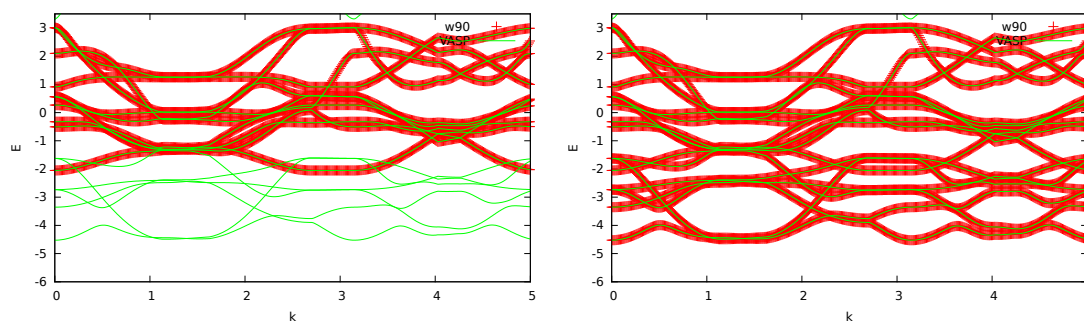


Figure 3.4: Comparison of the orbital fit of the electronic dispersion for the d -model (left) and the dp -model (right) for KFe₂As₂.

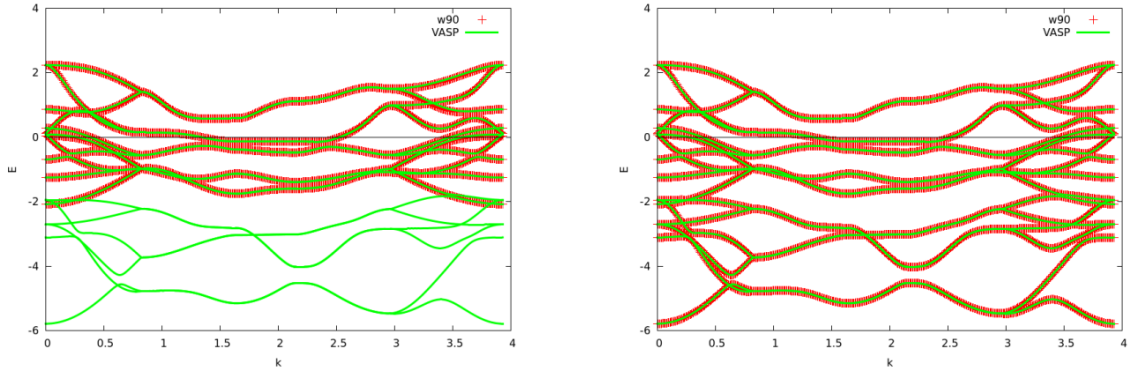


Figure 3.5: Comparison of the orbital fit of the electronic dispersion for the d -model (left) for FeTe.

In figure 3.5 we see that the d -bands (for FeTe) of Fe are reasonably well reproduced close in the proximity of the Fermi-energy. Close to the Γ -point ($k=0$) there is an overlap between the Fe d -bands and the Te p -bands. Moreover, we find one band to be very flat slightly below the Fermi-energy, which suggest a very large DOS at this energy ($-0.2eV$).

Comparing the left panel of Fig. 3.5 to the right panel we find that the dp -/ dpp -model fits the orbital-structure better in the proximity of the Fermi-energy. This is due to the increased number of fitting parameters (more bands).

For the Fe-SC calculations considered the d -manifold always belongs to the Fe whereas the p -manifold(s) correspond to different elements of the pnictogene-/ chalcoge- group. While one could in principle also determine the crystal-structure, including the lattice parameters, from a more sophisticated DFT calculation (applying the Hellman-Feynman-theorem to find the total energetic minimum) in our cases the experimentally found crystal-structures given in Tab. 3.1 have been used as input for the DFT calculation.

Material	Crystal structure
LaFeAsO	ZrCuSiAs-type
LiFeAs	PbFCl-type tetragonal
BaFe ₂ As ₂	ThCr ₂ Si ₂ -type
KFe ₂ As ₂	ThCr ₂ Si ₂ -type
FeTe	PbO-type

Table 3.1: Crystal structures for all materials under consideration[35][8].

3.1.1 Filling n_0 :

An extremely important parameter for the DMFT calculation is the total number of electrons per correlated iron atom. While the electrons can be redistributed between the different orbitals during the DMFT calculation, the sum over all orbitals is a constant value. As a starting point

of our discussion, the atomic orbital configuration as well as the electronegativity of the atomic consistence of our Fe-SC is given in table 3.2. From the atomic-orbitals and the electronegativity, we can extract a fist rough estimate of the number of electrons per iron atom to be considered.

Name	Chemical element	Atomic orbital configuration	Electronegativity
Iron	Fe	[Ar]3d ⁶ 4s ²	1.64
Oxygen	O	[He]2s ² 2p ⁴	3.50
Arsenic	As	[Ar]3d ¹⁰ 4s ² 4p ³	2.20
Tellurium	Te	[Kr]4d ¹⁰ 5s ² 5p ⁴	2.01
Lanthanum	La	[Xe]5d ¹ 6s ²	1.10
Barium	Ba	[Xe]6s ²	0.97
Lithium	Li	[He]2s ² 2p ¹	0.97
Potassium	K	[Ar]4s ¹	0.91

Table 3.2: Chemical elements, atomic orbital configuration and electronegativity for the constituents of the considered materials. For the electronegativity the Allred-Rochow-values are given.

LaFeAsO: Oxygen has by far the highest electronegativity. Thus it will attract two electrons it to it's 2p shell. Arsenic has the second highest electronegativity so it will also try to fill its 2p-shell, for which it needs three electrons. Lanthanum, on the other hand, has a high tendency to donate its three electrons, hence remaining in a stable [Xe] configuration. Thus, on average each iron atom will give away two electrons. These will come from the energetically unfavorable 4s shell. So each iron atom will have approximately 6 electrons in its d-shell. This will be reflected in the following choice for the total filling of the corresponding d - (dpp-) calculation: $n_0^{\text{d-model}} = 6$ and $n_0^{\text{dpp-model}} = n_0^{\text{d-model}} + n_{2\text{p-shell}}^{\text{Oxygen}} + n_{4\text{p-shell}}^{\text{Arsenic}} = 6 + 6 + 6 = 18$.

LiFeAs: Lithium has a small electronegativity and thus a strong tendency to donate one electron. Arsenic on the other hand has a high electronegativity and three orbital-slots to occupy. One will come from arsenic and the other two electrons will be donated by the Fe 4s² shell. So iron will have again approximately 6 electrons in its d-shell on average. Thus $n_0^{\text{d-model}} = 6$ and $n_0^{\text{dp-model}} = n_0^{\text{d-model}} + n_{4\text{p-shell}}^{\text{Arsenic}} = 6 + 6 = 12$.

BaFe₂As₂: Barium will donate its two s-electrons, whereas arsenic will try to fill its 4p orbital fully. Keeping in mind that there are two As and Fe atoms per unit-cell we get $n_0^{\text{d-model}} = 6$ and $n_0^{\text{dp-model}} = n_0^{\text{d-model}} + n_{4\text{p-shell}}^{\text{Arsenic}} = 6 + 6 = 12$.

KFe₂As₂: The argument for KFe_2As_2 is very similar as for $BaFe_2As_2$. However, potassium has one electron less to donate than barium. This leads to half an electron less on average per iron atom. We get thus $n_0^{\text{d-model}} = 5.5$ and $n_0^{\text{dp-model}} = n_0^{\text{d-model}} + n_{4\text{p-shell}}^{\text{Arsenic}} = 5.5 + 6 = 11.5$

FeTe: Tellurium has a higher electronegativity than iron. Therefore one can assume that its 5p shell will get two electrons from the 4s shell of iron. This leaves again 6 electrons in the 3d shell of iron. Thus $n_0^{\text{d-model}} = 6$ and $n_0^{\text{dp-model}} = n_0^{\text{d-model}} + n_{5\text{p-shell}}^{\text{Tellurium}} = 6 + 6 = 12$ again.

It is important to keep in mind that the above estimates for the number of electrons are quite rough. However, while a fully self-consistent determination of the charge per *Fe* atom would in principle be possible (E.g. by charge self-consistent DFT+DMFT [36] or via fully self-consistent GW approximation [37]), it is beyond the scope of this thesis.

3.2 Coulomb-overlap integrals (cRPA)

The results of the cRPA calculation are taken from Miyake, et al [21]. We will only show the relevant parameters for the DMFT calculation. While we give a brief discussion of the physical interpretation we must refer for a more detailed discussion to Ref. [21].

In Tab.3.3 we show the effective local Coulomb interaction U as well as the local exchange interaction terms (Hund's coupling) J for the d -model. Table 3.4 shows the same quantities for the dp - / dpp -model. Comparing the two tables we find (for the same material), especially the local Coulomb interaction U , to be significantly larger for the dp/dpp -case. This is due to two effects somewhat related effects. First, the maximally localized Wannier orbitals are in general narrower for the dp - / dpp -model due to the larger number of available fitting parameters (larger number of KS-orbitals). Evidently, a stronger localization will lead to larger Hubbard- U -terms. The second effect is the number of available screening channels. The cRPA calculation is constricted in the sense that the target-orbitals must not contribute to the screening to avoid double-counting². This smaller number of screening channels for the dp - / dpp -case is another reason for the increase of the local Coulomb interaction.

Another important feature is the orbital-dependence of the U -values. We find that for the d -model the orbital-dependence is significantly larger than for the dp - / dpp -model (for example the ratio between the largest and the smallest U_{ii} -value ranges for the d -model from 1.26 to 1.59, but for the d -model only between 1.05 and 1.17). This can again be understood from broader Wannier-functions in the d -model. A broader spread of the Wannier-functions leads to a stronger hybridization and thus to strongly orbital-dependent parameters. This is very important to answer the question whether using average U, V and J values is justified. In this context, it would be more justified for the dpp -model, but not for the d -model. At the same time, if we look at the exchange-terms J we find them to be much less affected to the models. Since the exchange terms J are dipole-terms rather than monopole-terms they are -in general- less sensitive to screening. The ratio of the largest to the smallest J value is approximately 2, which suggests that taking the average values would result indeed in a non-negligible error.

²In the context of RPA. The double counting of DFT still needs to be corrected separately within the DFT+DMFT algorithm. See following subsection.

LaFeAsO	U					J				
	$3z^2 - r^2$	xz	yz	$x^2 - y^2$	xy	$3z^2 - r^2$	xz	yz	$x^2 - y^2$	xy
$3z^2 - r^2$	2.84	1.97	1.97	1.51	1.78	$3z^2 - r^2$	0.33	0.33	0.42	0.57
xz	1.97	2.43	1.62	1.52	1.8	xz	0.33	0.37	0.35	0.46
yz	1.97	1.62	2.43	1.52	1.8	yz	0.33	0.37	0.35	0.46
$x^2 - y^2$	1.51	1.52	1.52	1.91	1.91	$x^2 - y^2$	0.42	0.35	0.35	0.23
xy	1.78	1.8	1.8	1.91	3.03	xy	0.57	0.46	0.46	0.23
BaFe₂As₂	U					J				
	$3z^2 - r^2$	xz	yz	$x^2 - y^2$	xy	$3z^2 - r^2$	xz	yz	$x^2 - y^2$	xy
$3z^2 - r^2$	3.28	2.21	2.21	1.77	1.99	$3z^2 - r^2$	0.36	0.36	0.5	0.6
xz	2.21	2.64	1.77	1.72	1.94	xz	0.36	0.4	0.41	0.48
yz	2.21	1.77	2.64	1.72	1.94	yz	0.36	0.4	0.41	0.48
$x^2 - y^2$	1.77	1.72	1.72	2.29	2.16	$x^2 - y^2$	0.5	0.41	0.41	0.26
xy	1.99	1.94	1.94	2.16	3.18	xy	0.6	0.48	0.48	0.26
LiFeAs	U					J				
	$3z^2 - r^2$	xz	yz	$x^2 - y^2$	xy	$3z^2 - r^2$	xz	yz	$x^2 - y^2$	xy
$3z^2 - r^2$	3.58	2.52	2.52	2.15	2.27	$3z^2 - r^2$	0.36	0.36	0.54	0.6
xz	2.52	2.96	2.08	2.11	2.23	xz	0.36	0.39	0.44	0.47
yz	2.52	2.08	2.96	2.11	2.23	yz	0.36	0.39	0.44	0.47
$x^2 - y^2$	2.15	2.11	2.11	2.85	2.54	$x^2 - y^2$	0.54	0.44	0.44	0.28
xy	2.27	2.23	2.23	2.54	3.39	xy	0.6	0.47	0.47	0.28
FeTe	U					J				
	$3z^2 - r^2$	xz	yz	$x^2 - y^2$	xy	$3z^2 - r^2$	xz	yz	$x^2 - y^2$	xy
$3z^2 - r^2$	3.84	2.57	2.56	2.44	2.5	$3z^2 - r^2$	0.37	0.37	0.66	0.68
xz	2.57	2.88	2.03	2.29	2.34	xz	0.37	0.37	0.49	0.49
yz	2.56	2.03	2.88	2.29	2.34	yz	0.37	0.37	0.49	0.49
$x^2 - y^2$	2.44	2.29	2.29	3.59	3.04	$x^2 - y^2$	0.66	0.49	0.49	0.34
xy	2.5	2.34	2.34	3.04	3.84	xy	0.68	0.49	0.49	0.34

Table 3.3: Effective on-site Coulomb (U)exchange (J) interactions between two electrons on the same iron site in the d model for all combinations of Fe-3d orbital (in eV) (from [21] but reordered)

LaFeAsO		U					J				
	$3z^2 - r^2$	xz	yz	$x^2 - y^2$	xy		$3z^2 - r^2$	xz	yz	$x^2 - y^2$	xy
$3z^2 - r^2$	4.33	3.31	3.31	2.81	2.99	$3z^2 - r^2$		0.45	0.45	0.67	0.74
xz	3.31	4.08	2.9	2.91	3.09	xz	0.45		0.56	0.59	0.63
yz	3.31	2.9	4.08	2.91	3.09	yz	0.45	0.56		0.59	0.63
$x^2 - y^2$	2.81	2.91	2.91	3.98	3.57	$x^2 - y^2$	0.67	0.59	0.59		0.37
xy	2.99	3.09	3.09	3.57	4.66	xy	0.74	0.63	0.63	0.37	
BaFe₂As₂		U					J				
	$3z^2 - r^2$	xz	yz	$x^2 - y^2$	xy		$3z^2 - r^2$	xz	yz	$x^2 - y^2$	xy
$3z^2 - r^2$	5.45	4.33	4.33	3.71	3.84	$3z^2 - r^2$		0.49	0.49	0.75	0.78
xz	4.33	5.19	3.86	3.81	3.95	xz	0.49		0.64	0.66	0.68
yz	4.33	3.86	5.19	3.81	3.95	yz	0.49	0.64		0.66	0.68
$x^2 - y^2$	3.71	3.81	3.81	4.97	4.4	$x^2 - y^2$	0.75	0.66	0.66		0.39
xy	3.84	3.95	3.95	4.4	5.4	xy	0.78	0.68	0.68	0.39	
LiFeAs		U					J				
	$3z^2 - r^2$	xz	yz	$x^2 - y^2$	xy		$3z^2 - r^2$	xz	yz	$x^2 - y^2$	xy
$3z^2 - r^2$	4.33	3.31	3.31	2.81	2.99	$3z^2 - r^2$		0.45	0.45	0.67	0.74
xz	3.31	4.08	2.9	2.91	3.09	xz	0.45		0.56	0.59	0.63
yz	3.31	2.9	4.08	2.91	3.09	yz	0.45	0.56		0.59	0.63
$x^2 - y^2$	2.81	2.91	2.91	3.98	3.57	$x^2 - y^2$	0.67	0.59	0.59		0.37
xy	2.99	3.09	3.09	3.57	4.66	xy	0.74	0.63	0.63	0.37	
FeTe		U					J				
	$3z^2 - r^2$	xz	yz	$x^2 - y^2$	xy		$3z^2 - r^2$	xz	yz	$x^2 - y^2$	xy
$3z^2 - r^2$	6.18	5.23	5.23	4.69	4.6	$3z^2 - r^2$		0.5	0.5	0.81	0.78
xz	5.23	6.29	4.85	4.91	4.81	xz	0.5		0.69	0.72	0.69
yz	5.23	4.85	6.29	4.91	4.81	yz	0.5	0.69		0.72	0.69
$x^2 - y^2$	4.69	4.91	4.91	6.37	5.42	$x^2 - y^2$	0.81	0.72	0.72		0.41
xy	4.6	4.81	4.81	5.42	6.09	xy	0.78	0.69	0.69	0.41	

Table 3.4: Effective on-site Coulomb (U)exchange (J) interactions between two electrons on the same iron site in the $dp - /dpp$ model (in eV) (from [21] but reordered)

3.2.1 Average U , J and V

It is very appealing to use averaged interaction terms for several reasons. First the model becomes simpler, not only from a conceptual point of view, but also by means of computation. If for example one assumes orbital-independent (for the same angular momentum quantum-number) U, V and J values and moreover the spherical symmetry relation $V = U - 2J$ the frequently used Kanamori-Hamiltonian has full $U(1)_C \otimes SU(2)_C \otimes SO(3)_O$ symmetry for the charge C , spin S and the orbitals O (see e.g. [18]). Since the Hamiltonian is block diagonal with respect to the corresponding quantum numbers, the computational power needed is decreased by orders of magnitude³. Another very important aspect is the DCC. If (due to some symmetry reason, for instance) in the d -model, all d -orbitals have the same interaction parameters one can absorb the, usually very problematic, DCC into the chemical potential. The chemical potential, however, is no external parameter, but determined within in the DMFT self-consistency cycle. Thus, for these cases there would be no DCC problem. For these reasons averaged U, V and J values are widely used for the calculation of iron-based SC. Their usage, however, can not be justified for all cases. We will come back to this point in the next two chapters where we will compare DFT+DMFT results for averaged and non-averaged interaction terms. The averaged local Coulomb interactions can be computed as⁴

$$\begin{aligned}
 \bar{U} &= \frac{1}{(2l+1)} \sum_i U_{ii} \\
 \bar{J} &= \frac{1}{2l(2l+1)} \sum_{\substack{ij \\ i \neq j}} J_{ij} \\
 \bar{V} &= \bar{U} - 2\bar{J}.
 \end{aligned} \tag{3.1}$$

After applying Eq. 3.1 to all materials we get:

	d -model			$dp - /dpp$ -model		
	\bar{U}	\bar{J}	\bar{V}	\bar{U}	\bar{J}	\bar{V}
LaFeAsO	2.53	0.39	1.75	4.23	0.57	3.09
BaFe ₂ As ₂	2.81	0.43	1.95	5.24	0.62	4.00
KFe ₂ As ₂	2.81	0.43	1.95	5.24	0.62	4.00
LiFeAs	3.15	0.43	2.29	5.94	0.62	4.7
FeTe	3.41	0.48	2.45	6.24	0.65	4.94

Table 3.5: Average effective on-site Coulomb (U) exchange (J) interactions between two electrons on the same iron site in the d - and $dp - /dpp$ - model (in eV). Regarding KFe_2As_2 we must remark that these are not given in [21]. Due to a similar crystal-structure as $BaFe_2As_2$ we have assumed the interaction terms to be identical.

³For example for the density-density interaction the particle number-operator commutes with H^{int} which significantly simplifies the problem. Moreover very efficient QMC-solvers (segment-code for this specific example) have been developed for these cases.

⁴for spherical (atomic) symmetry these would be equivalent to the *Kanamori*-averages.

3.3 Double Counting Correction (DCC)

One of the most severe problem of DFT+DMFT calculations is arguably the so called "double-counting". It arises from the interaction effects already included at the level of the DFT calculation. This part of the interaction (Hartree-interaction and others depending on the exchange-correlation functional) must be subtracted in the DMFT calculation⁵. This is, however, not a trivial task since DFT is a non-diagrammatic method whereas DMFT is. Therefore coupling these two methods neat-less together is rather involved task.

While there are several correction terms and recipes published, the most commonly used are the around-mean-field (AMF) approximation and the fully-localized limit (FLL). Both are strictly valid only for limiting cases and naturally give better results if the physical situation under consideration is at least close to one of these limiting cases.

The AMF approximation works well whenever the mean-field approximation is well justified. This is, for example in normal metals the case. For other materials, like isolators, it gives wrong results, there it is better to use the opposite limiting case, the FLL.⁶

For the iron-pnictide/-chalcogenide-SC, it is not immediately clear which DCC should be preferred. Completely separated Hubbard-orbitals, as we would get for very larger U terms, would be better described by FLL-DCC, whereas iron, being a metal, the use of AMF DCC. It was, however, shown by [38] that for *LaFeAsO* FLL gives better results than AMF. This is especially interesting since *LaFeAsO* has the smallest U , V and J values⁷. Thus for *LaFeAsO* an AMF-treatment would actually be more justified than for the others. So if FLL-DCC is well justified for *LaFeAsO* it should also be well justified for our other materials. Therefore we chose FLL-DCC for all our materials. To see the effect of DCC we decided to calculate the AMF case for one of our intermediately correlated materials (BaFe_2As_2) as well.

As mentioned before, using average U and J values are, especially in the d -model, not always justified. For orbital dependent interactions the DCC also becomes orbital dependent. They can be calculated as (See supplementary material of [39]):

$$\begin{aligned}\mu_{DC}^{AMF}(i) &= n^0 \left(\sum_j U_{ij} + \sum_{j,j \neq i} (U_{ij} - J_{ij}) \right) \\ \mu_{DC}^{FLL}(i) &= \mu_{DC}^{FLL}(i) + \frac{1}{4} \left(n^0 - \frac{1}{2} \right) \left(\sum_j (U_{ij} - J_{ij}) \right),\end{aligned}\tag{3.2}$$

where

$$n^0 = \frac{1}{2(2l+1)} \sum_{i,\sigma} n_{i,\sigma}\tag{3.3}$$

is the DFT filling. This gives Tab. 3.6. and can be entered in int *w2dynamics*[19] as

$$\text{dc} = -9.5295, -8.9790, \dots,$$

where is is important to compensate for the unusual sign-convention in *w2dynamics*.

⁵Except for specific cases where the DCC can be absorbed in the chemical potential (see previous section)

⁶Notice that choosing the DCC according to the material removes the *ab-initio*-character of the DFT+DMFT method.

⁷Not only in absolute values, but also with respect to the conduction-electron bandwidth.

	LaFeAsO		BaFe ₂ As ₂	
	μ_{DC}^{AMF}	μ_{DC}^{FLL}	μ_{DC}^{AMF}	μ_{DC}^{FLL}
$3z^2 - r^2$	9.3900	9.5295	10.6920	10.8510
xz	8.8440	8.9790	9.7620	9.9117
yz	8.8440	8.9790	9.7620	9.9117
$x^2 - y^2$	8.0880	8.2157	9.2700	9.4147
xy	9.5340	9.6732	10.4520	10.6073
	LiFeAs		KFe ₂ As ₂	
	μ_{DC}^{AMF}	μ_{DC}^{FLL}	μ_{DC}^{AMF}	μ_{DC}^{FLL}
$3z^2 - r^2$	12.3840	12.5740	9.8010	9.8805
xz	11.5080	11.6900	8.9485	9.0234
yz	11.5080	11.6900	8.9485	9.0234
$x^2 - y^2$	11.3820	11.5623	8.4975	8.5699
xy	12.0660	12.2523	9.5810	9.6586
	FeTe			
	μ_{DC}^{AMF}	μ_{DC}^{FLL}		
$3z^2 - r^2$	13.1400	13.3397		
xz	11.7720	11.9597		
yz	11.7720	11.9597		
$x^2 - y^2$	13.0380	13.2400		
xy	13.3680	13.5735		

Table 3.6: Orbital dependent double counting correction (DCC) for the d -model. The difference between $BaFe_2As_2$ and KFe_2As_2 is exclusively due to the different filling n_0 .

3.4 Temperature

To accurately compare the influence of the degree of correlation upon the formation and screening of a local magnetic moment with respect to the materials, we have chosen the same temperature for all calculations in this thesis. We decided to use $\beta = 50 \text{ eV}^{-1}$, for which all materials are still in the paramagnetic phase. This corresponds to 232.1 K.

Chapter 4

Results: DMFT

In this chapter we present the DMFT-results for all the families of the Fe-based superconductors considered. In particular, we will proceed by considering in separate subsections all compounds representative of the different families one by one, where their order reflects approximately their "degree of correlation". We start with the least correlated one LaFeAsO, then proceed with moderately correlated ones BaFe₂As₂ and LiFeAs and terminate with the strongly correlated ones: KFe₂As₂ and FeTe. In each material-section we first show the one-particle properties (self-energy and Green's function in Matsubara-frequencies) for all considered interaction-Hamiltonians and models, before focusing on the two-particle-properties (spin-spin-susceptibilities).

The comparison between different families of the Fe-based superconductors will be examined thoroughly in the subsequent chapters.

4.1 LaFeAsO

4.1.1 One-particle-properties in the d -model

In figure 4.1 we report the self-energy as well as the Green's function for a density-density type interaction in the d -model only. Figure 4.2 show the same for a Kanamori-type interaction. For which the full $SU(2)$ spin-symmetry of the Hubbard-interaction was restored. In both cases we used the averaged values of the Coulomb-overlap integrals (\bar{U} , \bar{J} and \bar{V}). This assumption was lifted for computing the data of Fig. 4.3 where we used the full-orbital dependence regarding the interaction terms. In this case DFT+DMFT calculation has been performed with the full Coulomb-interaction¹, hence we refer to this approach as "full U ".

¹at the level of cRPA

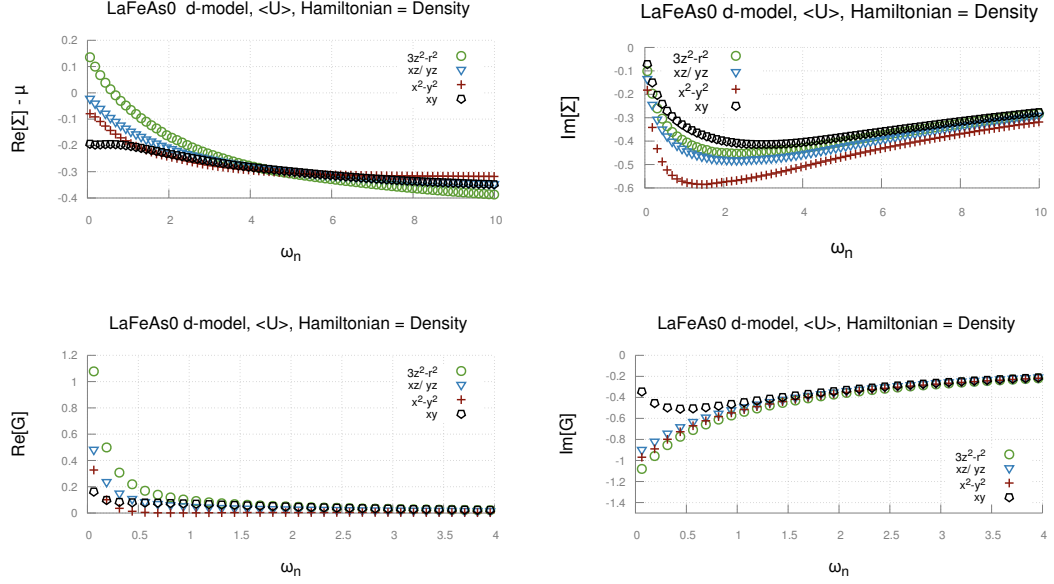


Figure 4.1: DFT+DMFT results for *LaFeAsO* in the *d*-only-model with orbital averaged Coulomb interactions used for a density-density-type interaction.

Comparing figure 4.1 with 4.2 we find the inclusion of the full $SU(2)$ symmetry not to change the physics drastically. From the $\lim_{i\omega_n \rightarrow 0} \text{Im}\Sigma$ and from $\lim_{i\omega_n \rightarrow 0} \text{Im}G$ we find the Kanamori-case to be more metallic. For both interaction types the $3z^2 - r^2$ orbital was shifted up whereas the $x^2 - y^2$ and xy -orbitals were shifted down slightly as can be inferred from $\text{Re}\Sigma$ (upper left figures). A similar trend for the shift of the orbitals is found also in the full-U calculations.

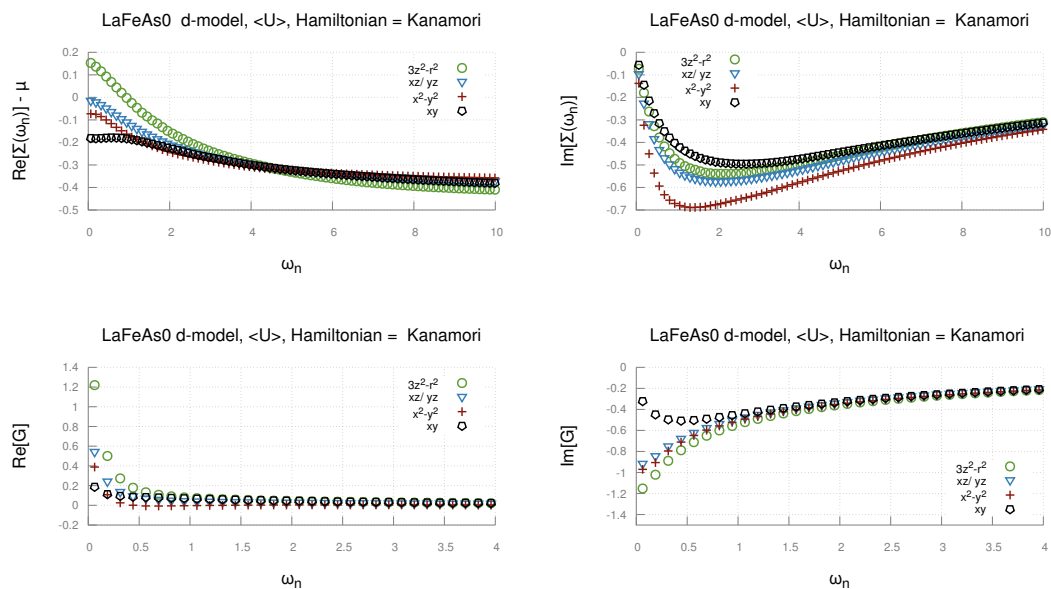


Figure 4.2: DFT+DMFT results of the single-particle properties of *LaFeAsO* in the *d*-only-model with orbital averaged Coulomb interactions used for a Kanamori-type interaction.

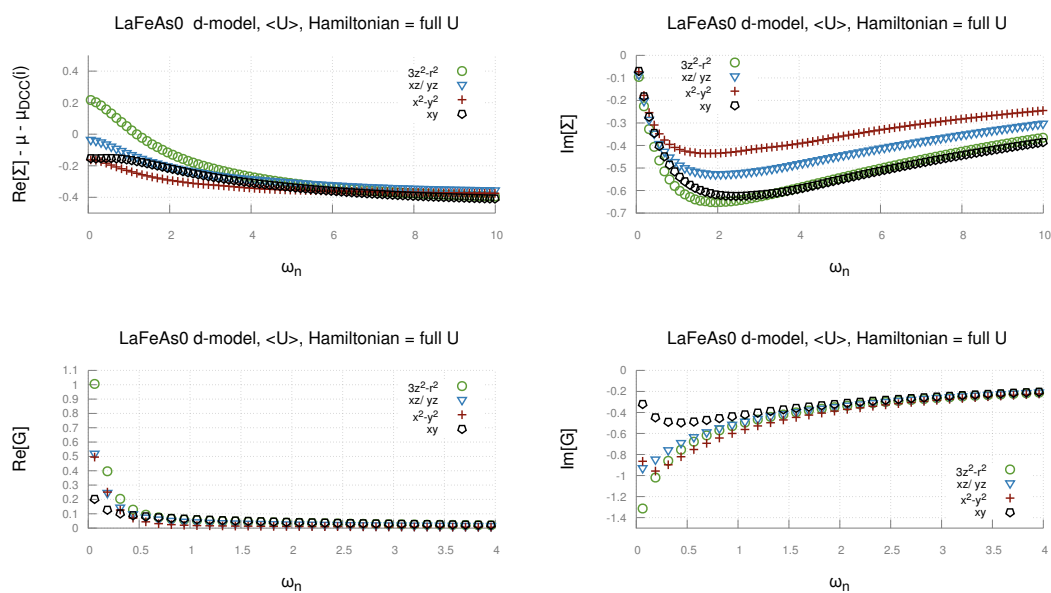


Figure 4.3: DFT+DMFT results of the single-particle properties of *LaFeAsO* in the *d*-only-model with "full U" interaction.

Comparing the two cases with orbital-averaged interaction-terms with the orbital-resolved U-term case we find that the roles of the orbitals have changed significantly. This is especially true for the e_g -orbitals. The $3z^2 - r^2$ -orbital gets a larger contribution at the Fermi-surface and an overall more metallic character. The $x^2 - y^2$ -orbitals gets less weight and is significantly less metallic. The t_{2g} -orbitals are less affected by non-averaged interaction terms.

The general trend is that all orbitals show a metallic character and large quasi-particle excitation life-times.

4.1.2 One-particle-properties in the dpp -model

Fig. 4.4 and Fig. 4.5 show the self-energies and Green's functions in Matsubara frequencies for density-density- as well as for Kanamori interaction. In both cases the U, V and J values were averaged over all orbitals.

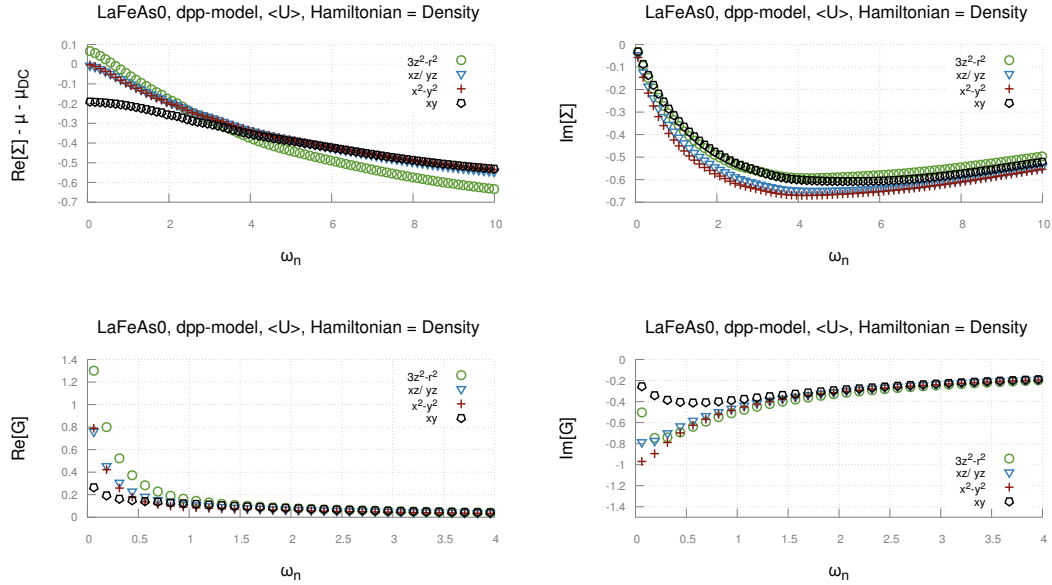


Figure 4.4: DFT+DMFT results of the single-particle properties of $LaFeAsO$, computed for the dpp -model with orbital-averaged Coulomb interaction in density-density-type interaction. We used the FLL for the DCC.

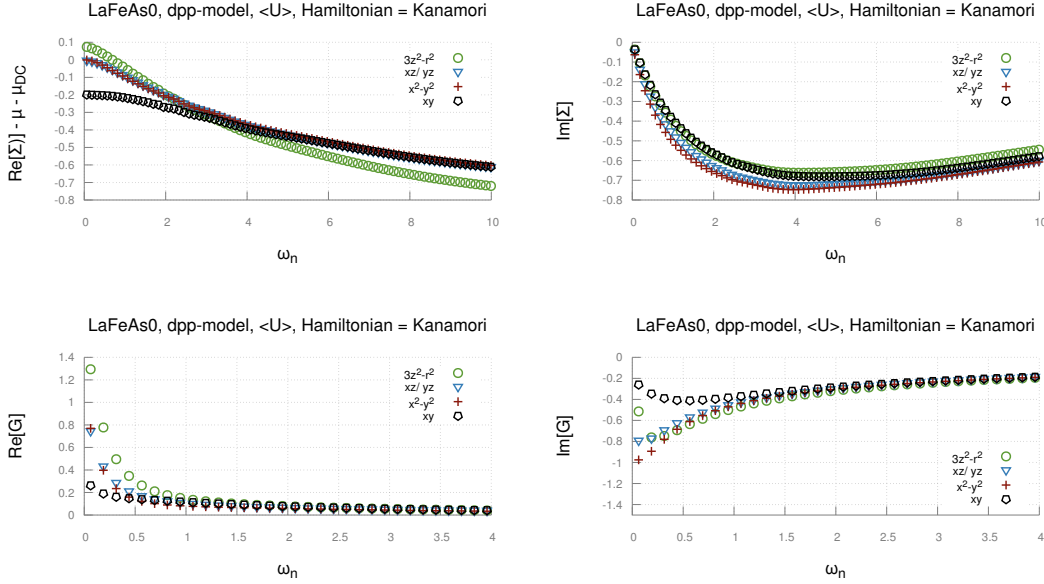


Figure 4.5: DFT+DMFT results of the single-particle properties of $LaFeAsO$, computed for the dpp -model with orbital-averaged Coulomb interaction in Kanamori-type interaction. We used the FLL for the DCC.

The two sets of figures show an overall similar behavior. From the imaginary part of the self-energy, one can just deduce a slightly larger quasi-particle excitation lifetime for the density-density case. The imaginary part of the Green's function is almost exactly on top, regarding these two interaction types. From the real part of the self-energy we find the trend that $\text{Re}\Sigma_i^{\text{Kanamori}} > \text{Re}\Sigma_i^{\text{Density}}$. This means that for a Kanamori-interaction, the orbitals are slightly more shifted to higher energies.

The comparison to the d -model full- U case shows a very different picture. This is mostly due to the different filling. Which is exactly 6.00 for the d -only-model, but ranges between 7.29 (Kan.) to 7.32 (dens) in the dpp -model. This can (and does on our cases) lead to a smaller spectral weight at $\omega = 0$ for the dpp -model than in the d -model. A smaller spectral weight at the Fermi energy means that fewer quasi-particles can be excited into a conducting state at zero-energy cost. One can see this for example by comparing the first few Matsubara frequencies of the bottom right figures of Fig. 4.3 to Fig. 4.5. This effect is especially significant for the $3z^2 - r^2$ -orbital (green), which has the largest spectral weight for the full- U case, whereas for the averaged U dpp -model it has a much smaller spectral weight and hardly any distinctive features regarding the other orbitals. This is rather due to the choice of model (d - vs dpp -) than due to the orbital-averaged interaction values or H^{int} choice, as can be seen by a comparison to Fig. 4.1 and Fig. 4.2.

4.1.3 Model comparison of the two-particle-properties: Spin-spin susceptibilities

In this subsection we compare the spin-spin-susceptibility χ computed with different models and interaction terms for *LaFeAsO*. We will focus our attention in particular to the difference between the χ^{tot} and χ^{diag} , which is entirely due to vertex corrections. First the QMC-data are shown (in imaginary time in Fig. 4.6 and in Matsubara frequencies in Fig. 4.7). Second, the analytically continued data (in real frequencies) have been computed. From these we can extract the different time-scales of the spin-dynamics of the system. Third, we show the Fourier transformed susceptibilities in real frequencies. From the fluctuation-dissipation theorem we also extract the symmetric anti-commutator-correlation function $F(t)$, which is better suited to study the quantum-mechanical spin-screening effects.

Susceptibilities in imaginary time/ frequency

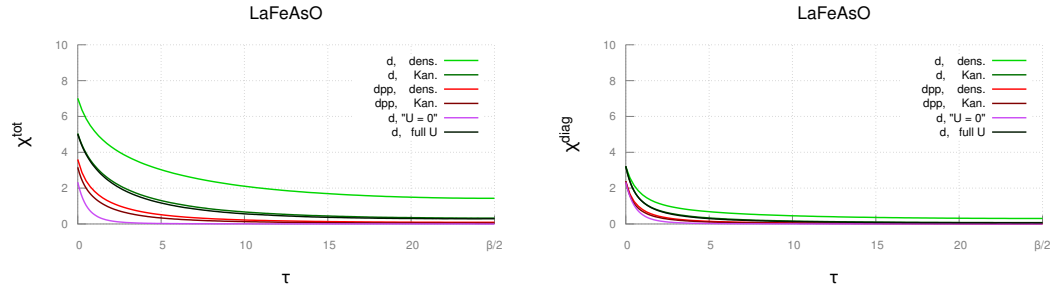


Figure 4.6: *LaFeAsO*: Spin-spin-susceptibility in imaginary time computed for the different models and interaction-types.

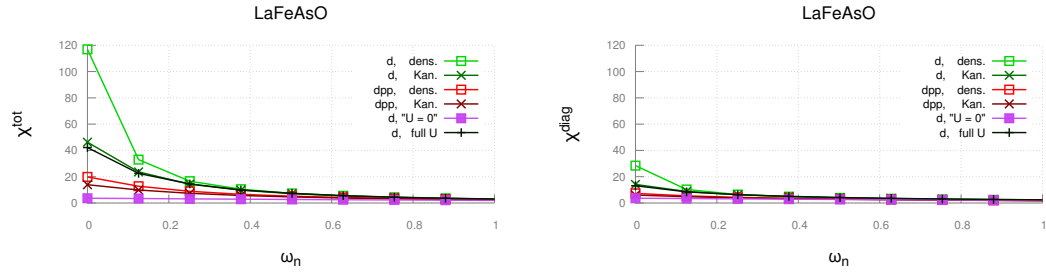


Figure 4.7: *LaFeAsO*: Spin-spin-susceptibility in Matsubara frequencies computed for the different models and interaction-types.

An interesting feature in Fig. 4.6 is that for the d -model the Kanamori-interaction with averaged U -terms gives almost exactly the same results as the d -model with full U interaction. This is rather remarkable since it could not be expected on the basis of the one-particle properties above. One may interpret it as a posteriori justification of the averaged procedure, if a

quantity is computed which sums over all orbital-indices. The role of each individual orbital has changed.

Comparing the left and right sub-figures of Fig. 4.6, we see that, especially for the density-density interaction, in the d -model a significant contribution comes from vertex corrections. (With the obvious exception of the $U = 0$ case, where $\chi^{\text{tot}} = \chi^{\text{diag}}$.) Furthermore we find the dpp -cases to be closer to the $U = 0$ case. This can be understood from the filling. In the dpp -cases the d -orbitals are further away from half-filling and thus effectively less interacting.

Susceptibilities in real frequencies

In Fig. 4.8 and in Fig. 4.10 analytically continued spin-spin-susceptibilities via two different methods are shown. To obtain Fig. 4.8 we use the Maximum-Entropy-method (more specifically [40] with an additional selection criterion discussed in section 2.4.3), which is well established. Whereas for Fig. 4.10, we have used a newer method named Sparse-Modeling. (More specifically we used a program supplied by the authors of the method[32].)

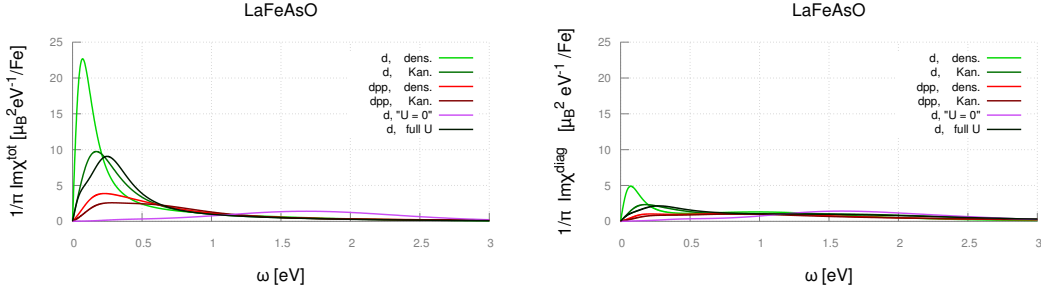


Figure 4.8: LaFeAsO: MaxEnt Spin-spin-susceptibility in real frequencies computed for the different models and interaction-types.

The non-interacting case (purple) shows a very featureless broad absorption spectrum extended roughly on the whole non-interacting bandwidth. As expected χ^{tot} equals χ^{diag} , since there are no vertex corrections for $U = J = V = 0$. In all the other models and Hamiltonians low energy peak appears, instead. The position of the peak depends on the choice of the model as well as the Hamiltonian. It ranges from 72 meV (d -model dens. dens. int.) to 284 meV (dpp -model Kan. int.).

The most reliable of the d -model is probably the *full* - U case, since we used a general orbital-dependent U -matrix as H^{int} . It has its peak-maximum of 0.249 eV. For this case we fitted the following model spectral function to the data.

$$\text{Im}\chi^{\text{tot}}(\omega) = \frac{2a\gamma\omega}{4\gamma^2\omega^2 + (\omega^2 - \omega_0^2)^2}$$

The fit was performed via minimizing the quadratic difference between the model and the data at the data-points. It is important to remark that the data-points are more dense at smaller energies (due to a Lorentzian energy mesh). This can be justified by the fact that the singular values of the kernel (connecting $\chi(\tau)$ with $\chi(\omega)$) decay fast with respect to the energy. Thus

$\chi(\omega)$ is better "supported" by the data at smaller frequencies than at higher frequencies. One should therefore "weigh" $\chi(\omega)$ at smaller frequencies more than at higher frequencies. This allows us to extract model parameters as

	Estimate	Standard Error	t-Statistic	P-Value
a	1.4273	0.0105749	134.971	$2.012 \cdot 10^{-746}$
ω_0	0.342307	0.00104806	326.609	$3.080 \cdot 10^{-1210}$
γ	0.282543	0.00212606	132.895	$1.4183 \cdot 10^{-738}$

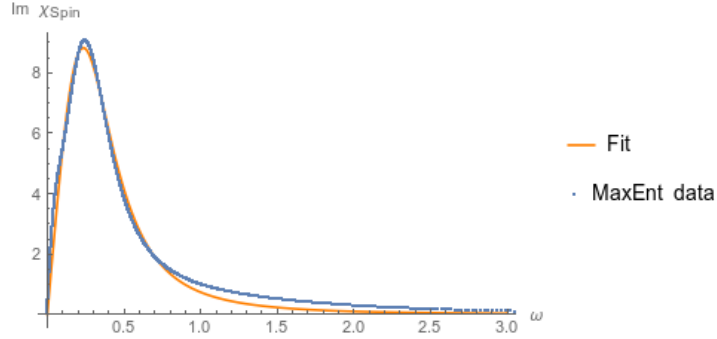


Figure 4.9: LaFeAsO: Comparison between the fitted model and the MaxEnt data.

Since the damping-parameter γ is smaller than the undamped-frequency ω_0 we are in the underdamped regime. The Fourier-transform of the model reads (in natural units) as

$$\chi^{\text{tot}}(t) = \theta(t) 7.38596 e^{-0.282543t} \sin(0.193245t).$$

However since the γ and ω_0 are not that different from each other a better life-time estimate can be extracted from the Fourier-transformed data (in real time).

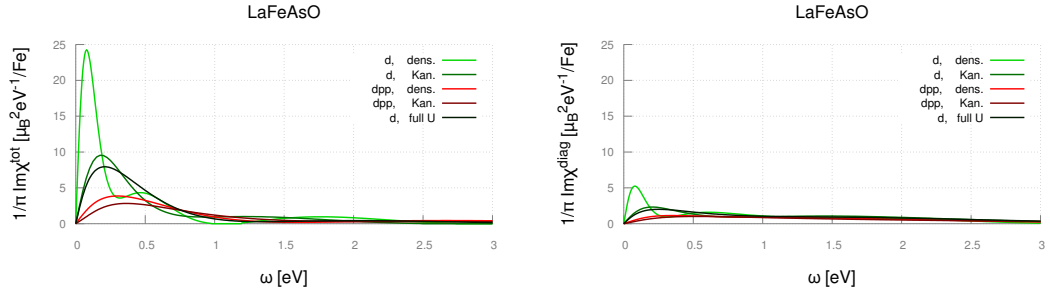


Figure 4.10: LaFeAsO: SpM Spin-spin-susceptibility in real frequencies computed for the different models and interaction-types. (For LaFeAsO SpM and MaxEnt agree reasonably well with one another.)

We find the two analytical continuation procedures to agree rather well with one another. As can be seen by comparing Fig. 4.8 with 4.10. It should, however, be remarked that LaFeAsO is the least correlated of the materials under consideration in this thesis.

Susceptibilities in real time

The Fourier-transform can be easily carried out and from the fluctuation-dissipation-theorem one can also calculate the anti-commutator-correlator $F(t)$ without any difficulty. The result with restored SI-units are shown in Fig. 4.11 and Fig. 4.12. We only show them for $t > 0$ since $\chi(t)$ is zero for $t < 0$ and $F(t)$ is symmetric with respect to time.

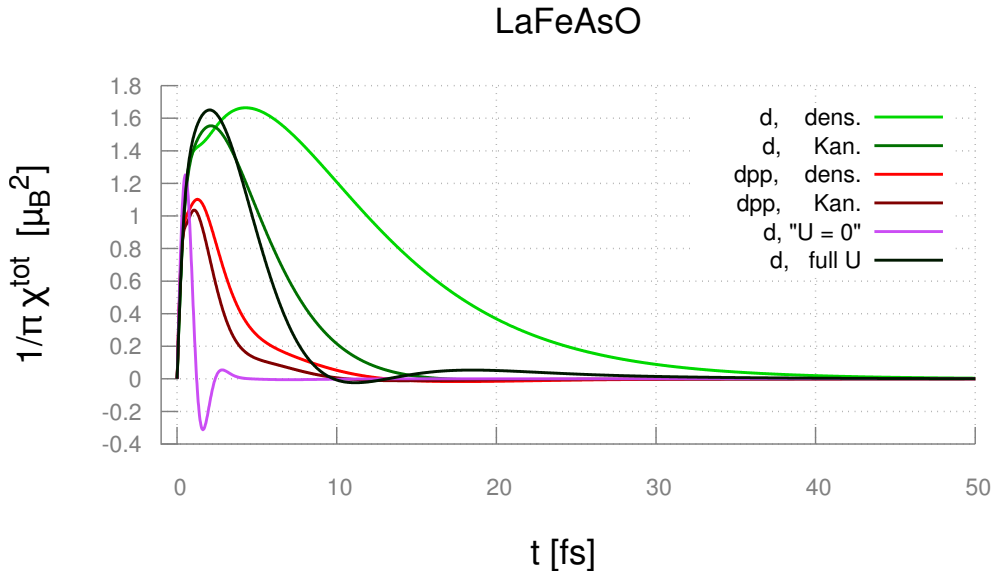


Figure 4.11: LaFeAsO: Spin-spin-susceptibility in real time computed for the different models and interaction-types.

We find $\chi(t)$ to decay on an approximate time-scale of 2 – 20fs depending upon the choice of model and Hamiltonian. $F(t)$ decays more rapidly on a time-scale of approximately 0.5 – 8fs. Comparing this with the model-time-scales (for full U MaxEnt)

$$\begin{aligned} t_\gamma &= \frac{\hbar}{\gamma} = 2.33 \text{ fs} \\ t_\omega &= \frac{\hbar}{\sqrt{\omega_0^2 - \gamma^2}} = 3.41 \text{ fs}, \end{aligned} \quad (4.1)$$

we find a damping time-scale of 2.33fs and a resonating time-scale of 3.41fs. Thus the damping is the more relevant effect for LaFeAsO (in full U in the d -model).

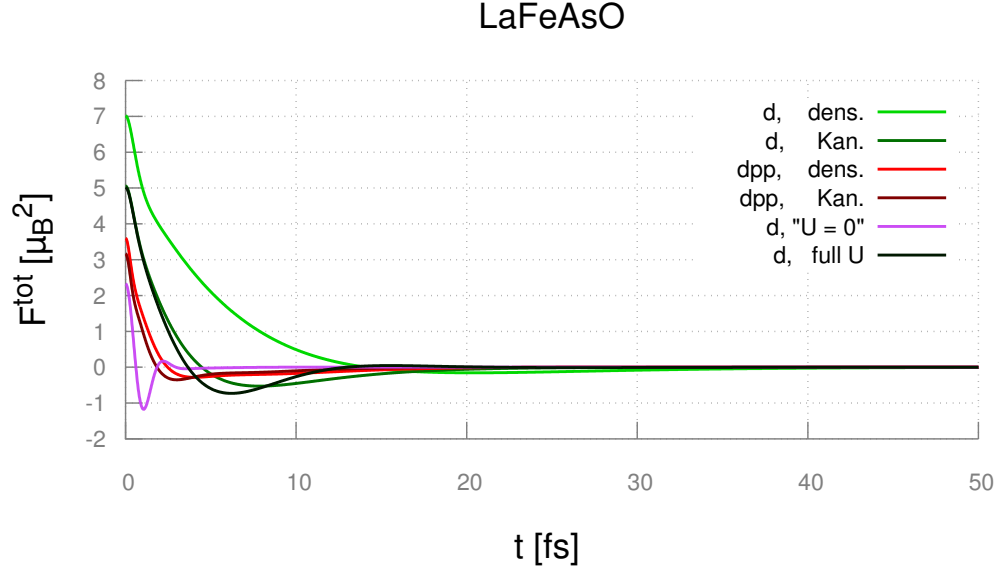


Figure 4.12: LaFeAsO: Spin-spin-anti-commutator correlation function in real time computed for the different models and interaction-types.

Cutoff dependence of the full integral

$$m_{\text{loc},t=0}^2 = \frac{3}{\pi} \lim_{\Omega \rightarrow \infty} \frac{\int_{-\Omega}^{\Omega} \int_{\text{BZ}} \text{Im}\chi(\vec{q}, \omega) b(\omega) d\vec{q} d\omega}{\int_{\text{BZ}} d\vec{q}} = \frac{3}{\pi} \lim_{\Omega \rightarrow \infty} \int_{-\Omega}^{\Omega} \text{Im}\chi(\text{loc}, \omega) b(\omega) d\omega \quad (4.2)$$

In Fig. 4.13 the energy cut-off dependence of the full (square) local magnetic moment is shown. The vertical dotted line marks a experimentally typical energy scale (for INS-measurements) of 100meV. Our results show that only 5% (for *dpp*) to 20% (for *d* dens.dens int.) of the full local magnetic-moment would show for such a cut-off value. For the full *U* case (very similar to the *d*-model Kan. int. case) one would make an 90% error.

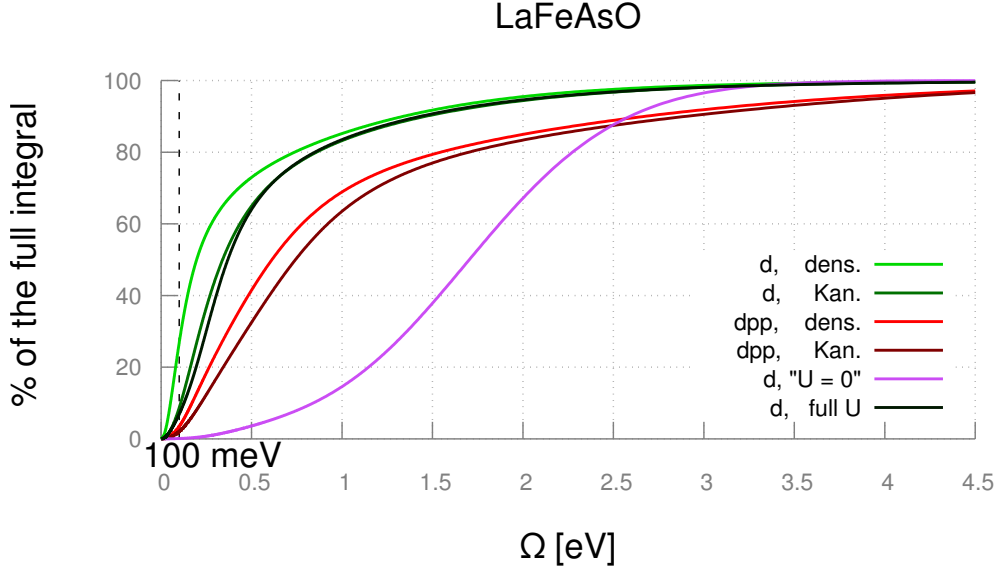


Figure 4.13: LaFeAsO: Cutoff dependency (finite Ω) of the squared local magnetic moment estimate $\langle m^2 \rangle$ (full integral in (Eq. 4.2)) computed for the different models and interaction-types.

4.1.4 Occupations and local magnetic momentum

In Tab. 4.1 we report the average occupations and double-occupations with the same spin while in Fig. 4.2 the average double-occupations with different spin are shown. Since we are in the paramagnetic phase the occupations can be deduced via symmetry ($\langle n_{i\uparrow} \rangle = \langle n_{i\downarrow} \rangle$). By comparing the two Tables once can also compute $C_{n_{i\sigma}n_{j\sigma'}} \equiv \langle n_{i\sigma}n_{j\sigma'} \rangle - \langle n_{i\sigma} \rangle \langle n_{j\sigma'} \rangle$ which measures the "degree of correlation".

We find LaFeAsO not to be particularly correlated. For example, by analyzing the results for orbital 1 (in full U), which has the largest U value, we get

$$C_{n_{1\uparrow}n_{1\downarrow}} = \langle n_{1\uparrow}n_{1\downarrow} \rangle - \langle n_{1\uparrow} \rangle \langle n_{1\downarrow} \rangle = 0.34 - 0.65^2 = 0.34 - 0.4225 = -0.0825.$$

This orbital is, however not the most correlated one (with respect to the same orbital-index) in spite of having the the largest U -value. For example $C_{n_{2\uparrow}n_{2\downarrow}} = -0.0881$ which shows that the (orbital-dependent) U -value alone is not a good estimate for the degree of correlation.

The orbital-dependent role of Hund's exchange, on the other hand, can be estimated by comparing $h_{ij} \equiv \langle n_{i\uparrow}n_{j\uparrow} \rangle - \langle n_{i\uparrow}n_{j\downarrow} \rangle$. Applying this to our Tables (again for the full U case) we get $h_{14} = h_{24} = h_{34} = 0.05$, whereas all the other $h_{ij} = 0.04$. Thus we conclude that the $x^2 - y^2$ orbital has the largest Hund's coupling effect, though it is not very different from the other orbitals.

Comparing the occupation numbers with respect to the different models and Hamiltonians (considering the columns) we observe only minor changes with respect to the interaction Hamiltonians, but qualitatively different results with respect to the different Wannier-projections (d vs dpp). In fact, this is ascribed to the considerably different filling of the d -manifold: In the

d -model the filling of the d -orbital manifold was fixed to 6 electrons on 10 available places, for the dpp -model this represents a free parameter. In the later case we have assumed that the number of electrons of the Wannier basis-set considered the d -manifold together with the two p -manifolds is 18. The reasons for arriving at these numbers were laid out in the previous chapter. It should therefore not be assumed that the dpp -results are automatically more valid than the d -ones[33].

At the same time, from the disagreement between the d - and the dpp -model, one can not answer the question which one is, more or less, correct.

Eventually, the squared local magnetic moment (total as well as diagonal contribution) is shown on the table. ($\chi^{\text{tot}}(\tau = 0)$ and $\chi^{\text{diag}}(\tau = 0)$). A more detailed discussion of this particular result will be given in the next chapter.

	d-model			dpp-model with FLL DCC	
	H_U^D	H_U^K	H_{FLL}^{fullU}	H_U^D	H_U^K
$\langle \mathbf{n}_{1\uparrow} \rangle$	0.69	0.68	0.65	0.81	0.81
$\langle n_{1\uparrow} n_{2\uparrow} \rangle$	0.44	0.41	0.39	0.58	0.57
$\langle n_{1\uparrow} n_{3\uparrow} \rangle$	0.44	0.41	0.39	0.58	0.57
$\langle n_{1\uparrow} n_{4\uparrow} \rangle$	0.41	0.38	0.39	0.58	0.57
$\langle n_{1\uparrow} n_{5\uparrow} \rangle$	0.44	0.42	0.41	0.57	0.57
$\langle \mathbf{n}_{2\uparrow} \rangle$	0.59	0.59	0.59	0.72	0.71
$\langle n_{2\uparrow} n_{3\uparrow} \rangle$	0.39	0.36	0.36	0.52	0.51
$\langle n_{2\uparrow} n_{4\uparrow} \rangle$	0.37	0.33	0.35	0.52	0.51
$\langle n_{2\uparrow} n_{5\uparrow} \rangle$	0.39	0.37	0.37	0.51	0.50
$\langle \mathbf{n}_{3\uparrow} \rangle$	0.59	0.59	0.59	0.72	0.71
$\langle n_{3\uparrow} n_{4\uparrow} \rangle$	0.37	0.33	0.35	0.52	0.51
$\langle n_{3\uparrow} n_{5\uparrow} \rangle$	0.39	0.37	0.37	0.51	0.50
$\langle \mathbf{n}_{4\uparrow} \rangle$	0.53	0.53	0.56	0.71	0.71
$\langle n_{4\uparrow} n_{5\uparrow} \rangle$	0.36	0.34	0.35	0.51	0.50
$\langle \mathbf{n}_{5\uparrow} \rangle$	0.61	0.61	0.61	0.71	0.71
$\sum_{i,\sigma} \langle n_{i,\sigma} \rangle$	6.00	6.00	6.00	7.32	7.29
$\chi^{\text{tot}}(\tau = 0)$	7.01	5.06	5.01	3.60	3.17
$\chi^{\text{diag}}(\tau = 0)$	3.19	3.22	3.22	2.37	2.39

Table 4.1: Comparison of orbital occupations of the *same* spin dependent on the interaction class as well as the model for LaFeAsO.

	d-model			dpp-model with FLL DCC	
	$H_{\bar{U}}^D$	$H_{\bar{U}}^K$	H_{FLL}^{fullU}	$H_{\bar{U}}^D$	$H_{\bar{U}}^K$
$\langle \mathbf{n}_{1\uparrow} \mathbf{n}_{1\downarrow} \rangle$	0.41	0.40	0.34	0.63	0.63
$\langle n_{1\uparrow} n_{2\downarrow} \rangle$	0.35	0.37	0.35	0.56	0.56
$\langle n_{1\uparrow} n_{3\downarrow} \rangle$	0.35	0.37	0.35	0.56	0.56
$\langle n_{1\uparrow} n_{4\downarrow} \rangle$	0.30	0.33	0.34	0.55	0.55
$\langle n_{1\uparrow} n_{5\downarrow} \rangle$	0.38	0.39	0.37	0.55	0.55
$\langle \mathbf{n}_{2\uparrow} \mathbf{n}_{2\downarrow} \rangle$	0.26	0.26	0.26	0.47	0.46
$\langle n_{2\uparrow} n_{3\downarrow} \rangle$	0.29	0.31	0.32	0.49	0.49
$\langle n_{2\uparrow} n_{4\downarrow} \rangle$	0.24	0.28	0.30	0.48	0.48
$\langle n_{2\uparrow} n_{5\downarrow} \rangle$	0.31	0.33	0.33	0.48	0.48
$\langle \mathbf{n}_{3\uparrow} \mathbf{n}_{3\downarrow} \rangle$	0.26	0.26	0.26	0.47	0.46
$\langle n_{3\uparrow} n_{4\downarrow} \rangle$	0.24	0.27	0.30	0.48	0.48
$\langle n_{3\uparrow} n_{5\downarrow} \rangle$	0.31	0.33	0.33	0.48	0.48
$\langle \mathbf{n}_{4\uparrow} \mathbf{n}_{4\downarrow} \rangle$	0.16	0.16	0.23	0.45	0.44
$\langle n_{4\uparrow} n_{5\downarrow} \rangle$	0.27	0.29	0.31	0.47	0.48
$\langle \mathbf{n}_{5\uparrow} \mathbf{n}_{5\downarrow} \rangle$	0.31	0.31	0.30	0.46	0.46

Table 4.2: Comparison of orbital occupations with *different* spin dependent on the interaction class as well as the model for LaFeAsO.

4.2 $Ba_2Fe_2As_2$

4.2.1 One-particle-properties in the d -model

In Fig. 4.14 we show the self-energy as well as the Green's function for a density-density type interaction in the d -only model. Fig-4.15 show the same for a Kanamori-type interaction. In both cases, we have used the averaged values of the Coulomb-overlap integrals (\bar{U} , \bar{J} and \bar{V}). The latter assumption was then removed, when performing the *full* U calculation (shown in Fig. 4.16).

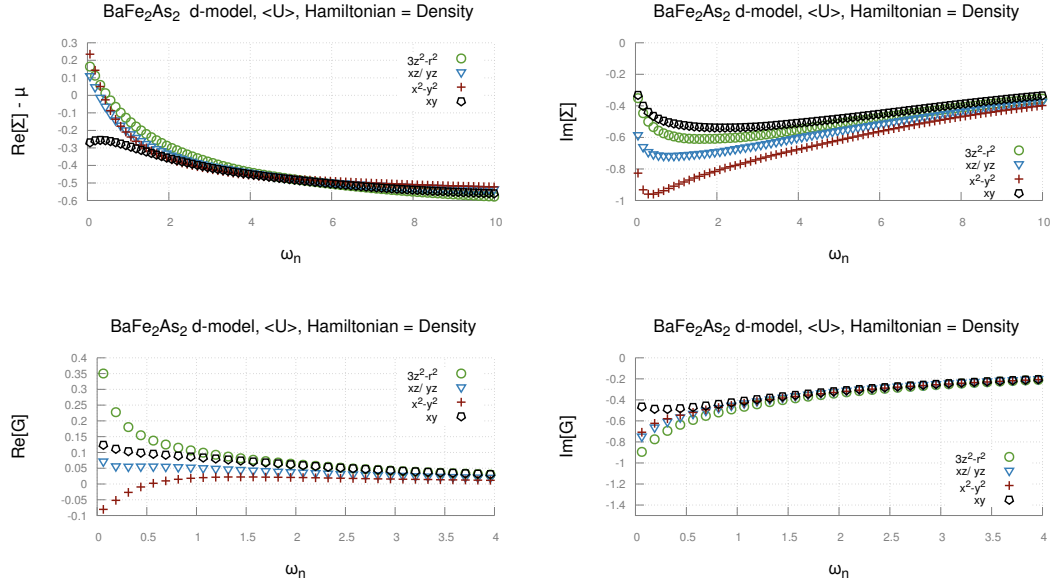


Figure 4.14: DFT+DMFT results of the single-particle properties of $BaFe_2As_2$ in the d -only model with orbital averaged Coulomb interactions used for a density-density-type interaction.

From Fig. 4.14 we find that all orbitals have a metallic character, but with finite quasi-particle excitations lifetimes. Thus the interaction strength is not strong enough to drive the material towards the Mott-insulating phase. From $\text{Re}\Sigma$ (upper left figure) we find that the xy -orbital is shifted considerably lower energies (by more than 0.25eV) while the other are all shifted to higher energies. From the imaginary part of the Green's function (lower left subfigure in Fig. 4.14), we see that the xy -orbital has considerably less spectral weight at the Fermi-level than the other orbitals.

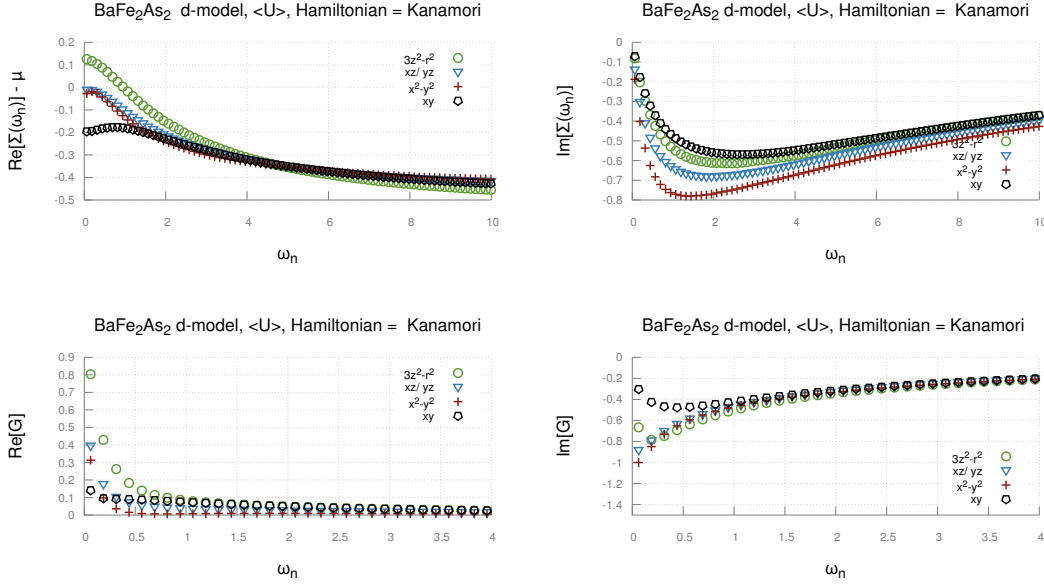


Figure 4.15: DFT+DMFT results of the single-particle properties of $BaFe_2As_2$ in the d -only-model with orbital averaged Coulomb interactions used for a Kanamori-type interaction.

The results for a Kanamori-Hamiltonian show overall similar results as for density-density interaction. However, also some fine differences can be noted. From $\text{Re}\Sigma$, we see that the shift of the orbitals is less severe in magnitude for $3z^2 - r^2$ - and xy -orbital, and the xz/yz as well as the $x^2 - y^2$ -orbital are hardly shifted at all.

As for the imaginary part of the Green's function, this can not as easily interpreted as for $LaFeAsO$: We find more spectral weight at ϵ_F for some orbitals (xz/yz and $x^2 - y^2$), but significantly less for others ($3z^2 - r^2$ - and xy). In this respect, more insight can be gained by analyzing the data-sets for $\text{Im}\Sigma$ (upper left subfigures): On finds that $\lim_{i\omega_n \rightarrow 0} |\text{Im}\Sigma|$ is smaller for all orbitals. Thus, quasi-particle excitations in all orbitals have a longer lifetime for a Kanamori-Hamiltonian than for a density-density-Hamiltonian. One can therefore conclude that the Kanamori-interaction (instead of the dens.-dens.-int.) lead to a more metallic behavior in the paramagnetic phase.

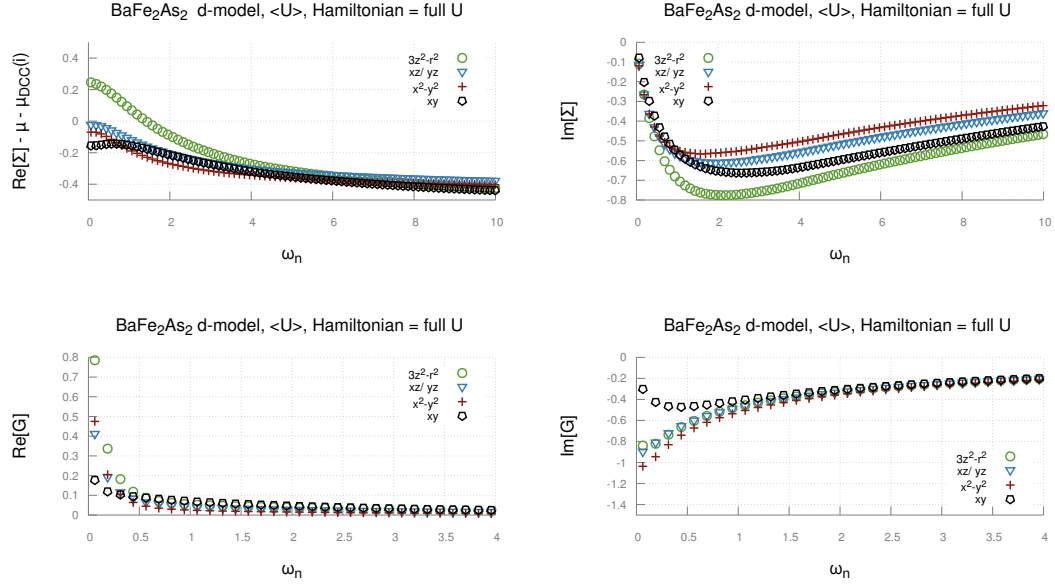


Figure 4.16: DFT+DMFT results of the single-particle properties of $BaFe_2As_2$ in the d -only-model with "full U" interaction.

In Fig. 4.16 an overall comparison of that data of full U calculations have been shown. We find that while all the orbitals overall still show a metallic character, the role of the individual orbitals has changed. This is specially significant for the $3z^2 - r^2$ -orbital which has significantly less spectral weight at the Fermi-level compared to the previous cases. The orbital-dependence of the excitation live-times has changed, slightly, depending on the orbital-index, but overall similar lifetimes as for Kanamori were extracted. The orbital dependent energy-shift has a stronger magnitude for full U than for Kanamori (see $\text{Re}\Sigma$).

4.2.2 One-particle-properties in the dp -model

Double counting correction: When performing a dp -calculation in DMFT, an important role is always played by the double counting corrections (DCC), whose role will be explicitly analyzed in this subsection. Although we have good reasons to believe that FLL DCC is a better choice than AMF for all compounds under consideration ², we want to check for an intermediately correlated material (among the class of Fe-SC). Since $BaFe_2As_2$ is more correlated than $LaFeAsO$, but less correlated than $FeTe$, we selected this material as a testbed to check how much of a difference the DCC choice makes.

In Fig 4.17 we show the one-particle-properties of $BaFe_2As_2$ for a dp -model. We computed both commonly used DCC for a density-density-interaction type. We find that the shift of the orbitals (corrected by the chemical potentials as well as the μ_{DC} -values) is almost exactly the same for both DCC choices (see $\text{Re}\Sigma$). From $\text{Im}\Sigma$ (top left) we find a general trend that $|\text{Im}\Sigma^{\text{AFM}}(i\omega_n)| < |\text{Im}\Sigma^{\text{FLL}}(i\omega_n)|$. Hence the quasi-particle lifetimes are smaller for the FLL. This shift in $\text{Im}\Sigma$ is, however, not big enough to affect significantly the spectral weight at the Fermi-level, as $\text{Im}G$ appears quite unaffected.

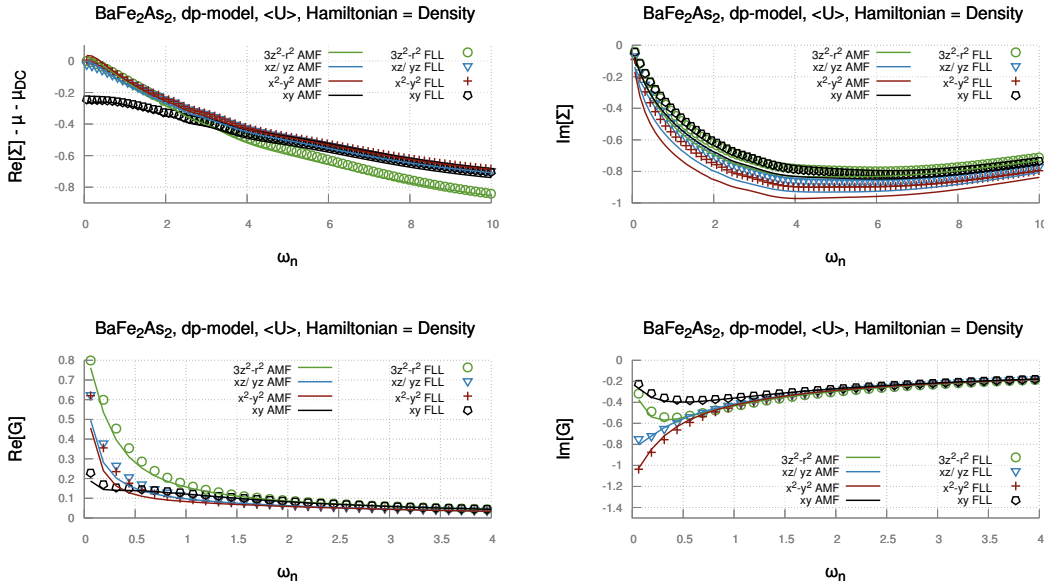


Figure 4.17: DFT+DMFT results of the single-particle properties of $BaFe_2As_2$, computed for the dp -model with orbital-averaged Coulomb interaction in density-density-type interaction. We used both common DCC: FLL (points) and AMF (lines). For the solid lines, clearly, only the values at the Matsubara-frequencies have physical meaning.

²see previous chapter for a detailed discussion

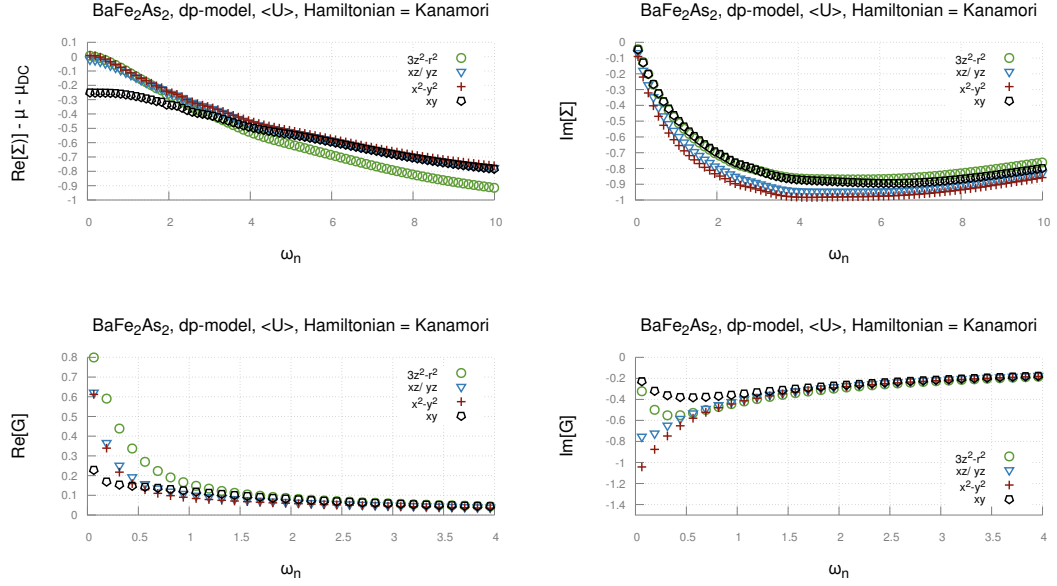


Figure 4.18: DFT+DMFT results of the single-particle properties of $BaFe_2As_2$, computed for the dp -model with orbital-averaged Coulomb interaction in Kanamori-type interaction. We used FLL for the DCC.

In Fig 4.18 we show the one-particle-properties of a Kanamori-type-interaction (for $BaFe_2As_2$ in the dp -model). The Green's function as well as the self-energy are very similar as in Fig. 4.17 (dens. int. with same model). By comparing to the d -only model we find, a very small trend of $\lim_{i\omega_n \rightarrow 0} \text{Im} |\Sigma^{\text{d model}}(i\omega_n)| > \lim_{i\omega_n \rightarrow 0} |\text{Im} \Sigma^{\text{dp model}}(i\omega_n)|$ and moreover $\lim_{i\omega_n \rightarrow 0} \left| \frac{\partial}{\partial i\omega_n} \text{Im} \Sigma^{\text{d model}}(i\omega_n) \right| < \frac{\partial}{\partial i\omega_n} \lim_{i\omega_n \rightarrow 0} |\text{Im} \Sigma^{\text{dp model}}(i\omega_n)|$. Therefore the quasi-particle lifetimes are slightly shorter in the d -model and the Fermi-liquid weight-factor ($Z = (1 + |\frac{\partial \text{Im} \Sigma}{\partial i\omega}|)^{-1}$) is slightly smaller, which leads to an mass-enhancement. Overall $BaFe_2As_2$ shows metallic behavior for all models and interaction Hamiltonians. From the one-particle properties alone this Fe-SC parent compound could be understood as a Fermi-liquid. The two-particle properties are shown in the next subsection.

4.2.3 Model comparison of the two-particle-properties: Spin-spin susceptibilities

In this subsection, we compare the spin-spin-susceptibility χ computed with different models and interaction terms for $BaFe_2As_2$. We will focus our attention in particular to the difference between the χ^{tot} and χ^{diag} , which is entirely induced by the electronic interaction, and mainly by the to vertex corrections.

First, the QMC-data are shown (in imaginary time in Fig. 4.6 and in Matsubara frequencies in Fig. 4.7). Second, the analytically continued data (in real frequencies) have been computed. From these we could extract the different time-scales of the spin-dynamics of the system. Third, we show the Fourier transformed susceptibilities in real frequencies. From the fluctuation-dissipation theorem we also extract the symmetric anti-commutator-correlation function $F(t)$, which is better suited to study the quantum-mechanical spin-screening effects.

Susceptibilities in imaginary time/ frequency

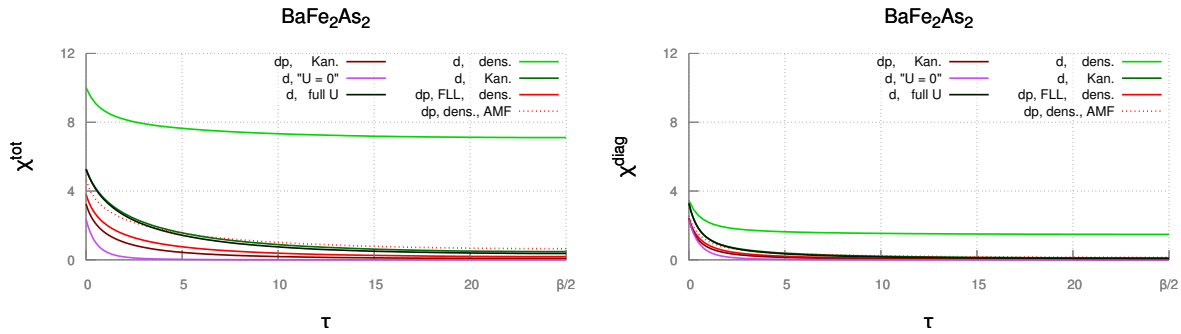


Figure 4.19: $BaFe_2As_2$: Comparison of the spin-spin-susceptibility in imaginary time computed for the different models and interaction-types.

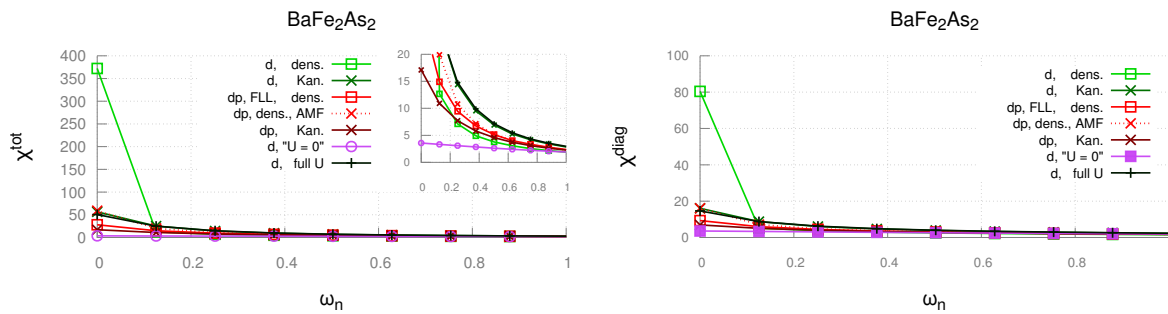


Figure 4.20: $BaFe_2As_2$: Comparison of spin-spin-susceptibility in Matsubara frequencies computed for the different models and interaction-types.

We find in Fig. 4.6 (again) that the d -model the Kanamori-interaction with averaged U -terms gives almost exactly the same spin-spin-correlation function as the d -model with full U interaction. This is remarkable since it could hardly be expected on the basis of the one-particle properties discussed before. One may interpret it as a "posteriori" justification of the averaging procedure, if a quantity is computed which sums over all orbital-indices. The role of each individual orbital has changed.

Comparing the left and right sub-figures of Fig. 4.6, we see that, especially for the density-density interaction, in the d -model a significant contribution comes from vertex corrections. (with the obvious exception of the $U = 0$ case, where $\chi^{\text{tot}} = \chi^{\text{diag}}$). Furthermore we find the dp -cases to be closer to the $U = 0$ case. This can be related to the significantly enhance filling of the d -orbitals. Similar to LaFeAsO the filling is roughly 7.2 for $BaFe_2As_2$ in the dpp -model (see Tab. 4.3). Regarding the comparison between FLL and AMF (dpp -model) we find a different magnitude of $\langle m^2 \rangle$ (see $\chi(\tau = 0)$) but similar screening behavior ($\chi^{\text{FLL}}(\tau)/\chi^{\text{FLL}}(0) \cong \chi^{\text{AMF}}(\tau)/\chi^{\text{AMF}}(0)$). For a more quantitative analysis the analytical continuation is needed.

Susceptibilities in real frequencies

In Fig. 4.21 and in Fig. 4.23 analytically continued spin-spin-susceptibilities via two different methods are shown. To obtain Fig. 4.21 we use the Maximum-Entropy-method (more specifically [40] with an additional selection criterion discussed in section 2.4.3). While for Fig. 4.23, we have used a newer method named Sparse-Modeling (more specifically we used a program supplied by the authors of the method[32].)

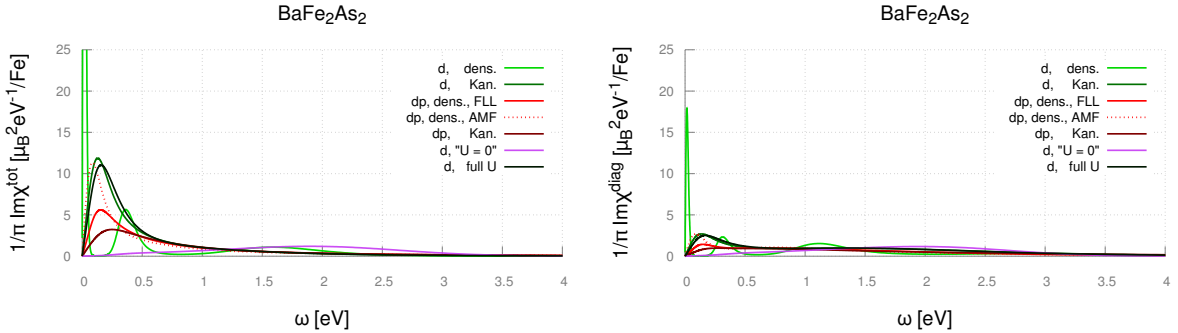


Figure 4.21: $BaFe_2As_2$: MaxEnt Spin-spin-susceptibility in real frequencies computed for the different models and interaction-types.

As for the results, the non-interacting case (purple) displays a rather featureless broad absorption spectrum extended roughly on the whole non-interacting bandwidth. As expected χ^{tot} equals χ^{diag} , since there are no vertex corrections for $U = J = V = 0$. In all the other models and Hamiltonians, instead structures appear at low energy. The position of the peak depends on the choice of the model as well as the Hamiltonian. It ranges from 15.7 meV (d -model dens. dens. int.) to 250 meV (dpp -model Kan. int.).

The most reliable among the d -model is probably the $full-U$ case, where we used a general orbital-dependent U -matrix as H^{int} . It has a peak-maximum at 157.4 meV. For this case, we have also fitted the following model spectral function to the data:

$$\text{Im}\chi^{\text{tot}}(\omega) = \frac{2a\gamma\omega}{4\gamma^2\omega^2 + (\omega^2 - \omega_0^2)^2}$$

The fit was performed via minimizing the quadratic difference between the model and the data at the data-points. Smaller frequencies were weighed comparably more ³.

This allows us to extract model parameters as

	Estimate	Standard Error	t-Statistic	P-Value
a	1.1296	0.00649518	173.913	$1.00 \cdot 10^{-876}$
ω_0	0.264915	0.00065306	405.651	$1.64 \cdot 10^{-1326}$
γ	0.251685	0.00147634	170.479	$2.33 \cdot 10^{-866}$

Notice that $\gamma \cong \omega_0$.

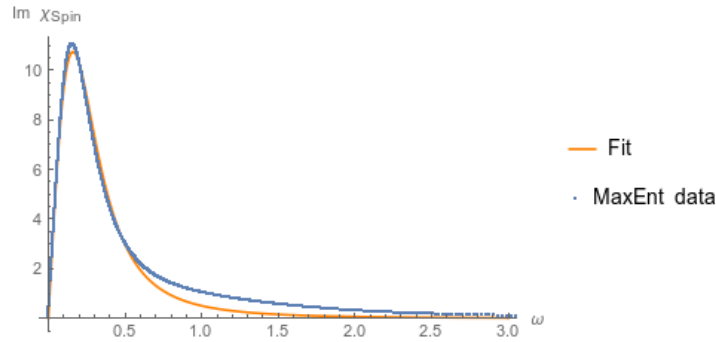


Figure 4.22: $BaFe_2As_2$: Comparison between the fitted model and the MaxEnt data.

Since the damping-parameter γ is slightly larger than the undamped-frequency ω_0 we are (barely) in the underdamped regime. The Fourier-transform of the model reads (in natural units) as

$$\chi^{\text{tot}}(t) = \theta(t)13.6638e^{-0.251685t} \sin(0.0826706t).$$

However, since the difference between γ and ω_0 is only marginal a better life-time estimate needs a more careful analysis based on the Fourier-transformed data in real time (see below).

³See Ch. 4.1.3 for a justification

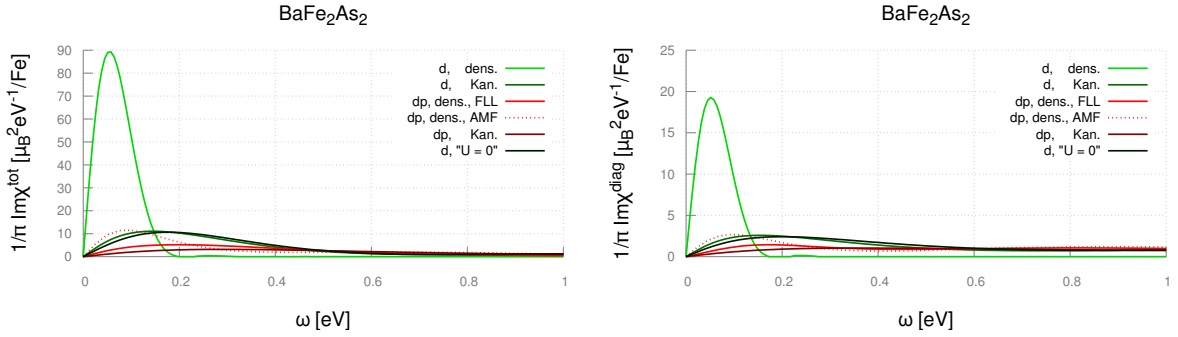


Figure 4.23: $BaFe_2As_2$ SpM: Spin-spin-susceptibility in real frequencies computed for the different models and interaction-types. The analytical continuation was done with sparse-modeling. The total susceptibility (left) is very similar in shape to the diagonal contribution only (right), but about a factor 4 larger. The peaks are in general broader than for MaxEnt. (We decided to use the results obtained by the more established MaxEnt-method for the further analysis.)

Susceptibilities in real time

The Fourier-transform can be easily carried out and from the fluctuation-dissipation-theorem one can also calculate the anti-commutator-correlator $F(t)$ without any difficulty. The results are shown in Fig. 4.24 and Fig. 4.25. We only show the correlation functions for $t > 0$ since $\chi(t)$ is zero for $t < 0$ and $F(t)$ is symmetric with respect to time.

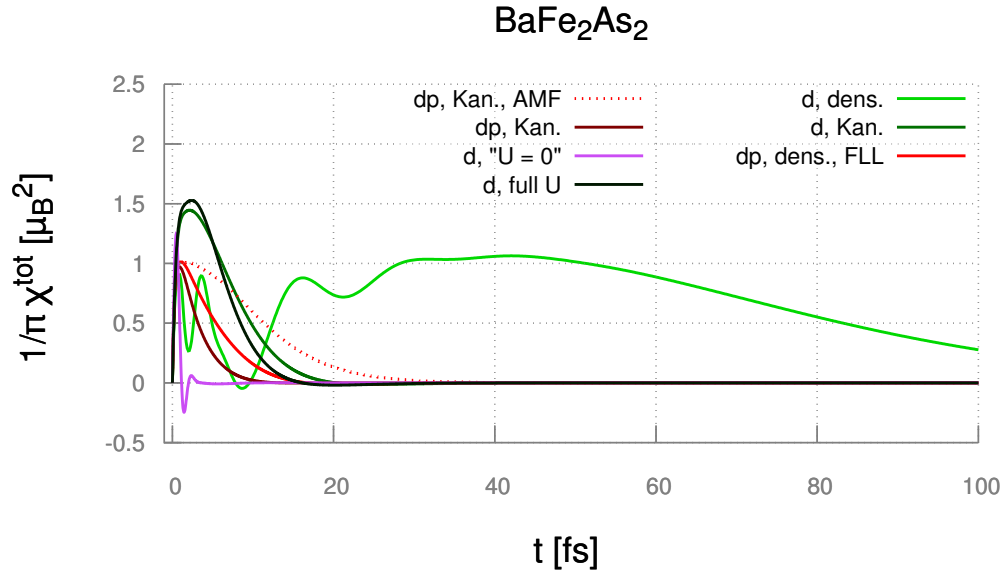


Figure 4.24: $BaFe_2As_2$: Spin-spin-susceptibility in real time computed for the different models and interaction-types.

We find $\chi(t)$ to decay (for cases except d , dens.) on an approximate time-scale of 2 – 20fs depending upon the choice of model and Hamiltonian. For d dens.-type-interaction the timescales are very different (more than by 100fs). Since we could already predict this behavior (roughly) from $\chi(\tau)$ and we checked them against a variety of different MaxEnt models as well as error-scales, it can be assumed that this effect is already present at the level of QMC. While an sizable effect on the dynamic of spin-fluctuations can be expected from the inclusion of spin-flip and pair-hopping terms in the interaction, the size of changes observed for the d -model data of $BaFe_2As_2$ is quite surprising, and probably requires further investigation. On the other hand, the difference in the results could also be an indication of the inapplicability of the approximations made to this family (see section 5).

However, why the neglect of pair-hopping and spin-flips has such a severe effect on the life-time of spin-excitations in $BaFe_2As_2$ is unclear.

$F(t)$ decays more rapidly on a time-scale of approximately 0.5 – 10fs. (and approximately 75fs for d ,dens. int.) Comparing this with the model-time-scales (for full U MaxEnt)

$$\begin{aligned} t_\gamma &= \frac{\hbar}{\gamma} = 2.48 fs \\ t_\omega &= \frac{\gamma}{\sqrt{\omega_0^2 - \gamma^2}} = 7.96 fs, \end{aligned} \quad (4.3)$$

we find a damping time-scale of 2.48fs and an oscillation frequency of 7.96fs.

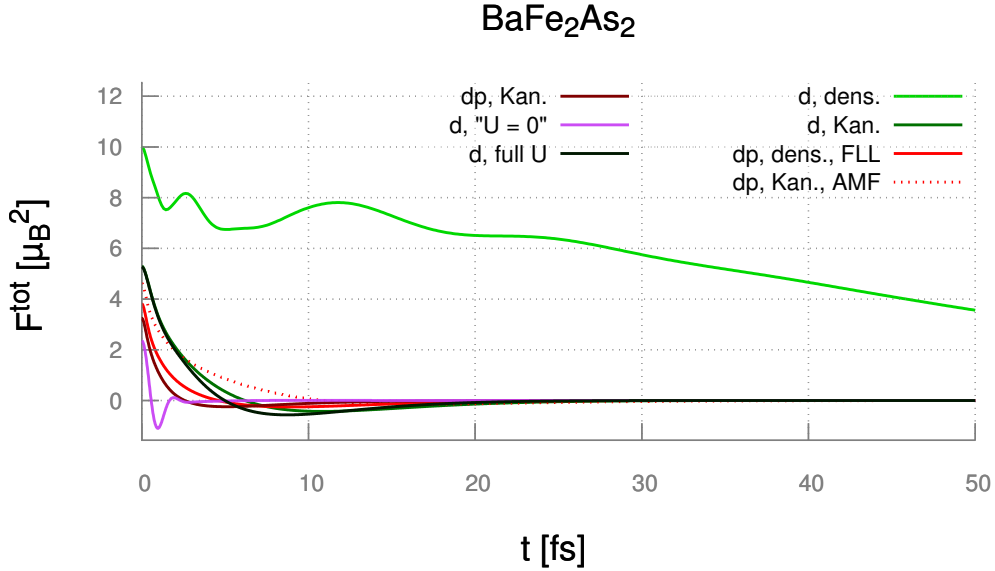


Figure 4.25: $BaFe_2As_2$: Spin-spin-anti-commutator correlation function in real time computed for the different models and interaction-types.

Cutoff dependence of the full integral

In Fig. 4.13 the energy cut-off dependence of the full (square) local magnetic moment is shown. The vertical dotted line marks a experimentally typical energy scale (for INS-measurements)

of 100meV. Our results show that only 5% (for dpp) to 20% (for d Kan int.) of the full local magnetic-moment would be captured within such a cut-off value for all cases except d -dens. For the d -model case with a density-density-type interaction one would already capture 50% of the total $\langle m^2 \rangle$. For the full U case (very similar to the d -model Kan. int. case) one would make approximately up to an 85% error.

$$m_{\text{loc},t=0}^2 = \frac{3}{\pi} \lim_{\Omega \rightarrow \infty} \frac{\int_{-\Omega}^{\Omega} \int_{\text{BZ}} \text{Im}\chi(\vec{q}, \omega) b(\omega) d\vec{q} d\omega}{\int_{\text{BZ}} d\vec{q}} = \frac{3}{\pi} \lim_{\Omega \rightarrow \infty} \int_{-\Omega}^{\Omega} \text{Im}\chi(\text{loc}, \omega) b(\omega) d\omega \quad (4.4)$$

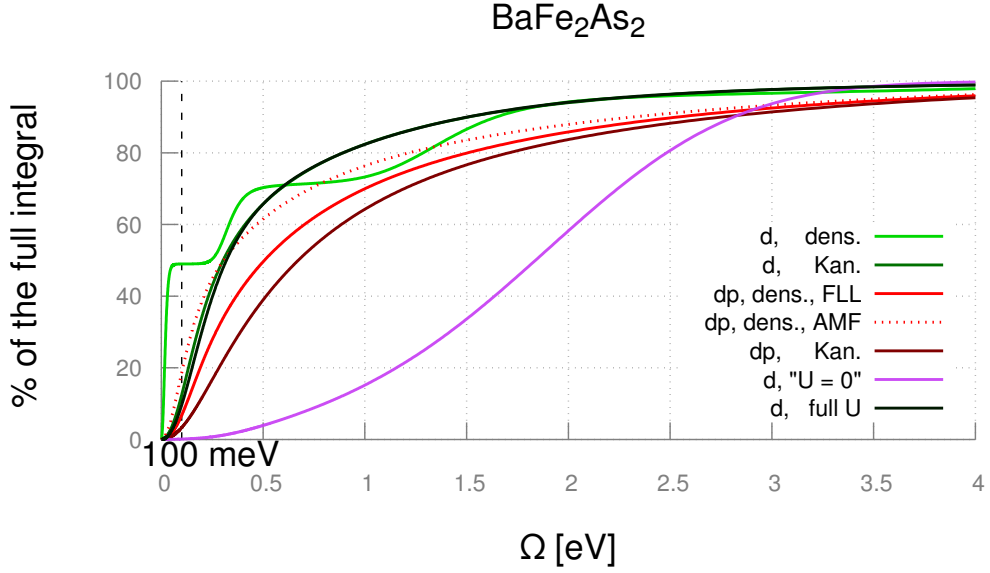


Figure 4.26: $BaFe_2As_2$: Cutoff dependency (finite Ω) of the squared local magnetic moment estimate $\langle m^2 \rangle$ (full integral in (Eq. 4.4)) computed for the different models and interaction-types.

4.2.4 Occupations and local magnetic momentum

We believe the disagreement between the results for the two different choices of Wannier-basis sets (d - vs. dp -model) is largely due to the different filling of the d -orbitals. While it is fixed to exactly 6 in the d -model we find $\sum_{\sigma,i} \langle n_{\sigma}^i \rangle$ ranging from 7.18 (dens., AMF) over 7.31 (Kan., FLL) to 7.34 (dens., FLL) (under the assumption that $n_0^d + n_0^p = 12$ see previous chapter for details).

In Tab. 4.3 we report the average occupations and double-occupations with the same spin while in Fig. 4.4 the average double-occupations with different spin are shown. Since we are in the paramagnetic phase the occupations can be deduced via symmetry ($\langle n_{i\uparrow} \rangle = \langle n_{i\downarrow} \rangle$). By comparing the two Tables once can also compute $C_{n_{i\sigma}n_{j\sigma'}} \equiv \langle n_{i\sigma}n_{j\sigma'} \rangle - \langle n_{i\sigma} \rangle \langle n_{j\sigma'} \rangle$ which measures the "degree of correlation".

We find LaFeAsO not to be particularly correlated. For example, by analyzing the results for the $3z^2 - r^2$ orbital (in full U), which has the largest U value, we get

$$C_{n_{1\uparrow}n_{1\downarrow}} = \langle n_{1\uparrow}n_{1\downarrow} \rangle - \langle n_{1\uparrow} \rangle \langle n_{1\downarrow} \rangle = 0.64 - 0.33^2 = -0.0796.$$

This orbital is, however not the most correlated one (with respect to the same orbital-index) in spite of having the the largest U -value. For example $C_{n_{4\uparrow}n_{4\downarrow}} = -0.1049$ which shows that the (orbital-dependent) U -value alone is not a good estimate for the degree of correlation.

The orbital-dependent role of Hund's exchange, on the other hand, can be estimated by comparing $h_{ij} \equiv \langle n_{i\uparrow}n_{j\uparrow} \rangle - \langle n_{i\uparrow}n_{j\downarrow} \rangle$. Applying this to our Tables (again for the full U case) we get $h_{14} = 0.06$, $h_{45} = 0.04$ and for all others $h_{ij} = 0.05$.

Comparing the occupation numbers with respect to the different models and Hamiltonians (considering the columns) we observe only minor changes with respect to the interaction Hamiltonians, but qualitatively different results with respect to the different Wannier-projections (d vs dp). In fact, this is ascribed to the considerably different filling of the d -manifold: In the d -model the filling of the d -orbital manifold was fixed to 6 electrons on 10 available places, for the dpp -model this represents a free parameter. In the later case we have assumed that the number of electrons of the Wannier basis-set considered the d -manifold together with the two p -manifolds is 12. The reasons for arriving at these numbers were laid out in the previous chapter. It should therefore not be assumed that the dp -results are automatically more valid than the d -ones.

At the same time, from the disagreement between the d - and the dp -model, one can not answer the question which one is, more or less, correct.

Eventually, the squared local magnetic moment (total as well as diagonal contribution) is shown on the table. ($\chi^{\text{tot}}(\tau = 0)$ and $\chi^{\text{diag}}(\tau = 0)$). A more detailed discussion of this particular result will be given in the next chapter.

	d-model			dp-model		
	H_U^D	H_U^K	H_{FLL}^{fullU}	H_{UFLL}^D	$H_{U,AMF}^D$	H_U^K
$\langle \mathbf{n}_{1\uparrow} \rangle$	0.66	0.67	0.64	0.80	0.79	0.80
$\langle n_{1\uparrow} n_{2\uparrow} \rangle$	0.45	0.41	0.39	0.58	0.56	0.57
$\langle n_{1\uparrow} n_{3\uparrow} \rangle$	0.45	0.41	0.39	0.58	0.56	0.57
$\langle n_{1\uparrow} n_{4\uparrow} \rangle$	0.44	0.38	0.39	0.57	0.55	0.56
$\langle n_{1\uparrow} n_{5\uparrow} \rangle$	0.47	0.42	0.42	0.58	0.57	0.57
$\langle \mathbf{n}_{2\uparrow} \rangle$	0.58	0.58	0.58	0.72	0.70	0.72
$\langle n_{2\uparrow} n_{3\uparrow} \rangle$	0.43	0.36	0.36	0.53	0.51	0.51
$\langle n_{2\uparrow} n_{4\uparrow} \rangle$	0.42	0.34	0.35	0.52	0.51	0.51
$\langle n_{2\uparrow} n_{5\uparrow} \rangle$	0.43	0.37	0.38	0.52	0.51	0.52
$\langle \mathbf{n}_{3\uparrow} \rangle$	0.58	0.58	0.58	0.72	0.70	0.72
$\langle n_{3\uparrow} n_{4\uparrow} \rangle$	0.42	0.34	0.35	0.52	0.51	0.51
$\langle n_{3\uparrow} n_{5\uparrow} \rangle$	0.43	0.37	0.38	0.52	0.51	0.52
$\langle \mathbf{n}_{4\uparrow} \rangle$	0.54	0.54	0.57	0.71	0.69	0.71
$\langle n_{4\uparrow} n_{5\uparrow} \rangle$	0.42	0.35	0.36	0.52	0.51	0.51
$\langle \mathbf{n}_{5\uparrow} \rangle$	0.64	0.62	0.62	0.72	0.72	0.72
$\sum_{i,\sigma} \langle n_{i,\sigma} \rangle$	6.00	6.00	6.00	7.34	7.18	7.31
$\chi^{tot}(\tau = 0)$	10.01	5.30	5.27	3.81	4.63	3.24
$\chi^{diag}(\tau = 0)$	3.45	3.29	3.29	2.39	2.55	2.41

Table 4.3: Comparison of orbital occupations of the *same spin* dependent on the interaction class as well as the model for $BaFe_2As_2$

	d-model			dp-model		
	H_U^D	H_U^K	H_{FLL}^{fullU}	$H_{U,FLL}^D$	$H_{U,AMF}^D$	H_U^K
$\langle \mathbf{n}_{1\uparrow} \mathbf{n}_{1\downarrow} \rangle$	0.36	0.39	0.33	0.61	0.59	0.61
$\langle n_{1\uparrow} n_{2\downarrow} \rangle$	0.30	0.36	0.34	0.55	0.52	0.55
$\langle n_{1\uparrow} n_{3\downarrow} \rangle$	0.30	0.36	0.34	0.55	0.52	0.55
$\langle n_{1\uparrow} n_{4\downarrow} \rangle$	0.26	0.33	0.33	0.54	0.51	0.54
$\langle n_{1\uparrow} n_{5\downarrow} \rangle$	0.36	0.39	0.37	0.56	0.54	0.56
$\langle \mathbf{n}_{2\uparrow} \mathbf{n}_{2\downarrow} \rangle$	0.22	0.24	0.25	0.47	0.43	0.46
$\langle n_{2\uparrow} n_{3\downarrow} \rangle$	0.24	0.30	0.31	0.48	0.45	0.49
$\langle n_{2\uparrow} n_{4\downarrow} \rangle$	0.19	0.28	0.30	0.47	0.43	0.48
$\langle n_{2\uparrow} n_{5\downarrow} \rangle$	0.30	0.33	0.33	0.49	0.47	0.49
$\langle \mathbf{n}_{3\uparrow} \mathbf{n}_{3\downarrow} \rangle$	0.22	0.24	0.25	0.47	0.43	0.46
$\langle n_{3\uparrow} n_{4\downarrow} \rangle$	0.19	0.28	0.30	0.47	0.43	0.48
$\langle n_{3\uparrow} n_{5\downarrow} \rangle$	0.30	0.33	0.33	0.49	0.47	0.49
$\langle \mathbf{n}_{4\uparrow} \mathbf{n}_{4\downarrow} \rangle$	0.13	0.17	0.22	0.44	0.40	0.44
$\langle n_{4\uparrow} n_{5\downarrow} \rangle$	0.26	0.30	0.32	0.48	0.45	0.49
$\langle \mathbf{n}_{5\uparrow} \mathbf{n}_{5\downarrow} \rangle$	0.34	0.32	0.31	0.48	0.47	0.48

Table 4.4: Comparison of orbital occupations with *different* spin dependent on the interaction class as well as the model for $BaFe_2As_2$

4.3 *LiFeAs*

4.3.1 One-particle-properties in the d -model

In figure 4.27 we show the self-energy as well as the Green's function of *LiFeAs* for a density-density type interaction in the d -model only. Figure 4.28 show the corresponding data for a, full $SU(2)$ symmetric Kanamori-type interaction. In both cases we used the averaged values of the Coulomb-overlap integrals (\bar{U} , \bar{J} and \bar{V}). For the data shown in Figure 4.29 instead this assumption was lifted as we used the full-orbital dependence regarding the interaction terms.

$\langle U \rangle$, $\langle J \rangle$ and $\langle V \rangle$: Averaged Coulomb interaction

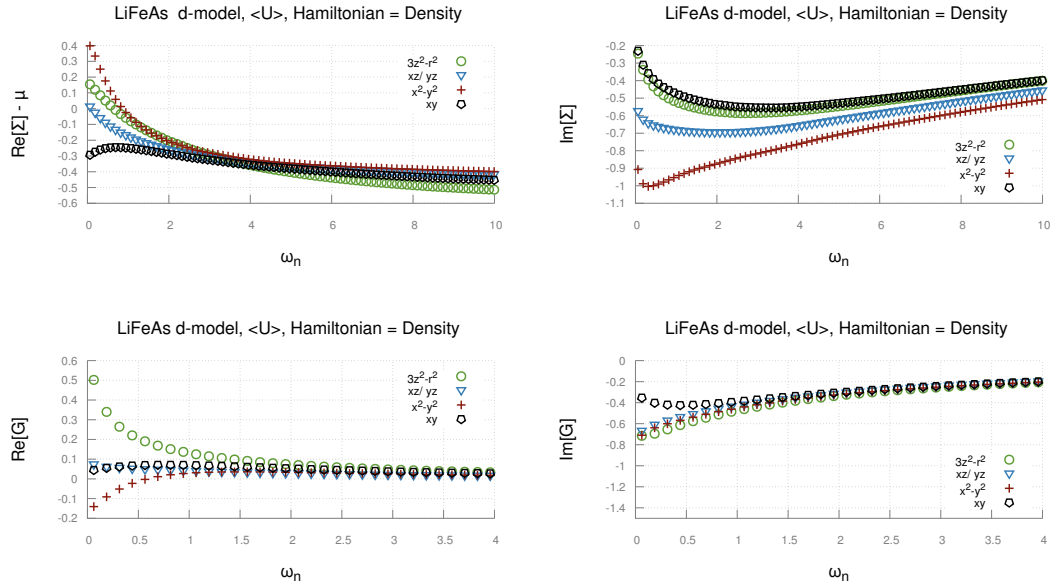


Figure 4.27: DFT+DMFT results of the single-particle properties of *LiFeAs* in the d -only-model with orbital averaged Coulomb interactions used for a density-density-type interaction.

Comparing figure 4.27 with 4.28 we find the inclusion of the full $SU(2)$ symmetry does change the physics for *LiFeAs*. This is in contrast to weaker correlated materials (e.g. *LaFeAsO*) where Kanamori- and density-type-interaction yielded similar results for the d -calculations. From the $\lim_{i\omega_n \rightarrow 0} \text{Im}\Sigma$ and $\lim_{i\omega_n \rightarrow 0} \text{Im}G$ we find the Kanamori-case to be more metallic. For example the $x^2 - y^2$ -orbital has an $\text{Im}\Sigma(0) \approx -0.8$ for for the dens. case, but $\approx -0.05 - 0.1$ in the Kanamori case. Therefore the $x^2 - y^2$ orbital will have for, the dens.-dens.-case, a significantly more broadened spectral function $\mathcal{A}^{x^2-y^2}(\omega)$ close to the Fermi-level. For the xz/yz -orbitals similar differences are observed. For both interaction types the $3z^2 - r^2$ - and $x^2 - y^2$ -orbitals are shifted to higher energies whereas the xy -orbital is shifted downwards (although the shift magnitudes is different for the two cases) as it can be inferred from $\text{Re}\Sigma$ (upper left figures). A similar trend for the shift of the orbitals is found also in the full-U calculations.

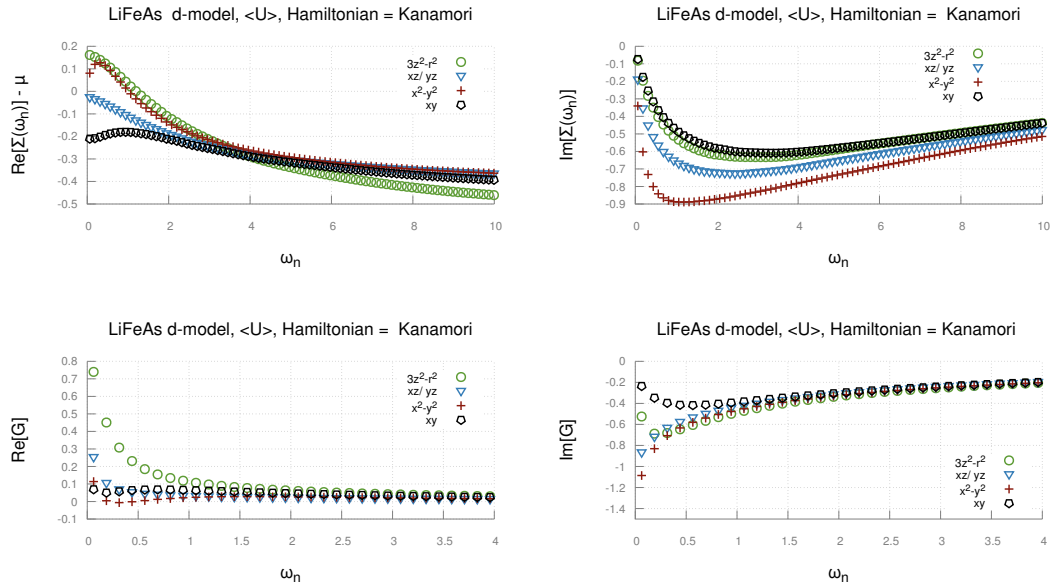


Figure 4.28: DFT+DMFT results of the single-particle properties of *LiFeAs* in the *d*-only-model with orbital averaged Coulomb interactions used for a Kanamori-type interaction calculation.

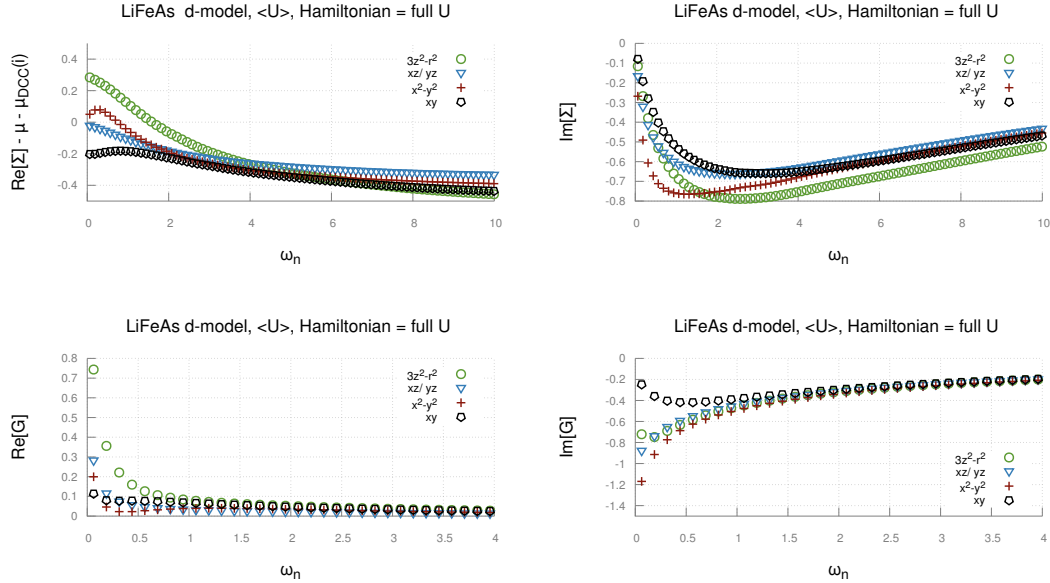


Figure 4.29: DFT+DMFT results of the single-particle properties of *LiFeAs* in the *d*-only-model with "full U" interaction calculation.

At the same time, comparing the two cases with orbital-averaged interaction-terms with the orbital-resolved U-term case we find that the roles of the orbitals have changed significantly. This is especially true for the " e_g "-orbitals: The $3z^2 - r^2$ - and $x^2 - y^2$ -orbitals have a larger spectral weight at the Fermi-surface, and the $x^2 - y^2$ -orbitals is more metallic for the full U -case. The " t_{2g} "-orbitals are less affected by non-averaged interaction terms. Overall, for $LiFeAs$ in the d -model, the differences between den.-int. and the others (Kan. and full U) are more severe than between Kan. int. and full U .

The qualitatively the general trend is that all orbitals show a metallic character and large quasi-particle excitation life-times in the d -only model.

4.3.2 One-particle-properties in the dpp -model

Fig. 4.30 and Fig. 4.31 show the self-energies and Green's functions in Matsubara frequencies for density-density- as well as for Kanamori interaction computed with the dp -Wannier basis set for $LiFeAs$. In both cases the U, V and J values were averaged over all orbitals.

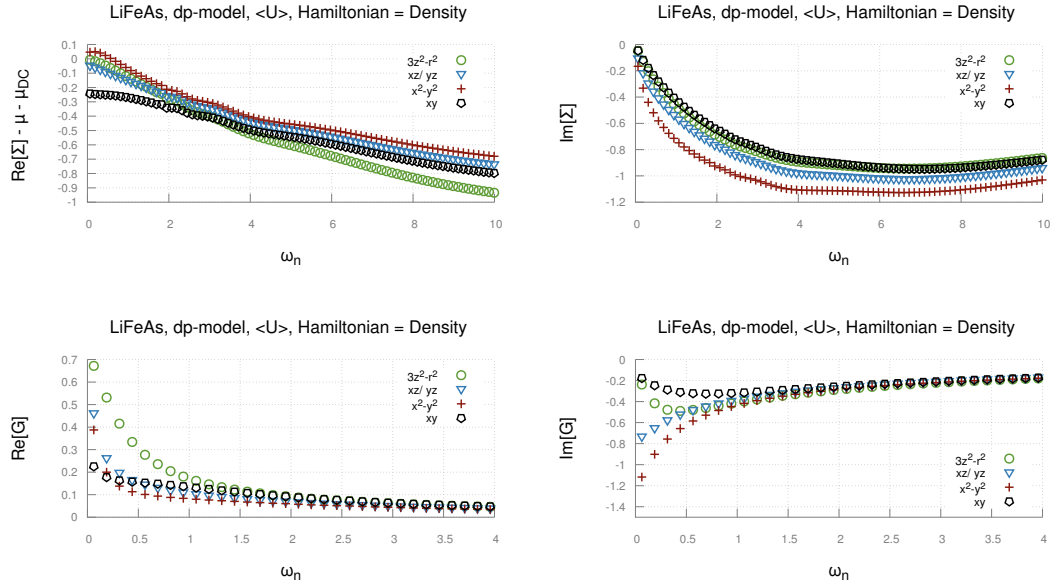


Figure 4.30: DFT+DMFT results of the single-particle properties of $LiFeAs$, computed for the dp -model with orbital-averaged Coulomb interaction in density-density-type interaction. We used the FLL for the DCC

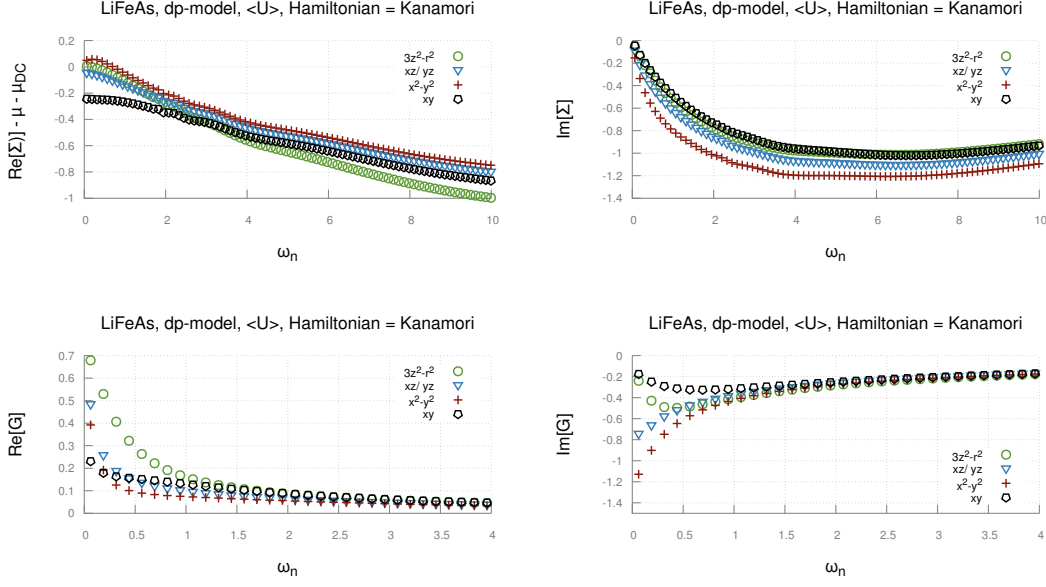
Kanamori interaction:

Figure 4.31: DFT+DMFT results of the single-particle properties of *LiFeAs*, computed for the *dp*-model with orbital-averaged Coulomb interaction in Kanamori-type interaction. We used the FLL for the DCC

The two sets of figures show an overall similar behavior. From the imaginary part of the self-energy, one can just deduce a slightly larger quasi-particle excitation lifetime for the density-density case since $|\text{Im} \Sigma^{\text{Kan.}}(i\omega_n)| < |\text{Im} \Sigma^{\text{dens.}}(i\omega_n)|$. However, the differences are not large enough to result in a major difference in $\text{Im} G$. The imaginary part of the Green's functions almost identical, regarding these two interaction types. From the real part of the self energy we find the trend that $\text{Re} \Sigma_i^{\text{Kanamori}} > \text{Re} \Sigma_i^{\text{Density}}$, but again the differences are very small.

The comparison to the *d*-model full-*U* case shows a very different picture. This is mostly due to the changed number of electrons in the 3d bands of iron. Which is exactly 6.00 for the *d*-only-model, but ranges between 7.25 (Kan.) to 7.27 (dens) in the *dpp*-model. The different physics can be seen from the imaginary part of the self-energy. For full *U* $\text{Im} \Sigma$ goes more rapid to zero (slope), corresponding to a larger mass-renormalization. However, $|\text{Im} \Sigma^{\text{fullU}}(i\omega_1)| > |\text{Im} \Sigma^{\text{dp}}(i\omega_1)|$. It is not immediately clear which of the two models experiences longer quasi-particle- life-times. The major difference in $\text{Im} G(i\omega_n)$ is the increased spectral weight at $\omega = 0$ for full *U* in the $3z^2 - r^2$ -orbital.

4.3.3 Model comparison of the two-particle-properties: Spin-spin susceptibilities

In this subsection we compare the spin-spin-susceptibility χ computed with different models and interaction terms for *LiFeAs*. We will focus our attention in particular to the difference between the χ^{tot} and χ^{diag} , is entirely due to vertex corrections. First the QMC-data are shown (in imaginary time in Fig. 4.32 and in Matsubara frequencies in Fig. 4.33). Second, the analytically continued data (in real frequencies) have been computed. From these we could extract the different time-scales of the spin-dynamics of the system. Third, we show the Fourier transformed susceptibilities in real frequencies. From the fluctuation-dissipation theorem we also computed the symmetric anti-commutator-correlation function $F(t)$, which is better suited to study the quantum-mechanical spin-screening effects.

Susceptibilities in imaginary time/ frequency

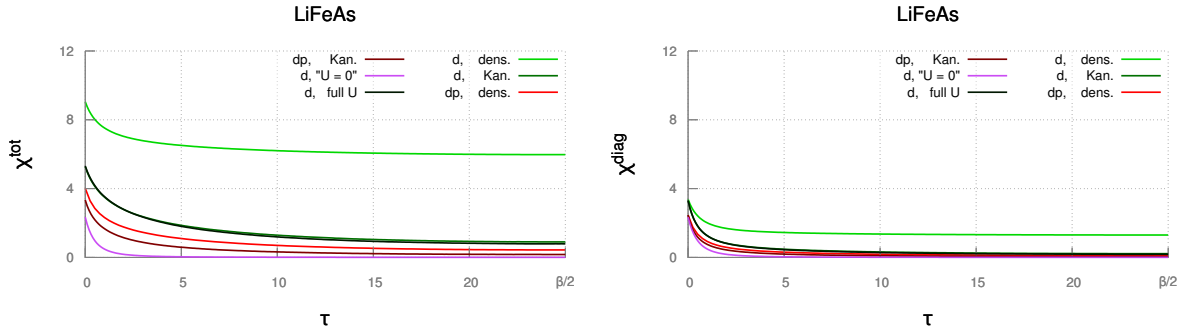


Figure 4.32: *LiFeAs*: Spin-spin-susceptibility in imaginary time computed for the different models and interaction-types.

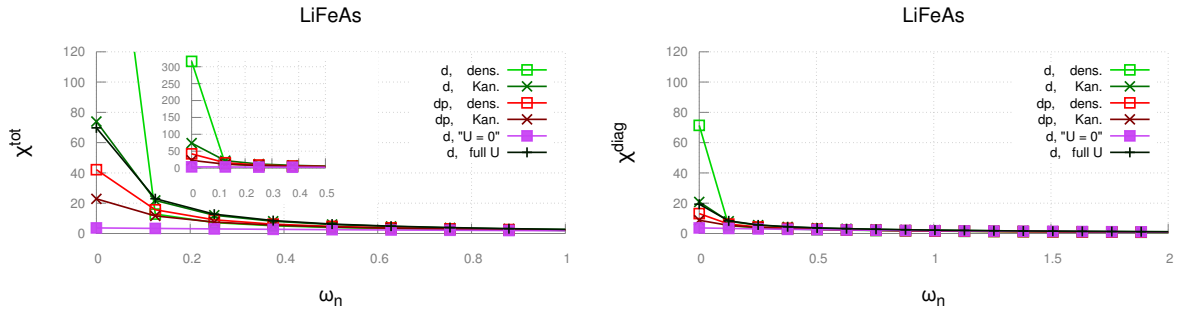


Figure 4.33: *LiFeAs*: Spin-spin-susceptibility in Matsubara frequencies computed for the different models and interaction-types.

An interesting feature in Fig. 4.32 is that for the d -model the Kanamori-interaction with averaged U -terms gives almost exactly the same results as the d -model with full U interaction. This is rather remarkable since it could not be expected on the basis of the one-particle properties above. One may interpret it as a posteriori justification of the averaged procedure, to be applied for calculations of orbital summed physical quantities.

Comparing the left and right sub-figures of Fig. 4.32, we see that, especially for the density-density interaction, in the d -model a significant contribution comes from vertex corrections. (With the obvious exception of the $U = 0$ case, where $\chi^{\text{tot}} = \chi^{\text{diag}}$). Furthermore, we find the dp -calculation to yield, overall, a smaller local magnetic moment than the d -only.

Susceptibilities in real frequencies

In Fig. 4.34 and in Fig. 4.36 the analytically continued spin-spin-susceptibilities via two different methods are shown. To obtain Fig. 4.34, we used the Maximum-Entropy-method (more specifically [40] with an additional selection criterion discussed in section 2.4.3). Whereas for Fig. 4.36, we have used Sparse-Modeling[32].

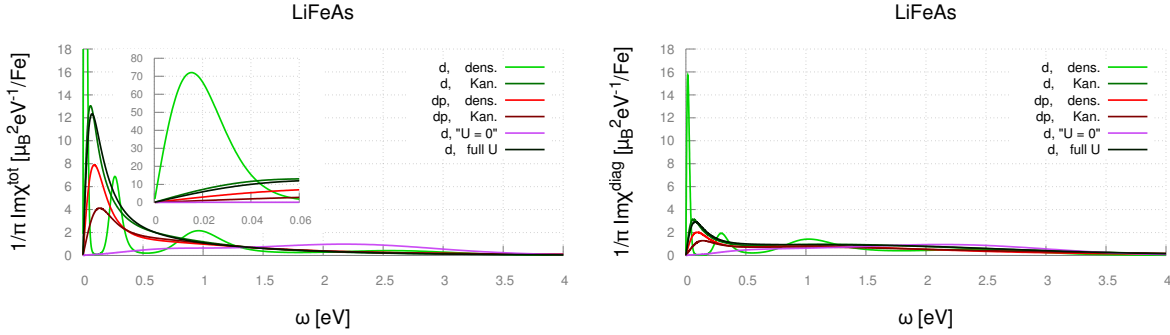


Figure 4.34: *LiFeAs*: **MaxEnt** Spin-spin-susceptibility in real frequencies computed for the different models and interaction-types.

The non-interacting case (purple) shows a very featureless broad absorption spectrum extended roughly on the whole non-interacting bandwidth. As expected χ^{tot} equals χ^{diag} , since there are no vertex corrections for $U = J = V = 0$.

In all the other models and Hamiltonians low energy peak appears, instead. The position of the peak depends strongly on the choice of the model as well as the Hamiltonian. Its peak-location (maximum) ranges from 15 meV (d -model dens. dens. int.) to 138 meV (dpp -model Kan. int.).

The most reliable of the d -model is probably the *full* - U case, since it exploits a general orbital-dependent U -matrix as H^{int} . In that calculation, the peak-maximum is found at 75.1 meV. For this case we have fitted the following model spectral function to the data.

$$\text{Im}\chi^{\text{tot}}(\omega) = \frac{2a\gamma\omega}{4\gamma^2\omega^2 + (\omega^2 - \omega_0^2)^2}$$

The fit was performed via minimizing the quadratic difference between the model and the data at the data-points. Smaller frequencies were taken more into account⁴.

This allows us to extract model parameters as

	Estimate	Standard Error	t-Statistic	P-Value
a	1.35122	0.0157477	85.8045	$1.60 \cdot 10^{-525}$
ω_0	0.245857	0.00135745	181.117	$7.20 \cdot 10^{-898}$
γ	0.455235	0.00521214	87.3415	$9.13 \cdot 10^{-534}$

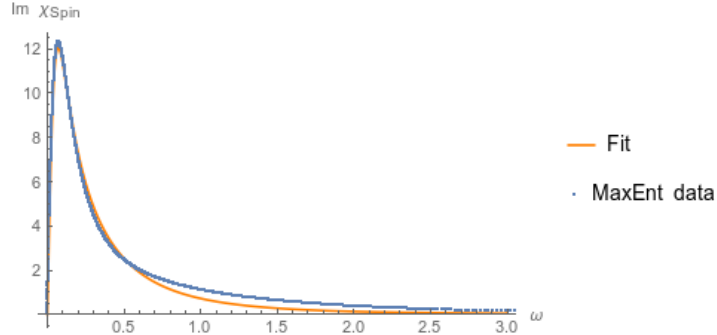


Figure 4.35: LiFeAs: Comparison between the fitted model and the MaxEnt data.

Since the damping-parameter γ is larger than the undamped-frequency ω_0 we are in the overdamped regime. The Fourier-transform of the model reads (in natural units) as

$$\chi^{\text{tot}}(t) = \theta(t) 3.52674e^{-0.455235t} \sinh(0.383137t).$$

For a more qualitative analysis of the time-scales we Fourier-transformed our data to real time (under consideration of the KK-relation).

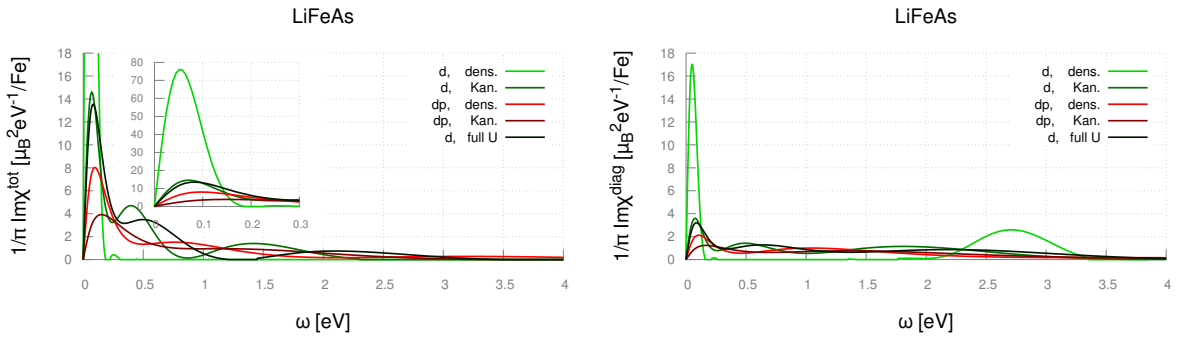


Figure 4.36: LiFeAs: SpM Spin-spin-susceptibility in real frequencies computed for the different models and interaction-types.

⁴See Ch. 4.1.3 for a justification

Susceptibilities in real time

The Fourier-transform can be easily carried out and from the fluctuation-dissipation-theorem one can also calculate the anti-commutator-correlator $F(t)$ without any difficulty. The result with restored SI-units are shown in Fig. 4.37 and Fig. 4.38. We only show them for $t > 0$ since $\chi(t)$ is zero for $t < 0$ and $F(t)$ is symmetric with respect to time.

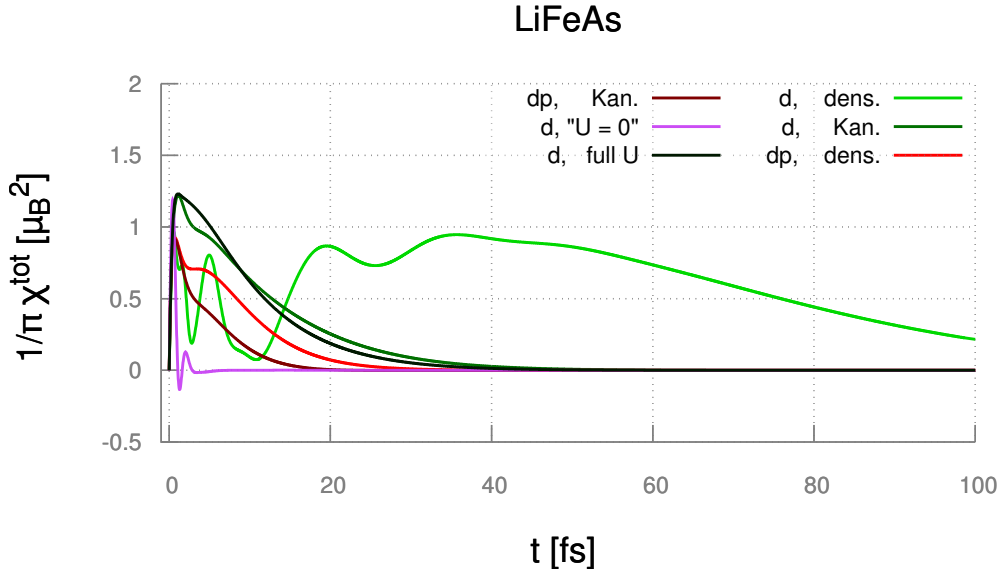


Figure 4.37: *LiFeAs*: Spin-spin-susceptibility in real time compared with respect to the different models and interaction-types.

We find $\chi(t)$ to decay on an approximate time-scale of 10 (full U/Kan. d.) to 80 fs (dens. d.) depending upon the choice of model and Hamiltonian. $F(t)$ decays more rapidly on a time-scale of approximately 4 – 60fs. Comparing this with the time-scales from the previously presented full U MaxEnt

$$\begin{aligned}
 t_\gamma &= \frac{\hbar}{\gamma} = 2.67721 \text{ fs} \\
 t_\omega &= \frac{\hbar}{\sqrt{|\omega_0^2 - \gamma^2|}} = 1.71796 \text{ fs}, \\
 t_{\tilde{\gamma}} &= \frac{\hbar}{\gamma - \omega} = 9.129 \text{ fs},
 \end{aligned} \tag{4.5}$$

we find an effective damping time-scale of 9.129 fs which is in good agreement with the numerical results (shown in Fig. 4.37)

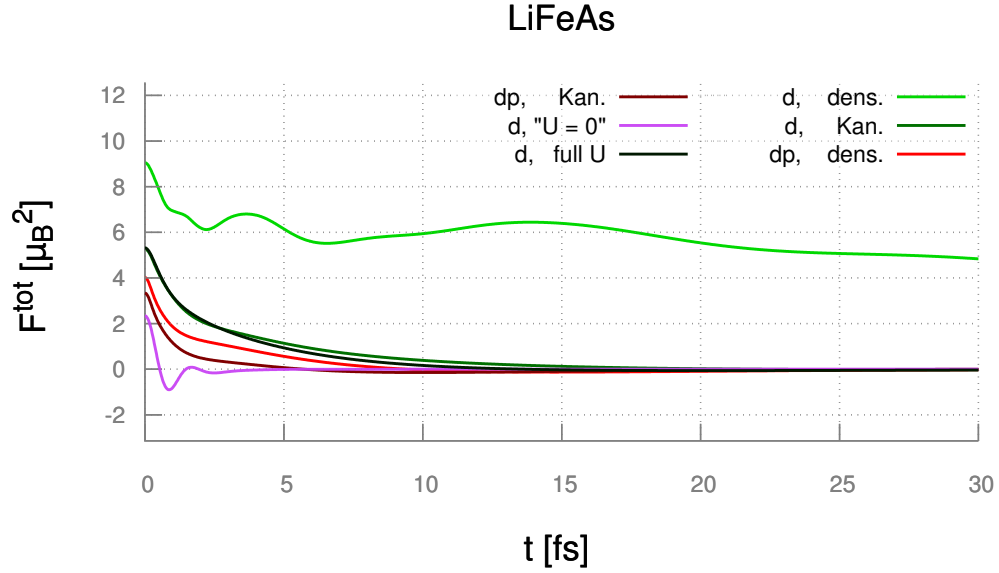


Figure 4.38: *LiFeAs*: Spin-spin-anti-commutator correlation function in real time computed for the different models and interaction-types.

Cutoff dependence of the full integral

$$m_{\text{loc},t=0}^2 = \frac{3}{\pi} \lim_{\Omega \rightarrow \infty} \frac{\int_{-\Omega}^{\Omega} \int_{\text{BZ}} \text{Im} \chi(\vec{q}, \omega) b(\omega) d\vec{q} d\omega}{\int_{\text{BZ}} d\vec{q}} = \frac{3}{\pi} \lim_{\Omega \rightarrow \infty} \int_{-\Omega}^{\Omega} \text{Im} \chi_{\text{loc}}(\omega) b(\omega) d\omega \quad (4.6)$$

In Fig. 4.39 the energy cut-off dependence of the full (square) local magnetic moment is shown. The vertical dotted line marks a experimentally typical energy scale (for INS-measurements) of 100meV. Our results show that only 5% (for *dp*) to 45% (for *d* dens.dens int.) of the full local magnetic-moment would be inside such a cut-off value. For the full *U* case (very similar to the *d*-model Kan. int. case) one would make, then, an 75% error.

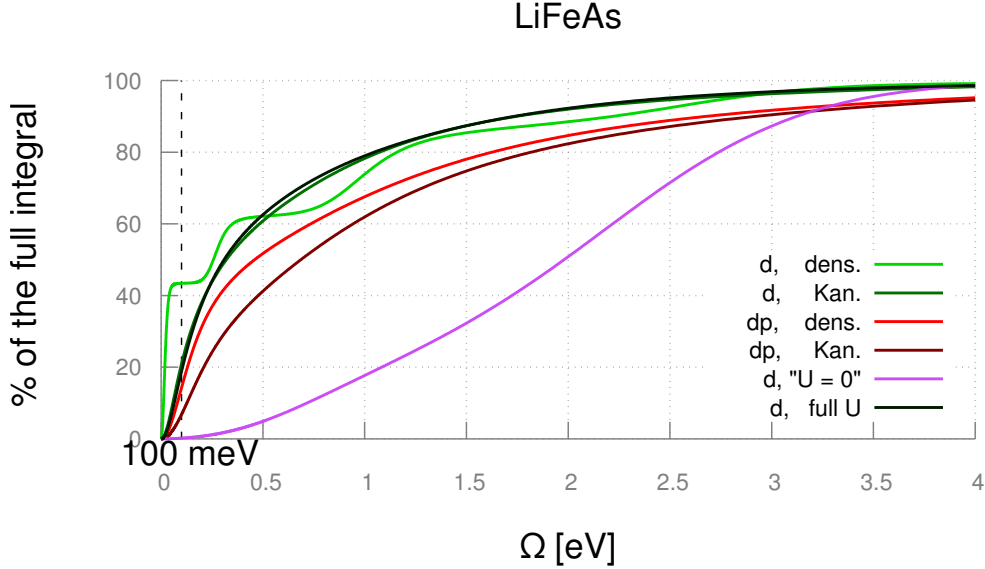


Figure 4.39: *LiFeAs*: Cutoff dependency (finite Ω) of the squared local magnetic moment estimate $\langle m^2 \rangle$ (full integral in (Eq. 4.6)) computed for the different models and interaction-types.

4.3.4 Occupations and local magnetic momentum

In Tab. 4.5 we report the average occupations and double-occupations with the same spin while in Fig. 4.6 the average double-occupations with different spin are shown. Since we are in the paramagnetic phase the occupations can be deduced via symmetry ($\langle n_{i\uparrow} \rangle = \langle n_{i\downarrow} \rangle$). By comparing the two Tables once can also compute $C_{n_{i\sigma}n_{j\sigma'}} \equiv \langle n_{i\sigma}n_{j\sigma'} \rangle - \langle n_{i\sigma} \rangle \langle n_{j\sigma'} \rangle$ which measures the "degree of correlation".

We find *LiFeAs* to be slightly more correlated than *BaFe₂As₂*. For example, by analyzing the results for orbital 5 (in full U), which has the largest U value, we get

$$C_{n_{5\uparrow}n_{5\downarrow}} = \langle n_{5\uparrow}n_{5\downarrow} \rangle - \langle n_{5\uparrow} \rangle \langle n_{5\downarrow} \rangle = -0.0744$$

This orbital is, however not the most correlated one (with respect to the same orbital-index) in spite of having the the largest U -value. For example $C_{n_{4\uparrow}n_{4\downarrow}} = -0.1364$ which shows that the (orbital-dependent) U -value alone is not a good estimate for the degree of correlation.

The orbital-dependent role of Hund's exchange, on the other hand, can be estimated by comparing $h_{ij} \equiv \langle n_{i\uparrow}n_{j\uparrow} \rangle - \langle n_{i\uparrow}n_{j\downarrow} \rangle$. Applying this to our Tables (again for the full U case) we get $h_{14} = h_{24} = h_{34} = 0.06$, $h_{23} = h_{45} = 0.05$ whereas all the other $h_{ij} = 0.04$. Thus we conclude that the $x^2 - y^2$ orbital (4) has the largest Hund's coupling effect.

Comparing the occupation numbers with respect to the different models and Hamiltonians (considering the columns) we observe only minor changes with respect to the interaction Hamiltonians, but qualitatively different results with respect to the different Wannier-projections (d vs dp). In fact, this is ascribed to the considerably different filling of the d -manifold: In the d -model the filling of the d -orbital manifold was fixed to 6 electrons on 10 available places,

for the dp -model this represents a free parameter. In the later case we have assumed that the number of electrons of the Wannier basis-set considered the d -manifold together with the two p -manifolds is 12. The reasons for arriving at these numbers were laid out in the previous chapter. We also observe $|\langle n_{i\sigma} \rangle^{\text{den.,d}} - \langle n_{i\sigma} \rangle^{\text{Kan.,d}}| < |\langle n_{i\sigma} n_{j\sigma'} \rangle^{\text{den.,d}} - \langle n_{i\sigma} n_{j\sigma'} \rangle^{\text{Kan.,d}}| \forall \sigma, \sigma' \forall i \neq j$, showing the broken $SU(2)$ symmetry of the density-density interaction.

At the same time, from the disagreement between the d - and the dp -model, one can not answer the question which one is, more or less, correct.

Eventually, the squared local magnetic moment (total as well as diagonal contribution) is shown on the table. ($\chi^{\text{tot}}(\tau = 0)$ and $\chi^{\text{diag}}(\tau = 0)$). A more detailed discussion of this particular result will be given in the next chapter.

	d-model			dpp-model with FLL DCC	
	H_U^D	H_U^K	H_{FLL}^{fullU}	H_U^D	H_U^K
$\langle \mathbf{n}_{1\uparrow} \rangle$	0.70	0.70	0.68	0.80	0.80
$\langle n_{1\uparrow} n_{2\uparrow} \rangle$	0.44	0.41	0.39	0.57	0.56
$\langle n_{1\uparrow} n_{3\uparrow} \rangle$	0.44	0.41	0.39	0.57	0.56
$\langle n_{1\uparrow} n_{4\uparrow} \rangle$	0.46	0.41	0.42	0.56	0.54
$\langle n_{1\uparrow} n_{5\uparrow} \rangle$	0.46	0.43	0.43	0.59	0.58
$\langle \mathbf{n}_{2\uparrow} \rangle$	0.57	0.56	0.56	0.71	0.71
$\langle n_{2\uparrow} n_{3\uparrow} \rangle$	0.39	0.34	0.34	0.51	0.50
$\langle n_{2\uparrow} n_{4\uparrow} \rangle$	0.42	0.35	0.35	0.50	0.49
$\langle n_{2\uparrow} n_{5\uparrow} \rangle$	0.39	0.35	0.36	0.53	0.52
$\langle \mathbf{n}_{3\uparrow} \rangle$	0.57	0.56	0.57	0.71	0.71
$\langle n_{3\uparrow} n_{4\uparrow} \rangle$	0.42	0.35	0.35	0.50	0.49
$\langle n_{3\uparrow} n_{5\uparrow} \rangle$	0.39	0.35	0.36	0.53	0.52
$\langle \mathbf{n}_{4\uparrow} \rangle$	0.55	0.56	0.58	0.68	0.68
$\langle n_{4\uparrow} n_{5\uparrow} \rangle$	0.40	0.36	0.37	0.51	0.50
$\langle \mathbf{n}_{5\uparrow} \rangle$	0.62	0.61	0.62	0.74	0.74
$\sum_{i,\sigma} \langle n_{i,\sigma} \rangle$	6.00	6.00	6.00	7.27	7.25
$\chi^{\text{tot}}(\tau = 0)$	9.04	5.27	5.32	4.02	3.34
$\chi^{\text{diag}}(\tau = 0)$	3.38	3.29	3.31	2.45	2.47

Table 4.5: Comparison of orbital occupations of the *same* spin dependent on the interaction class as well as the model for $LiFeAs$

	d-model			dpp-model with FLL DCC	
	$H_{\bar{U}}^D$	$H_{\bar{U}}^K$	H_{FLL}^{fullU}	$H_{\bar{U}}^D$	$H_{\bar{U}}^K$
$\langle \mathbf{n}_{1\uparrow} \mathbf{n}_{1\downarrow} \rangle$	0.43	0.44	0.38	0.62	0.61
$\langle n_{1\uparrow} n_{2\downarrow} \rangle$	0.33	0.37	0.35	0.54	0.55
$\langle n_{1\uparrow} n_{3\downarrow} \rangle$	0.33	0.37	0.35	0.54	0.55
$\langle n_{1\uparrow} n_{4\downarrow} \rangle$	0.31	0.36	0.36	0.52	0.52
$\langle n_{1\uparrow} n_{5\downarrow} \rangle$	0.38	0.40	0.39	0.57	0.57
$\langle \mathbf{n}_{2\uparrow} \mathbf{n}_{2\downarrow} \rangle$	0.21	0.22	0.22	0.45	0.45
$\langle n_{2\uparrow} n_{3\downarrow} \rangle$	0.23	0.28	0.29	0.47	0.47
$\langle n_{2\uparrow} n_{4\downarrow} \rangle$	0.20	0.27	0.29	0.44	0.45
$\langle n_{2\uparrow} n_{5\downarrow} \rangle$	0.29	0.31	0.32	0.49	0.50
$\langle \mathbf{n}_{3\uparrow} \mathbf{n}_{3\downarrow} \rangle$	0.21	0.22	0.22	0.45	0.45
$\langle n_{3\uparrow} n_{4\downarrow} \rangle$	0.20	0.27	0.29	0.44	0.45
$\langle n_{3\uparrow} n_{5\downarrow} \rangle$	0.29	0.31	0.32	0.49	0.50
$\langle \mathbf{n}_{4\uparrow} \mathbf{n}_{4\downarrow} \rangle$	0.14	0.17	0.20	0.39	0.38
$\langle n_{4\uparrow} n_{5\downarrow} \rangle$	0.26	0.31	0.32	0.47	0.48
$\langle \mathbf{n}_{5\uparrow} \mathbf{n}_{5\downarrow} \rangle$	0.31	0.31	0.31	0.51	0.51

Table 4.6: Comparison of orbital occupations with *different* spin dependent on the interaction class as well as the model for *LiFeAs*

4.4 KFe_2As_2

4.4.1 One-particle-properties in the d -model

In figure 4.40 we show the self-energy as well as the Green's function of KFe_2As_2 for a density-density type interaction in the d -model only. Figure 4.41 show the corresponding data for a, full $SU(2)$ symmetric Kanamori-type interaction. In both cases we used the averaged values of the Coulomb-overlap integrals (\bar{U} , \bar{J} and \bar{V}). For the data shown in Figure 4.42 instead this assumption was lifted as we used the full-orbital dependence regarding the interaction terms.

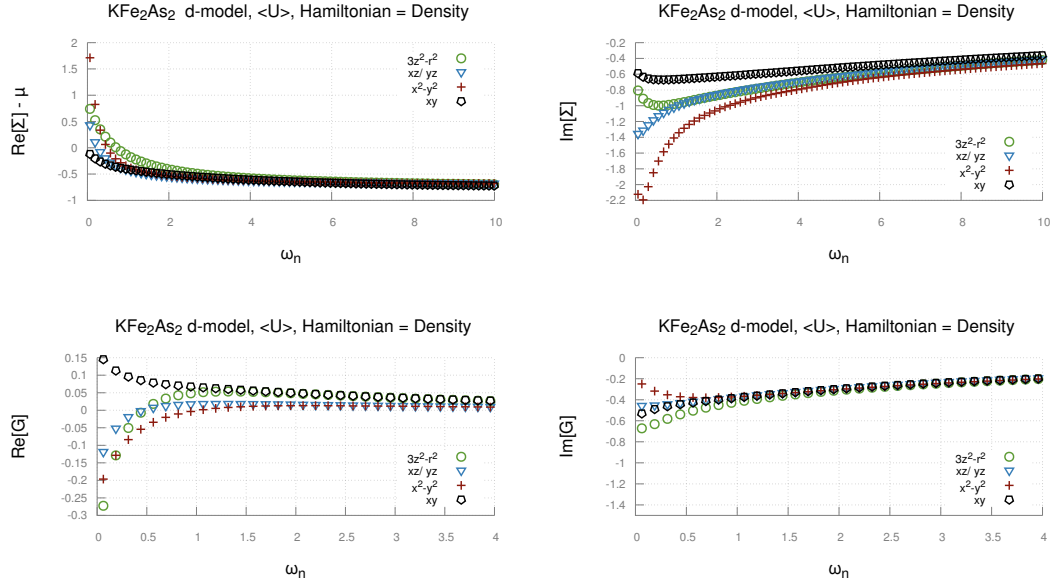


Figure 4.40: DFT+DMFT results of the single-particle properties of KFe_2As_2 in the d -only-model with orbital averaged Coulomb interactions used for a density-density-type interaction.

Comparing figure 4.40 with 4.41 we find the inclusion of the full $SU(2)$ symmetry changes the physics drastically. From the $\lim_{i\omega_n \rightarrow 0} \text{Im}\Sigma$ and from $\lim_{i\omega_n \rightarrow 0} \text{Im}G$ we find the Kanamori-case to be much more metallic. For example, the $x^2 - y^2$ and the xz/yz -orbitals are almost insulating for a dens.-type interaction, whereas $\text{Im}\Sigma^{\text{Kan.}}(0) \approx 0$.

For both interaction types the $3z^2 - r^2$ orbital was shifted upwards in energy. The most severe difference in $\text{Re}\Sigma$ involves the $x^2 - y^2$ -orbital: while it is shifted slightly down for Kanamori (by about 0.1eV) it is shifted up for dens.-dens.-interaction by about 2eV!. This leads to an almost insulating solution for the $3z^2 - r^2$ -orbital in dens. int., whereas the Kan. int. case has a large peak in the analytically continued spectral function centered almost at ϵ_F . (For the analytically continued spectral function we refer to Fig.5.1 in the next chapter).

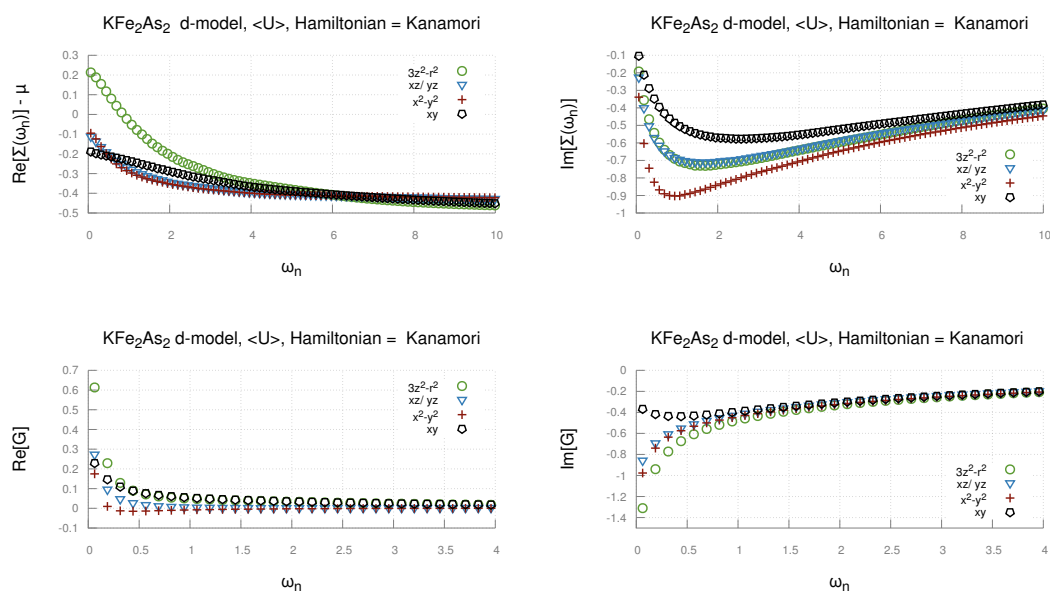


Figure 4.41: DFT+DMFT results of the single-particle properties of KFe_2As_2 in the d -only-model with orbital averaged Coulomb interactions used for a Kanamori-type interaction.

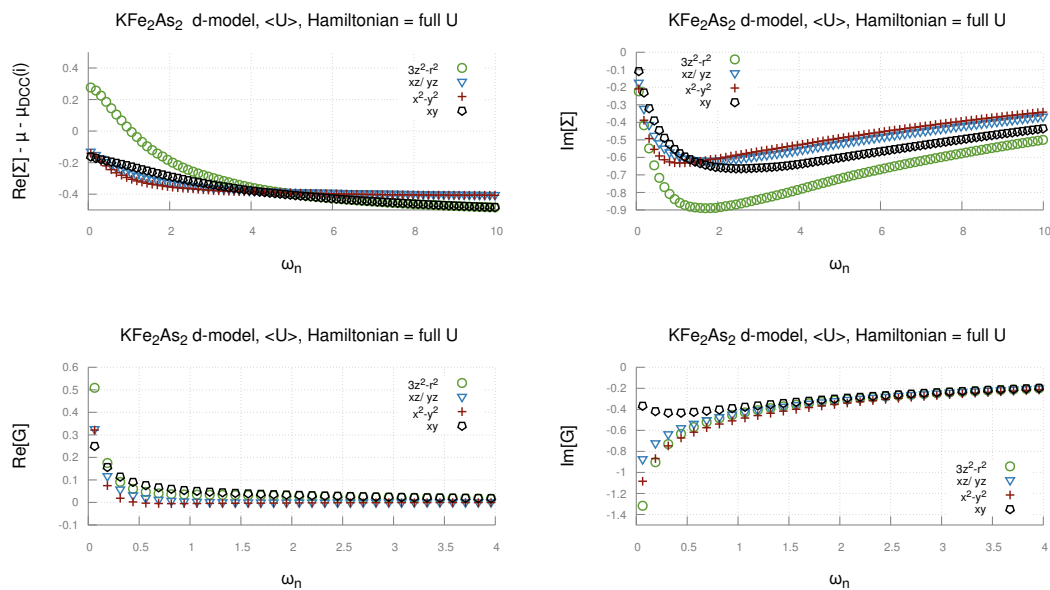


Figure 4.42: DFT+DMFT results for KFe_2As_2 in the d -only-model with "full U" interaction.

Comparing the two cases with orbital-averaged iteration-terms with the orbital-resolved U-term case, we find still a metallic solution, but with changed roles for the different orbitals. In particular the lifetimes- of the quasi-particle excitations of the $3z^2 - r^2$ -orbital have decreased, whereas those of the $x^2 - y^2$ -orbital have increased. The spectral weight at ϵ_F similar between these two cases.

The general trend is in KFe_2As_2 a (bad) metallic character remains, however, with shorter quasi-particle excitation life-times than in the previously analyzed materials.

4.4.2 One-particle-properties in the dpp -model

Fig. 4.43 and Fig. 4.44 show the self-energies and Green's functions in Matsubara frequencies for density-density- as well as for Kanamori interaction. In both cases the U, V and J values were averaged over all orbitals. The two sets of figures show an overall similar behavior. From the imaginary part of the self-energy, one can just deduce a slightly smaller quasi-particle excitation lifetime for the density-density case. The imaginary part of the Green's function is (again) almost exactly on top, regarding these two interaction types. From the real part of the self energy we find the trend that $\text{Re}\Sigma_i^{\text{Kanamori}} \approx \text{Re}\Sigma_i^{\text{Density}} + 0.025\text{eV}$ (for $\omega_n \leq 2\text{eV}$). This means that for a Kanamori-interaction, the orbitals are slightly more shifted to higher energies.

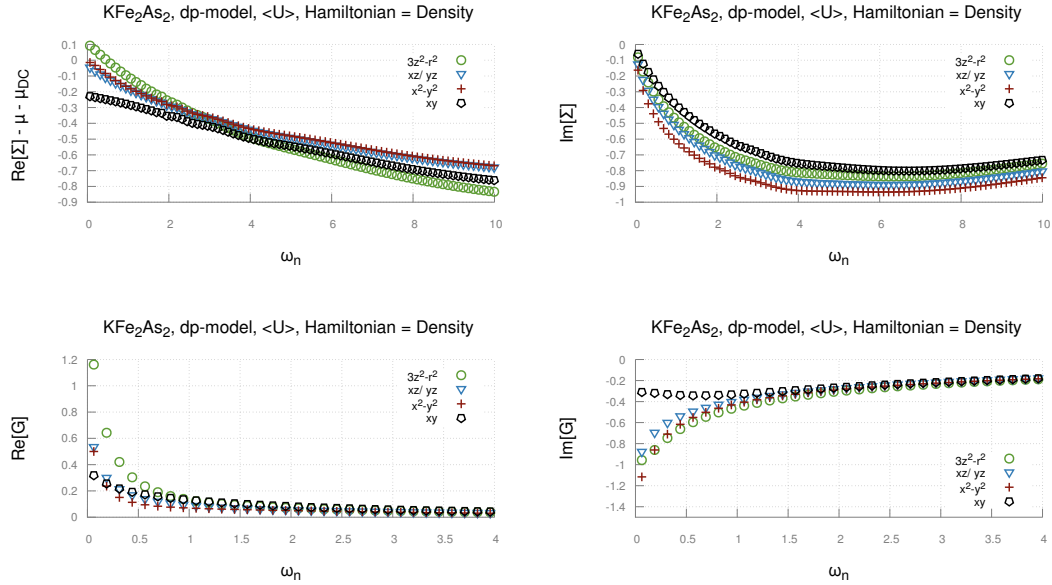


Figure 4.43: DFT+DMFT results of the single-particle properties of KFe_2As_2 , computed for the dp -model with orbital-averaged Coulomb interaction in density-density-type interaction. We used the FLL as DCC.

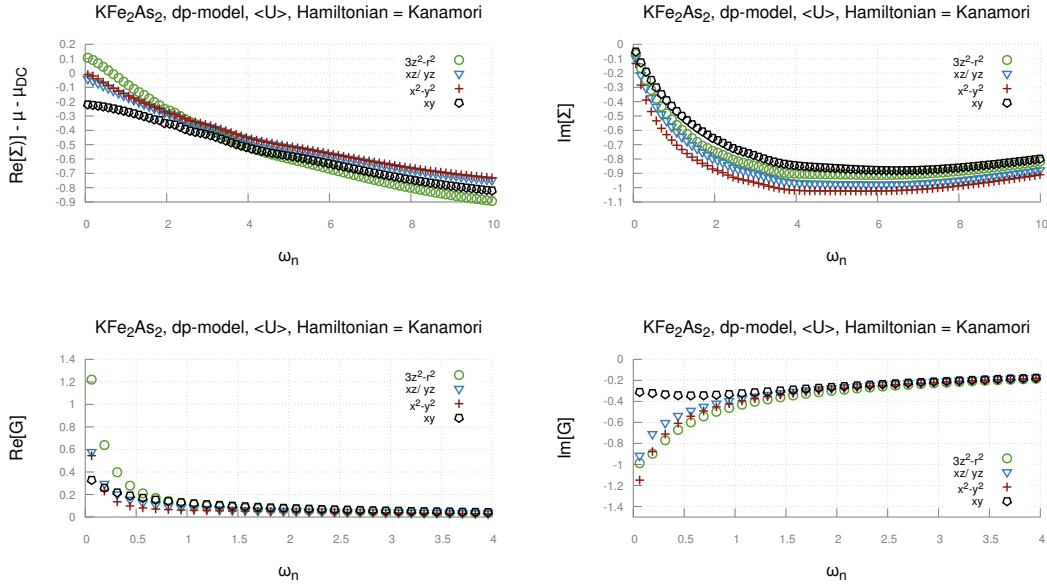


Figure 4.44: DFT+DMFT results of the single-particle properties of KFe_2As_2 , computed for the dp -model with orbital-averaged Coulomb interaction in Kanamori-type-interaction. We used the FLL for the DCC.

The comparison to the d -model full- U case shows a very different picture. It is probably in part also related to the different filling. One can see this for example by comparing the first few Matsubara frequencies of the bottom right figures of Fig. 4.42 to Fig. 4.44. This effect is (again) especially significant for the $3z^2 - r^2$ -orbital (green), which has the largest spectral weight for the full- U case, whereas for the averaged U dpp -model it has a much smaller spectral weight. This is rather due to the choice of model (d - vs dpp -) than due to the orbital-averaged interaction values or H^{int} choice, as can be seen by a comparison to Fig. 4.44 and Fig. 4.43.

4.4.3 Model comparison of the two-particle-properties: Spin-spin susceptibilities

In this subsection we compare the spin-spin-susceptibility χ computed with different models and interaction terms for KFe_2As_2 . We will focus our attention in particular to the difference between the χ^{tot} and χ^{diag} , entirely due to vertex corrections. First, our QMC-data are shown (in imaginary time in Fig. 4.45 and in Matsubara frequencies in Fig. 4.46). Second, the analytically continued data (in real frequencies) will be presented. From these we extracted the different time-scales of the spin-dynamics of the system. Third, we show the Fourier transformed susceptibilities in real frequencies. From the fluctuation-dissipation theorem we also analyzed the symmetric anti-commutator-correlation function $F(t)$, which is better suited to study the quantum-mechanical spin-screening effects.

Susceptibilities in imaginary time/ frequency

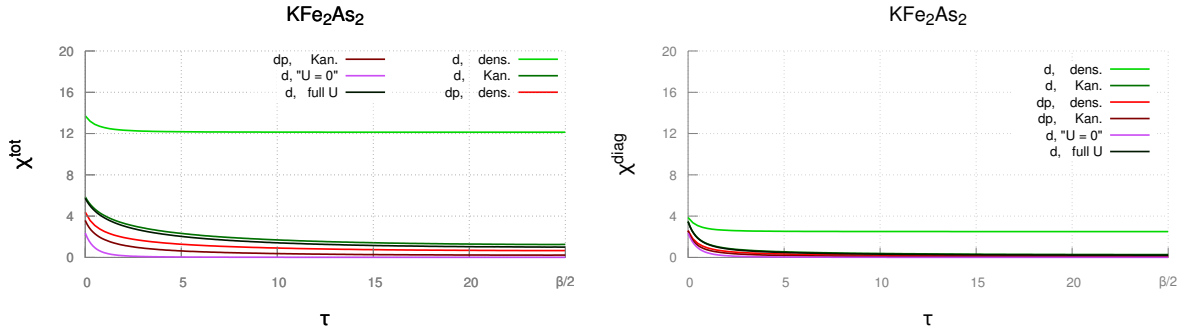


Figure 4.45: KFe_2As_2 : Spin-spin-susceptibility in imaginary time computed for the different models and interaction-types.

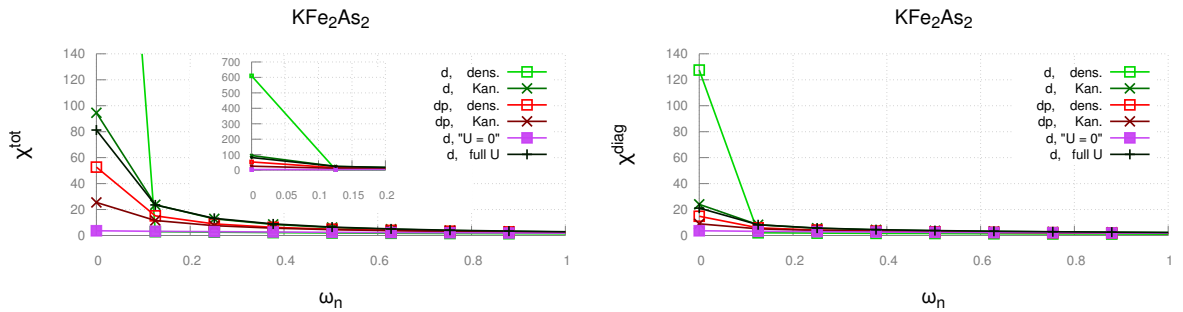


Figure 4.46: KFe_2As_2 : Spin-spin-susceptibility in Matsubara frequencies computed for the different models and interaction-types.

An interesting feature in Fig. 4.45 is that for the d -model the Kanamori-interaction with averaged U -terms gives almost exactly the same results as the d -model with full U interaction. This may be interpreted as a posteriori justification of the averaged procedure, for physical quantities via sums over all orbital-indices. The role of each individual orbital has changed. The density-density d -only case shows very different results than the other cases. Moreover by comparing the left and right sub-figures of Fig. 4.45, we see that, for all cases a significant contribution comes from vertex corrections (with the obvious exception of the $U = 0$ case, where $\chi^{\text{tot}} = \chi^{\text{diag}}$). Furthermore, we find the dp -cases to be closer to the $U = 0$ case. This can be related to the higher filling in the d -manifold. As for an interpretation, one can already qualitatively estimate the significantly increased lifetime of spin-excitations from the QMC-data, one needs to do the analytical continuation to make quantitative predictions (see below).

Susceptibilities in real frequencies

In Fig. 4.47 and in Fig. 4.49 analytically continued spin-spin-susceptibilities via two different methods are shown. To obtain Fig. 4.47 we use the Maximum-Entropy-method (more specifically [40] with an additional selection criterion discussed in section 2.4.3), which is well established. For Fig. 4.49, we have instead used SpM [32].

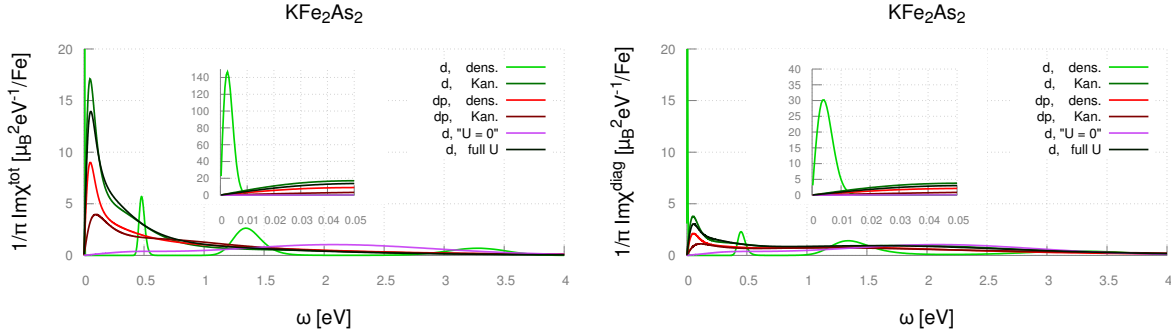


Figure 4.47: KFe_2As_2 : **MaxEnt** Spin-spin-susceptibility in real frequencies computed for the different models and interaction-types.

The non-interacting case (purple) shows a very featureless broad absorption spectrum extended roughly on the whole non-interacting bandwidth. As expected χ^{tot} equals χ^{diag} , since there are no vertex corrections for $U = J = V = 0$. In all the other models and Hamiltonians a low energy peak appears, instead. The position of the peak depends on the choice of the model as well as the Hamiltonian. It ranges from 2.66 meV (d -model dens.-dens. int.) to 138 meV (dpp -model Kan. int.).

The most reliable of the d -model is probably the *full*- U case, for which we used a general orbital-dependent U -matrix as H^{int} . The corresponding spectrum displays a peak-maximum at 62.2 meV. For this case we, fitted the following model spectral function to the data

$$\text{Im}\chi^{\text{tot}}(\omega) = \frac{2a\gamma\omega}{4\gamma^2\omega^2 + (\omega^2 - \omega_0^2)^2}$$

The fit was performed via minimizing the quadratic difference between the model and the data at the data-points. Smaller frequencies were taken more into account⁵.

This allows us to extract model parameters as

	Estimate	Standard Error	t-Statistic	P-Value
a	3.36362	0.12472	26.9694	$1.40 \cdot 10^{-126}$
ω_0	0.35741	0.00649794	55.0036	$9.50 \cdot 10^{-336}$
γ	1.2059	0.0437882	27.5393	$8.19 \cdot 10^{-131}$

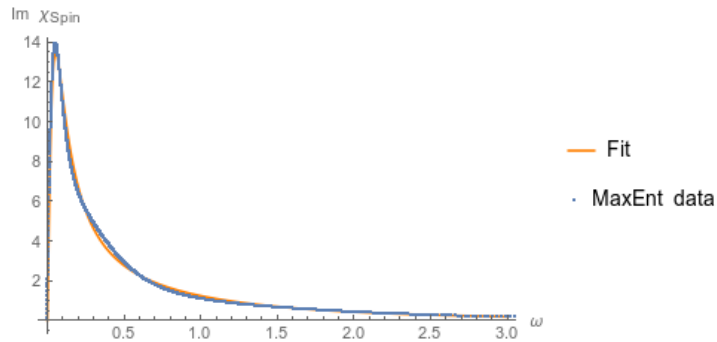


Figure 4.48: KFe_2As_2 : Comparison between the fitted model and the MaxEnt data.

Since the damping-parameter γ is larger than the undamped-frequency ω_0 we are in the overdamped regime. The Fourier-transform of the model reads (in natural units) as

$$\chi^{\text{tot}}(t) = \theta(t) 2.92054 e^{-1.2059t} \sinh(1.15171t).$$

To analyze these life-time estimates more quantitatively we Fourier-transformed the data to real time (under consideration of the KK-relation).

⁵See Ch. 4.1.3 for a justification

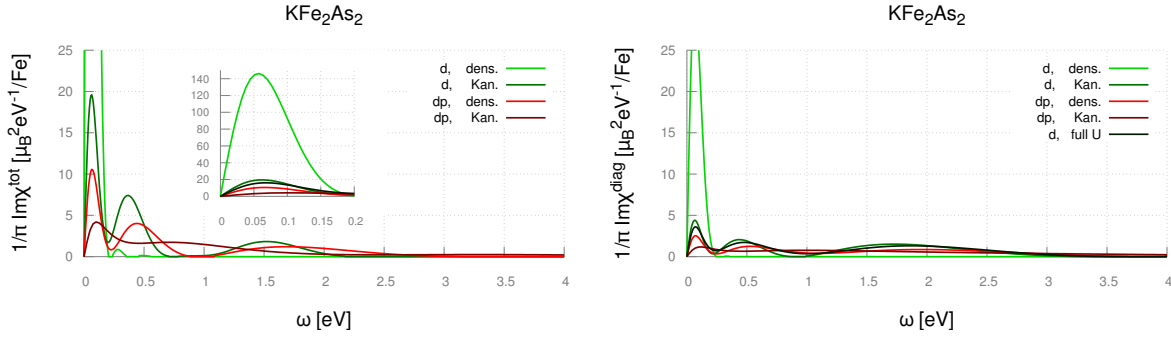


Figure 4.49: KFe_2As_2 : SpM Spin-spin-susceptibility in real frequencies computed for the different models and interaction-types. The results differ considerably from MaxEnt. Especially the low-energy peak. (Formation of local magnetic moment.) A possible reason for this failure is given next to Fig. 2.5

Susceptibilities in real time

The Fourier-transform can be easily carried out and from the fluctuation-dissipation-theorem one can also calculate the anti-commutator-correlator $F(t)$ without any difficulty. The result with restored SI-units are shown in Fig. 4.50 and Fig. 4.51. We only show them for $t > 0$ since $\chi(t)$ is zero for $t < 0$ and $F(t)$ is symmetric with respect to time.

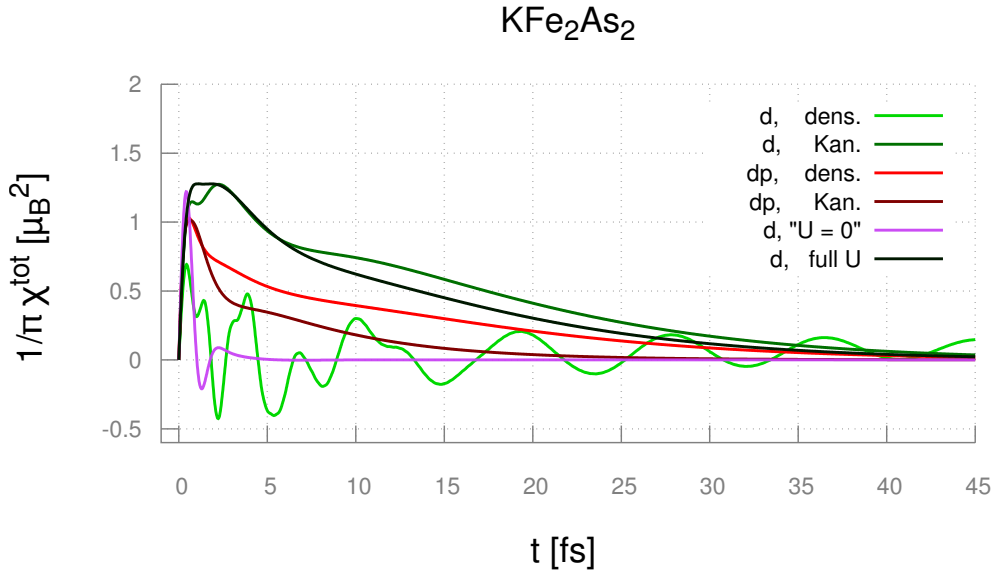


Figure 4.50: KFe_2As_2 Spin-spin-susceptibility in real time computed for different models and interaction-types.

We find $\chi(t)$ to decay on an approximate time-scale of 2 – 15 fs depending upon the choice of model an Hamiltonian. $F(t)$ decays more rapidly on a time-scale of approximately 2 – 5 fs, with the only exception of d -only dens. int. (light green) which has a significantly longer time-scale. (Though this might be a signal of th non-applicability of such an approximation in the paramagnetic phase. See Sec. 5. Comparing this with the model-time-scales (for full U MaxEnt)

$$\begin{aligned} t_\gamma &= \frac{\hbar}{\gamma} = 0.54582 fs \\ t_\omega &= \frac{\hbar}{\sqrt{\omega_0^2 - \gamma^2}} = 0.571507 fs \\ t_{\tilde{\gamma}} &= \frac{\hbar}{\gamma - \omega} = 12.14637 fs, \end{aligned} \quad (4.7)$$

we find an effective damping time-scale of 12.14 fs agreeing well with the black curve in Fig. 4.50.

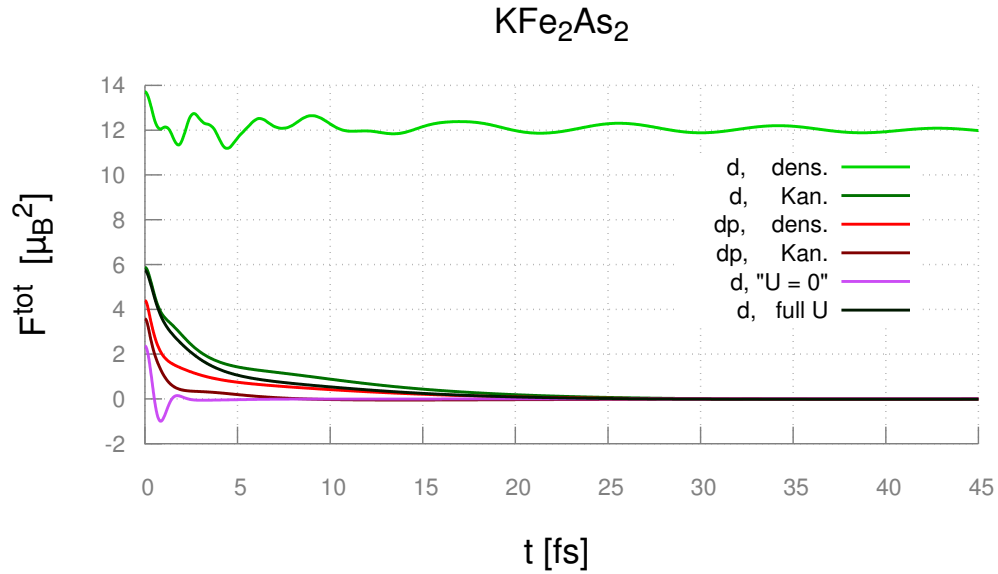


Figure 4.51: FeTe: Spin-spin-anti-commutator correlation function in real time computed for the different models and interaction-types.

Cutoff dependence of the full integral

$$m_{loc,t=0}^2 = \frac{3}{\pi} \lim_{\Omega \rightarrow \infty} \frac{\int_{-\Omega}^{\Omega} \int_{\text{BZ}} \text{Im}\chi(\vec{q}, \omega) b(\omega) d\vec{q} d\omega}{\int_{\text{BZ}} d\vec{q}} = \frac{3}{\pi} \lim_{\Omega \rightarrow \infty} \int_{-\Omega}^{\Omega} \text{Im}\chi(\text{loc}, \omega) b(\omega) d\omega \quad (4.8)$$

In Fig. 4.52 the energy cut-off dependence of the full (square) local magnetic moment is shown. The vertical dotted line marks a experimentally typical energy scale (for INS-measurements) of 100meV. Our results show that only 10% (for dp) to 30% (for d dens.dens int.) of the full local magnetic-moment would be captured by for such a cut-off value. For the full U case (very similar to the d -model Kan. int. case) one would make an 75% error.

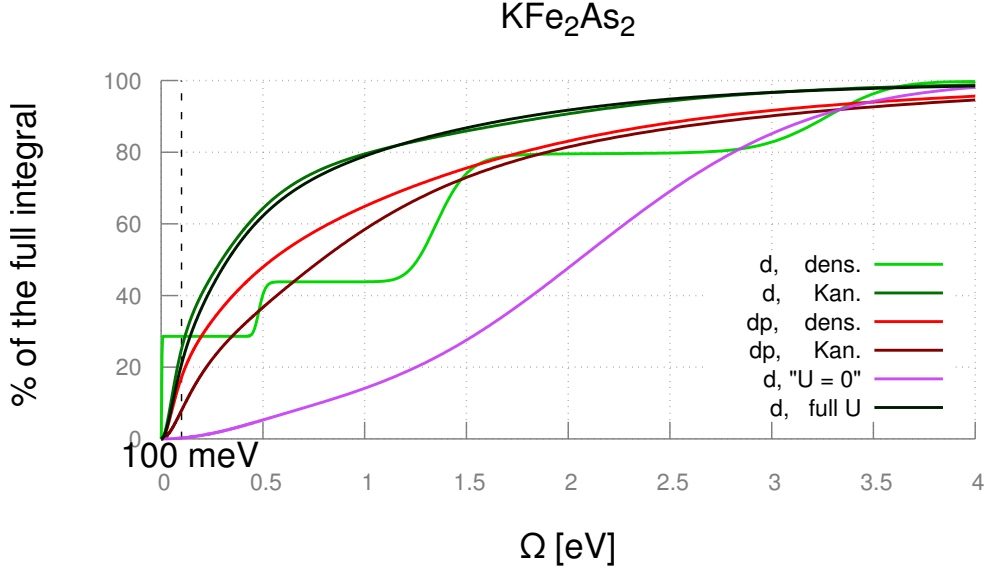


Figure 4.52: KFe_2As_2 : Cutoff dependency (finite Ω) of the squared local magnetic moment estimate $\langle m^2 \rangle$ (full integral in (Eq. 4.8)) computed for the different models and interaction-types.

4.4.4 Occupations and local magnetic momentum

In Tab. 4.7 we report the average occupations and double-occupations with the same spin while in Fig. 4.8 the average double-occupations with different spin are shown. Since we are in the paramagnetic phase the occupations can be deduced via symmetry ($\langle n_{i\uparrow} \rangle = \langle n_{i\downarrow} \rangle$). By comparing the two Tables once can also compute $C_{n_{i\sigma}n_{j\sigma'}} \equiv \langle n_{i\sigma}n_{j\sigma'} \rangle - \langle n_{i\sigma} \rangle \langle n_{j\sigma'} \rangle$ which measures the "degree of correlation".

We find KFe_2As_2 to be more correlated than the previous materials. For example, by analyzing the results for orbital 1 (in full U), which has the largest U value, we get

$$C_{n_{1\uparrow}n_{1\downarrow}} = \langle n_{1\uparrow}n_{1\downarrow} \rangle - \langle n_{1\uparrow} \rangle \langle n_{1\downarrow} \rangle = -0.12$$

This orbital is, the most correlated one (with respect to the same orbital-index). The orbital-dependent role of Hund's exchange, on the other hand, can be estimated by comparing $h_{ij} \equiv \langle n_{i\uparrow}n_{j\uparrow} \rangle - \langle n_{i\uparrow}n_{j\downarrow} \rangle$. Applying this to our Tables (again for the full U case) we get $h_{14} = 0.07$, $h_{12} = h_{13} = h_{24} = h_{34} = 0.06$ whereas all the other $h_{ij} = 0.05$. Thus we conclude that the $3z^2 - r^2$ orbital has the largest Hund's coupling effect, though it is not very different from the other orbitals.

Comparing the occupation numbers with respect to the different models and Hamiltonians (considering the columns) we observe only minor changes with respect to the interaction Hamiltonians, but qualitatively different results with respect to the different Wannier-projections (d vs dp). In fact, this is ascribed to the considerably different filling of the d -manifold: In the d -model the filling of the d -orbital manifold was fixed to 6 electrons on 10 available places, for the dp -model this represents a free parameter. In the later case we have

assumed that the number of electrons of the Wannier basis-set considered the d -manifold together with the two p -manifolds is 12. The reasons for arriving at these numbers were laid out in the previous chapter. It should not be assumed that the dp -results are automatically more valid than the d -ones[33]. We also observe $|\langle n_{i\sigma} \rangle^{\text{den.,d}} - \langle n_{i\sigma} \rangle^{\text{Kan.,d}}| < |\langle n_{i\sigma} n_{j\sigma'} \rangle^{\text{den.,d}} - \langle n_{i\sigma} n_{j\sigma'} \rangle^{\text{Kan.,d}}| \forall \sigma, \sigma' \forall i \neq j$, showing the broken SU(2) symmetry of the density-density interaction.

At the same time, from the disagreement between the d - and the dp -model, one can not answer the question which one is, more or less, correct.

Eventually, the squared local magnetic moment (total as well as diagonal contribution) is shown on the table. ($\chi^{\text{tot}}(\tau = 0)$ and $\chi^{\text{diag}}(\tau = 0)$). A more detailed discussion of this particular result will be given in the next chapter.

	d-model			dpp-model with FLL DCC	
	H_U^D	H_U^K	H_{FLL}^{fullU}	H_U^D	H_U^K
$\langle \mathbf{n}_{1\uparrow} \rangle$	0.58	0.61	0.60	0.78	0.77
$\langle n_{1\uparrow} n_{2\uparrow} \rangle$	0.43	0.34	0.33	0.53	0.52
$\langle n_{1\uparrow} n_{3\uparrow} \rangle$	0.43	0.34	0.33	0.53	0.52
$\langle n_{1\uparrow} n_{4\uparrow} \rangle$	0.45	0.34	0.34	0.53	0.52
$\langle n_{1\uparrow} n_{5\uparrow} \rangle$	0.44	0.38	0.38	0.57	0.56
$\langle \mathbf{n}_{2\uparrow} \rangle$	0.52	0.52	0.52	0.68	0.56
$\langle n_{2\uparrow} n_{3\uparrow} \rangle$	0.40	0.29	0.29	0.47	0.46
$\langle n_{2\uparrow} n_{4\uparrow} \rangle$	0.42	0.29	0.29	0.47	0.46
$\langle n_{2\uparrow} n_{5\uparrow} \rangle$	0.41	0.32	0.33	0.50	0.49
$\langle \mathbf{n}_{3\uparrow} \rangle$	0.52	0.52	0.52	0.68	0.67
$\langle n_{3\uparrow} n_{4\uparrow} \rangle$	0.42	0.29	0.29	0.47	0.46
$\langle n_{3\uparrow} n_{5\uparrow} \rangle$	0.41	0.32	0.33	0.50	0.49
$\langle \mathbf{n}_{4\uparrow} \rangle$	0.51	0.50	0.51	0.67	0.67
$\langle n_{4\uparrow} n_{5\uparrow} \rangle$	0.42	0.32	0.32	0.50	0.49
$\langle \mathbf{n}_{5\uparrow} \rangle$	0.62	0.60	0.60	0.73	0.73
$\sum_{i,\sigma} \langle n_{i,\sigma} \rangle$	5.50	5.50	5.50	7.06	7.04
$\chi^{\text{tot}}(\tau = 0)$	13.72	5.87	5.73	4.40	3.58
$\chi^{\text{diag}}(\tau = 0)$	3.87	3.49	3.47	2.58	2.60

Table 4.7: Comparison of orbital occupations of the *same* spin dependent on the interaction class as well as the model for KFe_2As_2

	d-model			dpp-model with FLL DCC	
	H_U^D	H_U^K	H_{FLL}^{fullU}	H_U^D	H_U^K
$\langle \mathbf{n}_{1\uparrow} \mathbf{n}_{1\downarrow} \rangle$	0.19	0.28	0.24	0.57	0.57
$\langle n_{1\uparrow} n_{2\downarrow} \rangle$	0.16	0.28	0.27	0.50	0.50
$\langle n_{1\uparrow} n_{3\downarrow} \rangle$	0.16	0.28	0.27	0.50	0.50
$\langle n_{1\uparrow} n_{4\downarrow} \rangle$	0.13	0.27	0.27	0.49	0.49
$\langle n_{1\uparrow} n_{5\downarrow} \rangle$	0.26	0.34	0.33	0.55	0.55
$\langle \mathbf{n}_{2\uparrow} \mathbf{n}_{2\downarrow} \rangle$	0.13	0.16	0.17	0.40	0.40
$\langle n_{2\uparrow} n_{3\downarrow} \rangle$	0.14	0.23	0.24	0.42	0.43
$\langle n_{2\uparrow} n_{4\downarrow} \rangle$	0.11	0.22	0.23	0.41	0.42
$\langle n_{2\uparrow} n_{5\downarrow} \rangle$	0.23	0.28	0.28	0.46	0.47
$\langle \mathbf{n}_{3\uparrow} \mathbf{n}_{3\downarrow} \rangle$	0.13	0.16	0.17	0.40	0.40
$\langle n_{3\uparrow} n_{4\downarrow} \rangle$	0.11	0.22	0.23	0.41	0.42
$\langle n_{3\uparrow} n_{5\downarrow} \rangle$	0.23	0.28	0.28	0.46	0.47
$\langle \mathbf{n}_{4\uparrow} \mathbf{n}_{4\downarrow} \rangle$	0.06	0.11	0.15	0.37	0.37
$\langle n_{4\uparrow} n_{5\downarrow} \rangle$	0.21	0.27	0.27	0.46	0.46
$\langle \mathbf{n}_{5\uparrow} \mathbf{n}_{5\downarrow} \rangle$	0.31	0.29	0.29	0.50	0.49

Table 4.8: Comparison of orbital occupations with *different* spin dependent on the interaction class as well as the model for KFe_2As_2

4.5 *FeTe*

4.5.1 One-particle-properties in the *d*-model

In figure 4.53 we show the self-energy as well as the Green's function of *FeTe* for a density-density type interaction in the *d*-model only. Figure 4.54 show the corresponding data for a, full $SU(2)$ symmetric Kanamori-type interaction. In both cases we used the averaged values of the Coulomb-overlap integrals (\bar{U} , \bar{J} and \bar{V}). For the data shown in Figure 4.29 instead this assumption was lifted as we used the full-orbital dependence regarding the interaction terms.

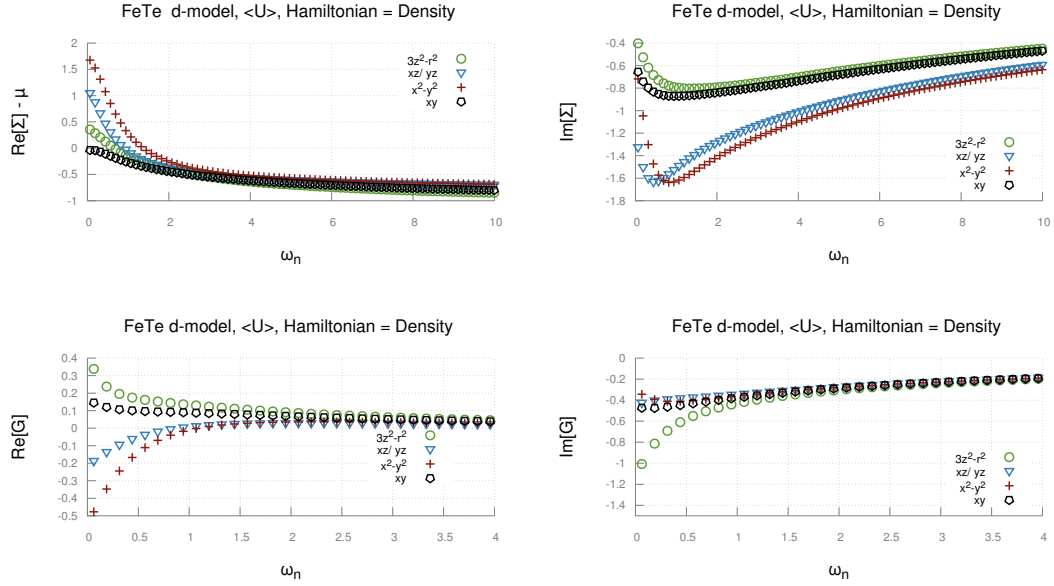


Figure 4.53: DFT+DMFT results of the single-particle properties of *FeTe* in the *d*-only-model with orbital averaged Coulomb interactions used for a density-density-type interaction.

Comparing figure 4.53 with 4.54 we find the inclusion of the full $SU(2)$ symmetry lead to different results. From the $\lim_{i\omega_n \rightarrow 0} \text{Im}\Sigma$ and from $\lim_{i\omega_n \rightarrow 0} \text{Im}G$ we find the Kanamori-case to be more metallic. We moreover observe that $\text{Re}\Sigma^{\text{dens.}} > \text{Re}\Sigma^{\text{Kan.}}$ for *all* orbitals. So dens.-type-int. has shifted all orbitals to higher energies. By extrapolating $\text{Im}G(i\omega_n)$ to $\omega = 0$ shows no definite trend. While the $3z^2 - r^2$ - and the xz/yz -orbitals have more spectral weight at $\omega = 0$ for a dens.-dens- int. that for Kan. int., the $x^2 - y^2$ -orbital has less spectral weight for dens.-dens- int. than for Kan. interaction.

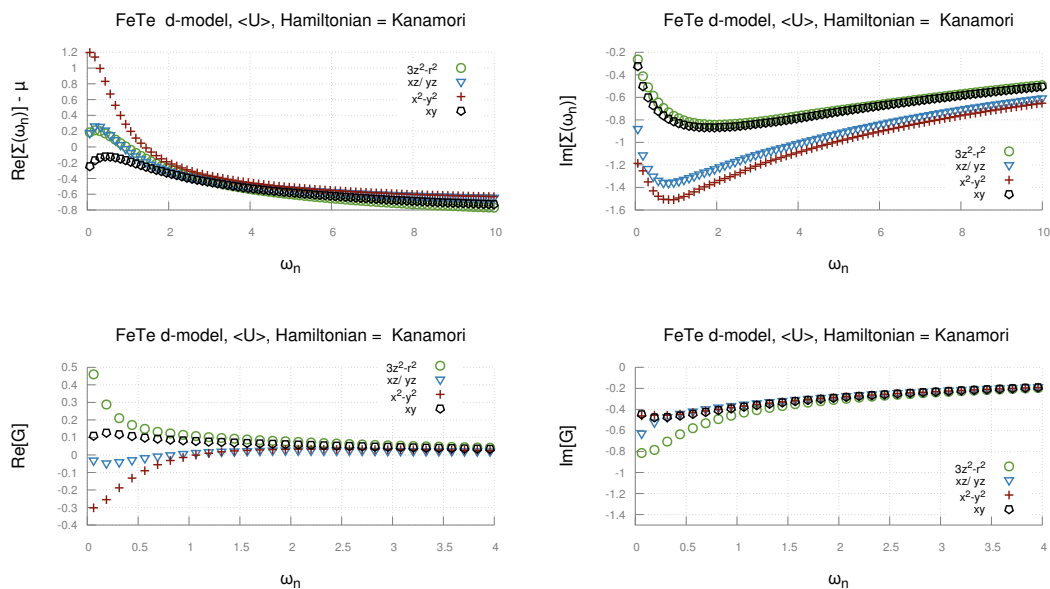


Figure 4.54: DFT+DMFT results of the single-particle properties of $FeTe$ in the d -only-model with orbital averaged Coulomb interactions used for a Kanamori-type interaction.

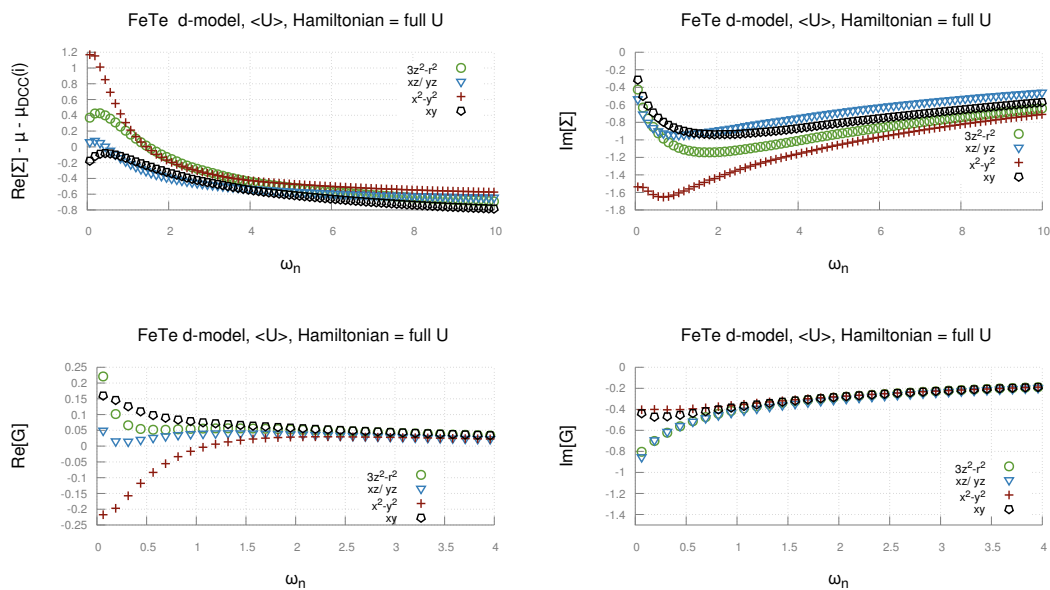


Figure 4.55: DFT+DMFT results for $FeTe$ in the d -only-model with "full U" interaction.

Comparing the two cases with orbital-averaged interaction-terms with the orbital-resolved U-term case we find that the roles of the orbitals have changed significantly. This is especially true $x^2 - y^2$ - and the xz/yz -orbitals. We find $\lim_{i\omega_n \rightarrow 0} \text{Im} \Sigma_{x^2-y^2}^{\text{full U}} < \lim_{i\omega_n \rightarrow 0} \text{Im} \Sigma_{x^2-y^2}^{\text{Kan.}}$, but $\lim_{i\omega_n \rightarrow 0} \text{Im} \Sigma_{xz/yz}^{\text{full U}} > \lim_{i\omega_n \rightarrow 0} \text{Im} \Sigma_{xz/yz}^{\text{Kan.}}$. How this will effect the (total) one-particle spectrum $\mathcal{A}(\omega)$ is not immediately clear. The one-particle spectral function, continued to the real frequency axis via MaxEnt, is given in Chapter 5.

4.5.2 One-particle-properties in the dpp -model

Fig. 4.56 and Fig. 4.57 show the self-energies and Green's functions in Matsubara frequencies for density-density- as well as for Kanamori interaction. In both cases the U, V and J values were averaged over all orbitals.

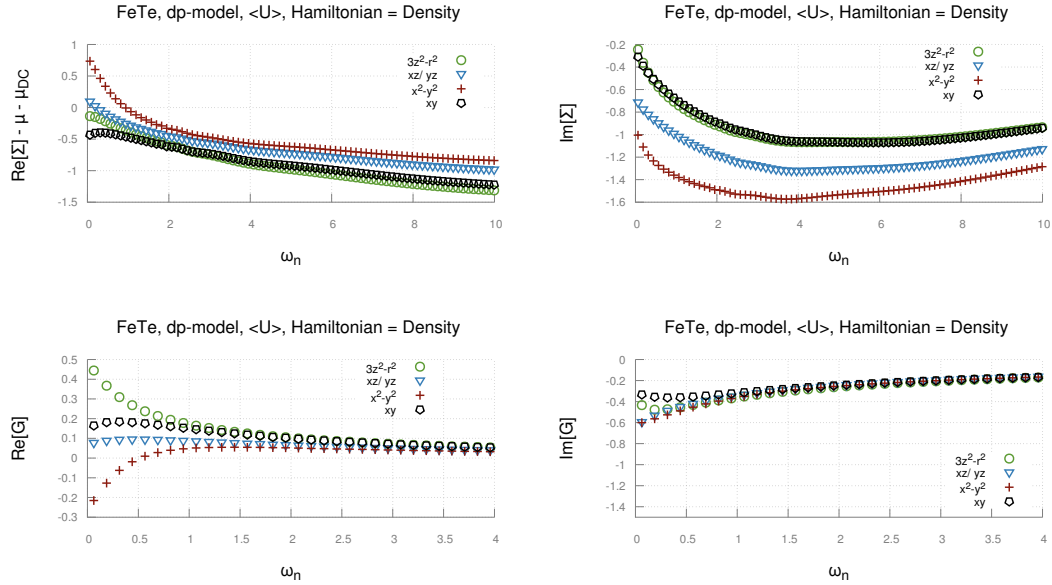


Figure 4.56: DFT+DMFT results of the single-particle properties of $FeTe$, computed for the dp -model with orbital-averaged Coulomb interaction in density-density-type interaction. We used the FLL scheme for the DCC

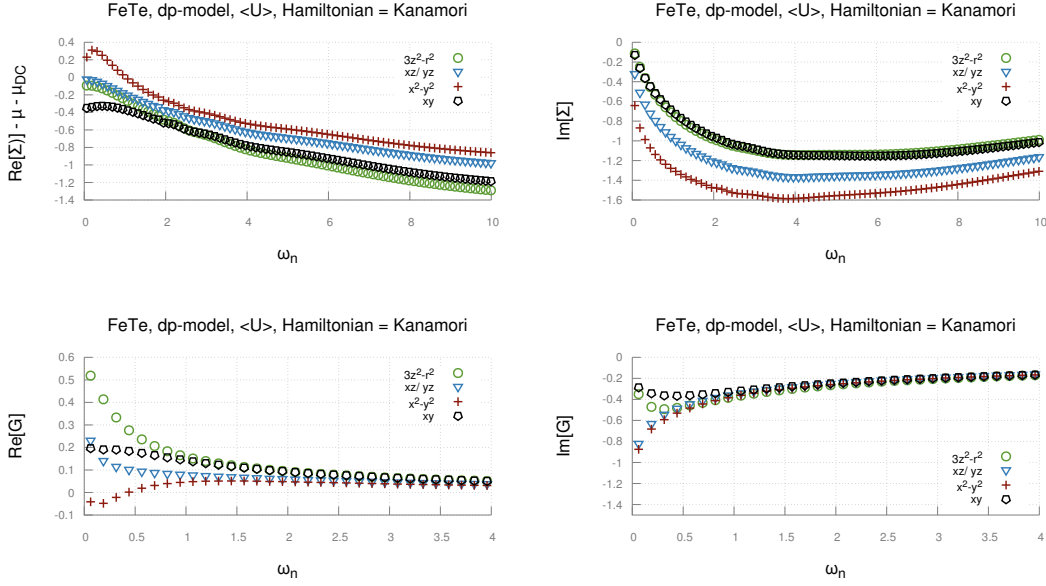


Figure 4.57: DFT+DMFT results of the single-particle properties of $FeTe$, computed for the dp -model with orbital-averaged Coulomb interaction in Kanamori-type interaction. We used the FLL scheme for the DCC.

The two sets of figures show an overall similar behavior. From the imaginary part of the self-energy one can just deduce a smaller quasi-particle excitation lifetime for the density-density case. Moreover the slope of the self-energy is smaller for Kanamori-interaction. The imaginary part of the Green's function shows complementary behavior.

The comparison to the d -model full- U case shows a very different picture. The full U d -model shows smaller quasi-particle excitation lifetime as both dp -cases.

This is probably related to the different filling. Which is exactly 6.00 for the d -only-model, but 7.07 in the dp -model. This is rather due to the choice of model (d - vs dp -) than due to the orbital-averaged interaction values or H^{int} choice, as can be seen by a comparison to Fig. 4.53 and Fig. 4.54.

Qualitatively we find a (bad) metallic behavior for $FeTe$.

4.5.3 Model comparison of the two-particle-properties: Spin-spin susceptibilities

In this subsection we compare the spin-spin-susceptibility χ computed with different models and interaction terms for *FeTe*. We will focus our attention in particular to the difference between the χ^{tot} and χ^{diag} , which is entirely due to vertex corrections. First the QMC-data are shown (in imaginary time in Fig. 4.58 and in Matsubara frequencies in Fig. 4.59). Second, the analytically continued data (in real frequencies) have been computed. From these we have extracted the different time-scales of the spin-dynamics of the system. Third, we show the Fourier transformed susceptibilities in real frequencies. From the fluctuation-dissipation theorem we have also computed the symmetric anti-commutator-correlation function $F(t)$, which is better suited to study the quantum-mechanical spin-screening effects.

Susceptibilities in imaginary time/ frequency

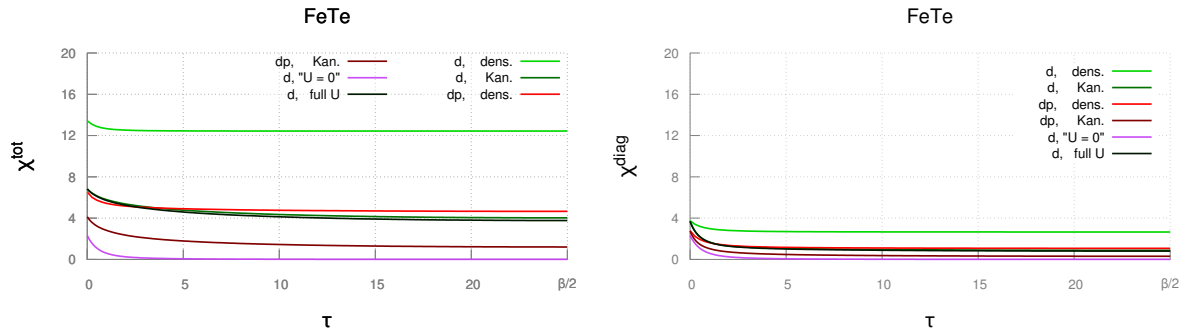


Figure 4.58: FeTe: Spin-spin-susceptibility in imaginary time computed for the different models and interaction-types.

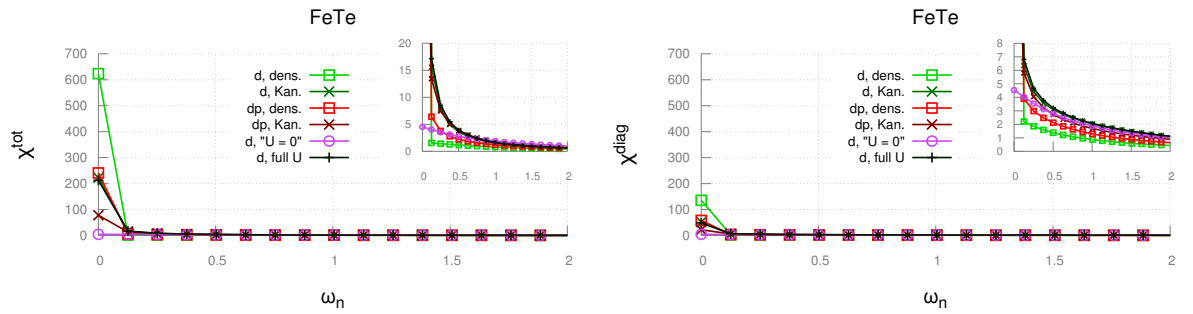


Figure 4.59: FeTe: Spin-spin-susceptibility in Matsubara frequencies computed for the different models and interaction-types.

An interesting feature in Fig. 4.58 is that for the d -model the Kanamori-interaction with averaged U -terms as well as dp -model in dens. int. gives almost exactly the same results as the d -model with full U interaction. The density-density d -only case shows very different results represents an outlier with respect to the other cases. Comparing the left and right sub-figures of Fig. 4.6, we see that for all cases, a significant contribution comes from vertex corrections (with the obvious exception of the $U = 0$ case). As for an interpretation, one can already qualitatively estimate the significantly increased lifetime of spin-excitations from the QMC-data, one needs to do the analytical continuation to make quantitative predictions (see below).

Susceptibilities in real frequencies

In Fig. 4.60 and in Fig. 4.61 analytically continued spin-spin-susceptibilities via two different methods are shown. To obtain Fig. 4.60 we use the Maximum-Entropy-method (more specifically [40] with an additional selection criterion discussed in section 2.4.3). Whereas for Fig. 4.61 used SpM[32].

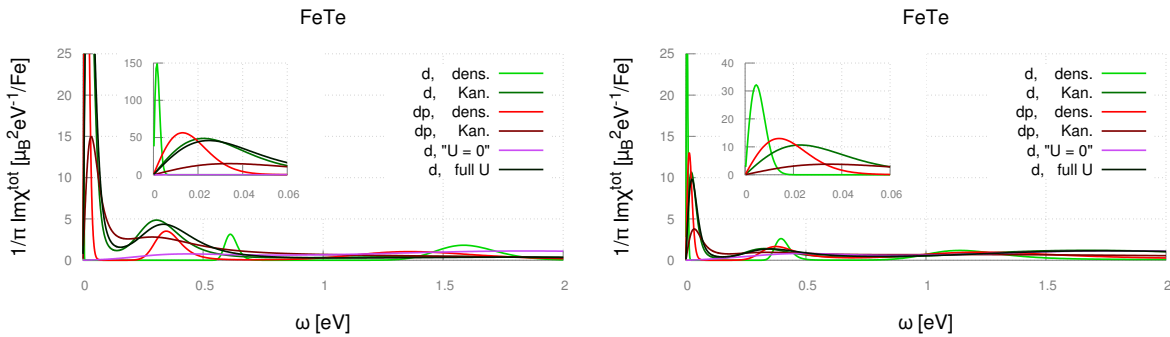


Figure 4.60: FeTe: MaxEnt Spin-spin-susceptibility in real frequencies computed for the different models and interaction-types.

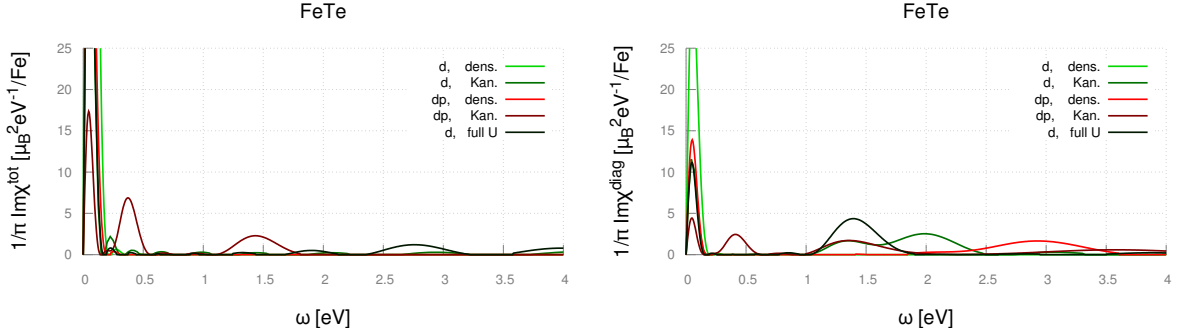


Figure 4.61: FeTe: SpM Spin-spin-susceptibility in real frequencies computed for the different models and interaction-types. The results differ considerably from MaxEnt. Especially the low-energy peak. (Formation of local magnetic moment.) A possible reason for this failure is given next to Fig. 2.5

The non-interacting case (purple) shows a rather featureless broad absorption spectrum extended roughly on the whole non-interacting bandwidth. As expected χ^{tot} equals χ^{diag} , since there are no vertex corrections for $U = J = V = 0$. In all the other models and Hamiltonians a spectral peak-like structure appears at low energies, instead. The position of the first peak depends on the choice of the model as well as the Hamiltonian. It ranges from 1.69 meV (d -model dens. dens. int.) to 34.2 meV (dp -model Kan. int.).

The most reliable of the d -model is probably the *full* - U case, for which we used a general orbital-dependent U -matrix as H^{int} . The corresponding spectrum display their first peak-maxima at 24.4, 322.8 and 1713.4 meV. We tried to fit a three peak model (on the whole MaxEnt-data), but it did not converge. Then we tried a two-peak model of the form

$$\text{Im}\chi^{\text{tot}}(\omega) = \frac{2 a_1 \gamma_1 \omega}{4\gamma_1^2 \omega^2 + (\omega^2 - \omega_{0_1}^2)^2} + \frac{2 a_2 \gamma_2 \omega}{4\gamma_2^2 \omega^2 + (\omega^2 - \omega_{0_2}^2)^2}.$$

For the two-peak model the fitting procedure converged. The fit was performed via minimizing the quadratic difference between the model and the data at the data-points. It is important to remark that the data-points are more dense at smaller energies (due to a Lorentzian energy mesh). This can be justified by the fact that the singular values of the kernel (connecting $\chi(\tau)$ with $\chi(\omega)$) decay fast with respect to the energy. Thus $\chi(\omega)$ is better "supported" by the data at smaller frequencies than at higher frequencies. One should therefore "weigh" $\chi(\omega)$ at smaller frequencies more than at higher frequencies.

This procedure allowed us to extract the model parameters as

If one fits a Single-peak model locally (by truncating the data) to the third peak at around 1.72eV one finds $a_3 = 1.2549$, $\omega_{0_3} = 1.84785$ and $\gamma_3 = 0.835419$. The corresponding timescales are, thus, negligible in comparison to the first two peaks and they will not be further considered here.

	Estimate	Standard Error	t-Statistic	P-Value
a_1	0.0762308	0.000300206	253.928	$9.10 \cdot 10^{-1071}$
a_2	0.36391	0.00548836	66.3058	$7.34 \cdot 10^{-410}$
ω_{01}	0.0347013	0.0000569195	609.656	$7.91 \cdot 10^{-1538}$
ω_{02}	0.357901	0.0013751	260.272	$8.43 \cdot 10^{-1084}$
γ_1	0.0274941	0.000120823	227.558	$5.23 \cdot 10^{-1013}$
γ_2	0.11116	0.00207659	53.5299	$1.51 \cdot 10^{-324}$

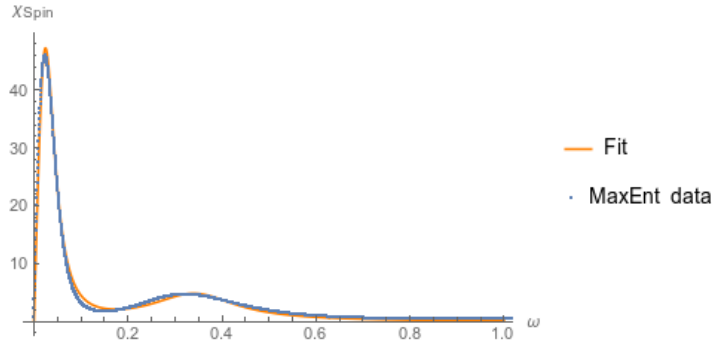


Figure 4.62: *FETE*: Comparison between the fitted model and the MaxEnt data.

Since both damping-parameters γ_i ($i=1,2$) are smaller than their corresponding undamped-frequencies ω_{0i} we are in the underdamped regime. The Fourier-transform of the model reads (in natural units) as

$$\chi^{\text{tot}}(t) = \theta(t) \left(3.60055 e^{-0.0274941t} \sin(0.021172t) + 1.06969 e^{-0.11116t} \sin(0.3402t) \right).$$

To improve the discussion of our life-time estimates we performed the numerical Fourier-transform to real time (under consideration of the KK-relation). (See below)

Susceptibilities in real time

The Fourier-transform can be easily carried out and from the fluctuation-dissipation-theorem one can also calculate the anti-commutator-correlator $F(t)$ without any difficulty. The result with restored SI-units are shown in Fig. 4.63 and Fig. 4.64. We only show them for $t > 0$ since $\chi(t)$ is zero for $t < 0$ and $F(t)$ is symmetric with respect to time.

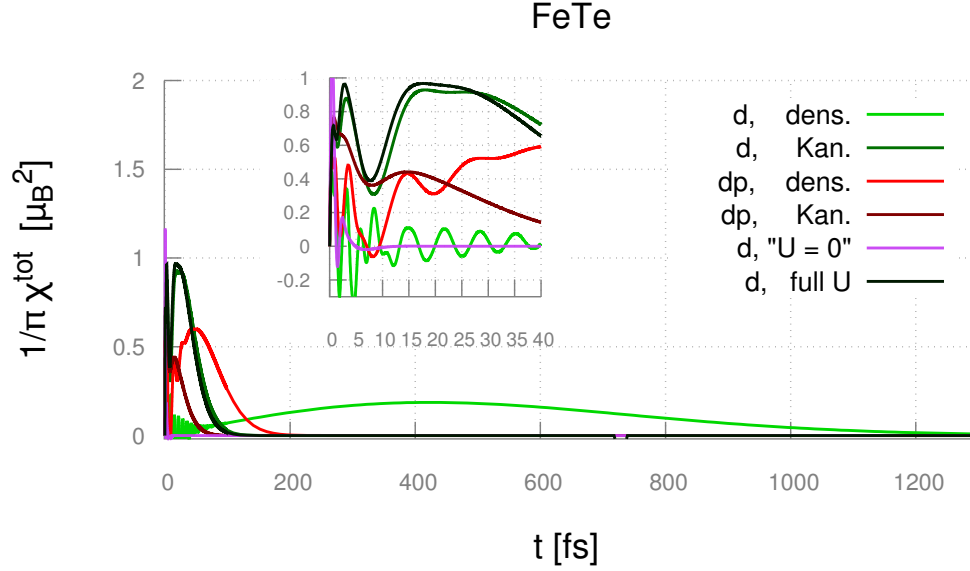


Figure 4.63: FeTe: Spin-spin-susceptibility in real time computed for the different models and interaction-types.

We find $\chi(t)$ the numerical data in Fig.4.63 to decay for full U on an approximate time-scale of 50 fs. This is in disagreement with the fitted model. Where the damping-timescale is 23.9 fs. Comparing the fitted model we see that the fit slightly overestimates the width, and thus underestimates the time-scale. A possible reason might be that first peak in the data actually consists of several (narrow) peaks, which can not be resolved. Several narrow peaks would lead longer life-times. Another (related) explanation would be that the harmonic oscillator model is not ideal for *FeTe*.

Both Kanamori and full U show similar lifetimes. For the d -only, dens. int. we find a lifetime of almost 1ns, which is very different to the other cases. The strong oscillations at the beginning originate from the second peak. Transforming the model-parameters into life-times

$$\begin{aligned}
 t_{\gamma_1} &= \frac{\hbar}{\gamma} = 23.9401 fs \\
 t_{\omega_1} &= \frac{\hbar}{\sqrt{\omega_{01}^2 - \gamma_1^2}} = 31.0888 fs \\
 t_{\gamma_2} &= \frac{\hbar}{\gamma_2} = 5.92131 fs \\
 t_{\omega_2} &= \frac{\hbar}{\sqrt{\omega_{02}^2 - \gamma_2^2}} = 1.93478 fs,
 \end{aligned} \tag{4.9}$$

we find $t_{\gamma_1} < t_{\omega_1}$, but $t_{\gamma_2} > t_{\omega_2}$. The first peak dominates (in the model) for timescales larger than 6 fs. This fact is in agreement with the data. The first peak, however, was not ideally captured by the model.

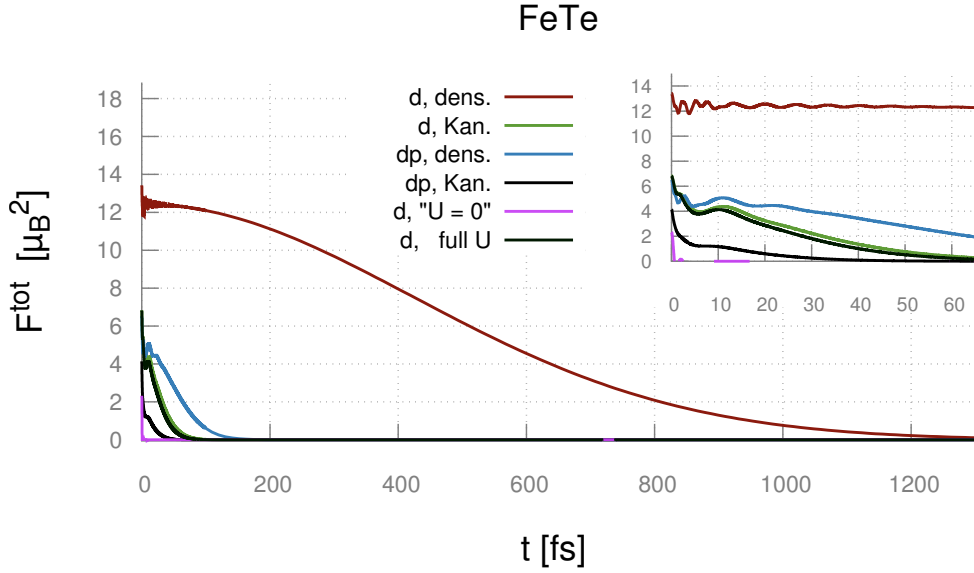


Figure 4.64: FeTe: Spin-spin-anti-commutator correlation function in real time computed for the different models and interaction-types.

Cutoff dependence of the full integral

$$m_{\text{loc},t=0}^2 = \frac{3}{\pi} \lim_{\Omega \rightarrow \infty} \frac{\int_{-\Omega}^{\Omega} \int_{\text{BZ}} \text{Im}\chi(\vec{q}, \omega) b(\omega) d\vec{q} d\omega}{\int_{\text{BZ}} d\vec{q}} = \frac{3}{\pi} \lim_{\Omega \rightarrow \infty} \int_{-\Omega}^{\Omega} \text{Im}\chi(\text{loc}, \omega) b(\omega) d\omega \quad (4.10)$$

In Fig. 4.65 the energy cut-off dependence of the full (square) local magnetic moment is shown. The vertical dotted line marks a experimentally typical energy scale (for INS-measurements) of 100meV. Our results show that only 30% (for *dp* Kan.) to 50% (for *d* Kan. int.) of the full local magnetic-moment would show for such a cut-off value. For the full *U* case (very similar to the *d*-model Kan. int. case) one would make an 50% error, i.e. lower than in all other cases.

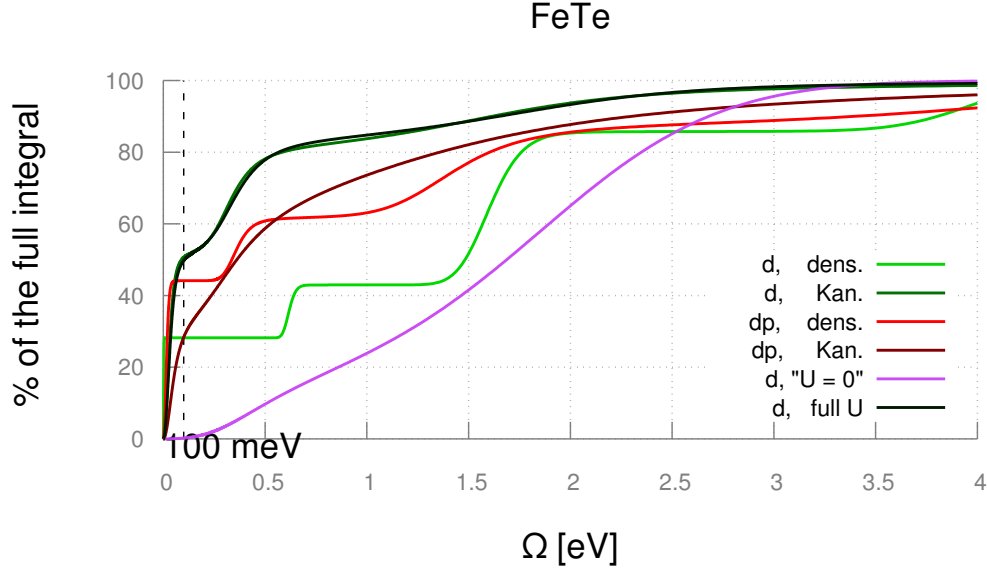


Figure 4.65: FeTe: Cutoff dependency (finite Ω) of the squared local magnetic moment estimate $\langle m^2 \rangle$ (full integral in (Eq. 4.10)) computed for the different models and interaction-types.

4.5.4 Occupations and local magnetic momentum

In Tab. 4.9 we report the average occupations and double-occupations with the same spin while in Fig.4.10 the average double-occupations with different spin are shown. Since we are in the paramagnetic phase the occupations can be deduced via symmetry ($\langle n_{i\uparrow} \rangle = \langle n_{i\downarrow} \rangle$). By comparing the two Tables once can also compute $C_{n_{i\sigma}n_{j\sigma'}} \equiv \langle n_{i\sigma}n_{j\sigma'} \rangle - \langle n_{i\sigma} \rangle \langle n_{j\sigma'} \rangle$ which measures the "degree of correlation".

We find FeTe to be the most correlated material. For example, by analyzing the results for orbital 4 (in full U), which has the largest U value, we get

$$C_{n_{4\uparrow}n_{4\downarrow}} = \langle n_{4\uparrow}n_{4\downarrow} \rangle - \langle n_{4\uparrow} \rangle \langle n_{4\downarrow} \rangle = -0.2016$$

This orbital $x^2 - y^2$ is the most correlated. The orbital-dependent role of Hund's exchange, on the other hand, can be estimated by comparing $h_{ij} \equiv \langle n_{i\uparrow}n_{j\uparrow} \rangle - \langle n_{i\uparrow}n_{j\downarrow} \rangle$. Applying this to our Tables (again for the full U case) we get $h_{24} = h_{24} = 0.1$, $h_{25} = 0.09$, $h_{23} = h_{45} = 0.08$, $h_{12} = h_{13} = 0.07$ and $h_{15} = h_{25} = h_{35} = 0.06$.

Comparing the occupation numbers with respect to the different models and Hamiltonians (considering the columns) we observe only minor changes with respect to the interaction Hamiltonians, but qualitatively different results with respect to the different Wannier-projections (d vs dp). In fact, this is ascribed to the considerably different filling of the d -manifold: In the d -model the filling of the d -orbital manifold was fixed to 6 electrons on 10 available places, for the dp -model this represents a free parameter. In the later case we have assumed that the number of electrons of the Wannier basis-set considered the d -manifold together with the two p -manifolds is 12. The reasons for arriving at these numbers were

laid out in the previous chapter. It should not be assumed that the dp -results are automatically more valid than the d -ones[33]. We also observe $|\langle n_{i\sigma} \rangle^{\text{den.,d}} - \langle n_{i\sigma} \rangle^{\text{Kan.,d}}| < |\langle n_{i\sigma} n_{j\sigma'} \rangle^{\text{den.,d}} - \langle n_{i\sigma} n_{j\sigma'} \rangle^{\text{Kan.,d}}| \forall \sigma, \sigma' \forall i \neq j$, showing the broken SU(2) symmetry of the density-density interaction.

At the same time, from the disagreement between the d - and the dp -model, one can not answer the question which one is, more or less, correct.

Eventually, the squared local magnetic moment (total as well as diagonal contribution) is shown on the table. ($\chi^{\text{tot}}(\tau = 0)$ and $\chi^{\text{diag}}(\tau = 0)$). A more detailed discussion of this particular result will be given in the next chapter.

	d-model			dpp-model with FLL DCC	
	H_U^D	H_U^K	H_{FLL}^{fullU}	H_U^D	H_U^K
$\langle \mathbf{n}_{1\uparrow} \rangle$	0.72	0.71	0.64	0.80	0.80
$\langle n_{1\uparrow} n_{2\uparrow} \rangle$	0.48	0.41	0.40	0.56	0.54
$\langle n_{1\uparrow} n_{3\uparrow} \rangle$	0.48	0.42	0.40	0.56	0.54
$\langle n_{1\uparrow} n_{4\uparrow} \rangle$	0.48	0.41	0.39	0.53	0.51
$\langle n_{1\uparrow} n_{5\uparrow} \rangle$	0.52	0.47	0.45	0.62	0.60
$\langle \mathbf{n}_{2\uparrow} \rangle$	0.54	0.55	0.58	0.67	0.68
$\langle n_{2\uparrow} n_{3\uparrow} \rangle$	0.46	0.35	0.37	0.51	0.47
$\langle n_{2\uparrow} n_{4\uparrow} \rangle$	0.47	0.35	0.36	0.50	0.44
$\langle n_{2\uparrow} n_{5\uparrow} \rangle$	0.46	0.39	0.40	0.54	0.52
$\langle \mathbf{n}_{3\uparrow} \rangle$	0.54	0.55	0.58	0.67	0.68
$\langle n_{3\uparrow} n_{4\uparrow} \rangle$	0.47	0.35	0.36	0.50	0.44
$\langle n_{3\uparrow} n_{5\uparrow} \rangle$	0.46	0.39	0.41	0.54	0.52
$\langle \mathbf{n}_{4\uparrow} \rangle$	0.53	0.54	0.54	0.61	0.62
$\langle n_{4\uparrow} n_{5\uparrow} \rangle$	0.46	0.39	0.39	0.51	0.48
$\langle \mathbf{n}_{5\uparrow} \rangle$	0.67	0.66	0.66	0.77	0.76
$\sum_{i,\sigma} \langle n_{i,\sigma} \rangle$	6.00	6.00	6.00	7.07	7.07
$\chi^{\text{tot}}(\tau = 0)$	13.43	6.86	6.83	6.53	4.15
$\chi^{\text{diag}}(\tau = 0)$	3.75	3.70	3.69	2.77	2.74

Table 4.9: Comparison of orbital occupations of the *same* spin dependent on the interaction class as well as the model for $FeTe$

	d-model			dpp-model with FLL DCC	
	H_U^D	H_U^K	H_{FLL}^{fullU}	H_U^D	H_U^K
$\langle \mathbf{n}_{1\uparrow} \mathbf{n}_{1\downarrow} \rangle$	0.46	0.44	0.31	0.62	0.61
$\langle n_{1\uparrow} n_{2\downarrow} \rangle$	0.29	0.35	0.33	0.50	0.52
$\langle n_{1\uparrow} n_{3\downarrow} \rangle$	0.29	0.35	0.33	0.50	0.52
$\langle n_{1\uparrow} n_{4\downarrow} \rangle$	0.27	0.34	0.30	0.44	0.47
$\langle n_{1\uparrow} n_{5\downarrow} \rangle$	0.42	0.43	0.39	0.59	0.59
$\langle \mathbf{n}_{2\uparrow} \mathbf{n}_{2\downarrow} \rangle$	0.12	0.14	0.20	0.37	0.38
$\langle n_{2\uparrow} n_{3\downarrow} \rangle$	0.12	0.25	0.29	0.38	0.42
$\langle n_{2\uparrow} n_{4\downarrow} \rangle$	0.10	0.23	0.26	0.32	0.38
$\langle n_{2\uparrow} n_{5\downarrow} \rangle$	0.25	0.32	0.34	0.47	0.49
$\langle \mathbf{n}_{3\uparrow} \mathbf{n}_{3\downarrow} \rangle$	0.12	0.14	0.21	0.37	0.38
$\langle n_{3\uparrow} n_{4\downarrow} \rangle$	0.10	0.23	0.26	0.32	0.38
$\langle n_{3\uparrow} n_{5\downarrow} \rangle$	0.25	0.32	0.35	0.47	0.49
$\langle \mathbf{n}_{4\uparrow} \mathbf{n}_{4\downarrow} \rangle$	0.06	0.09	0.09	0.24	0.26
$\langle n_{4\uparrow} n_{5\downarrow} \rangle$	0.23	0.31	0.31	0.41	0.45
$\langle \mathbf{n}_{5\uparrow} \mathbf{n}_{5\downarrow} \rangle$	0.37	0.35	0.35	0.55	0.54

Table 4.10: Comparison of orbital occupations with *different* spin dependent on the interaction class as well as the model for $FeTe$

Chapter 5

Results: Comparison and discussion of Materials and Models

This chapter is devoted to an overall comparison of the one- and two-particle spectral properties obtained for the different families of Fe-based superconductors and to the discussion of the role played by the local magnetic moment in the different case. In particular, we will first show the one-particle spectral-functions of the materials under consideration before moving on to the spin-spin-correlation functions, whose investigation represents the main focus of this thesis. In this respect, our findings confirm the expectations for the trend of spin absorption spectra (in the different families, responsible for the mismatch between earlier LSDA calculations and experiments)

More in details we start by showing the spin susceptibility in imaginary time, the direct output of our QMC calculations. Then, we illustrate our analytical continuation-results (on the real frequency axis) and, finally, we transform our results to real-time. These will allow us to analyze the quantum-dynamical screening effect (and there respective time-scales) providing a deeper insights into the different local magnetic moments of these materials.

Spectral function Fig. 5.1 shows the DFT+DMFT spectral function on the real frequency-axis. The contributions of all (analytically continued) orbitals were summed up. Each sub-plot shows one model-/ Hamiltonian-case. For the $dp - /dpp$ -model the spectral function for Kanamori and for density-density- interaction agree well with one another for all materials except FeTe (sub-figures at the bottom). For FeTe, which is the most correlated of the materials, we find a small peak at $\omega = 0$ for Kanamori, which was missing in the density-density case. This would support the approximation of using a density-density- interaction for all materials in the $dp - /dpp$ -model except FeTe. In the d -model the situation is quite different. For averaged interaction terms with a Kanamori-interaction all materials show a spectral-peak slightly below the Fermi-level. The size of the peak decreases for larger U -values. This is in contrast to the density-density case (mid left subfigure) where the spectral functions are almost structureless in this region (except for LaFeAsO where the two interaction cases still agree reasonably well). We observe that the choice of H^{int} changes the result significantly for the d -model. In the *full* U case the structures in the spectral function are more pronounced. This is partially due to the different MaxEnt-selection criteria we applied. For *full* U we used *Bryan's* MaxEnt (Averaging over all spectra, weighed by their posteriori probability). For the other cases we used the Kink-selection criteria discussed in section 2.4.3 . The later smears out the spectral function and is responsible for the loss of the sharp energy-features. However, we find large differences to severe to be ascribed as a mere fact of the MaxEnt selection criteria. For example, while the peaks below the Fermi-level are present for Kanamori- as well as for *full* U -interaction, their magnitudes and their positions are quite different. This difference is especially surprising in comparison to the similarity of the corresponding spin-spin-correlation function. (See next paragraph.)

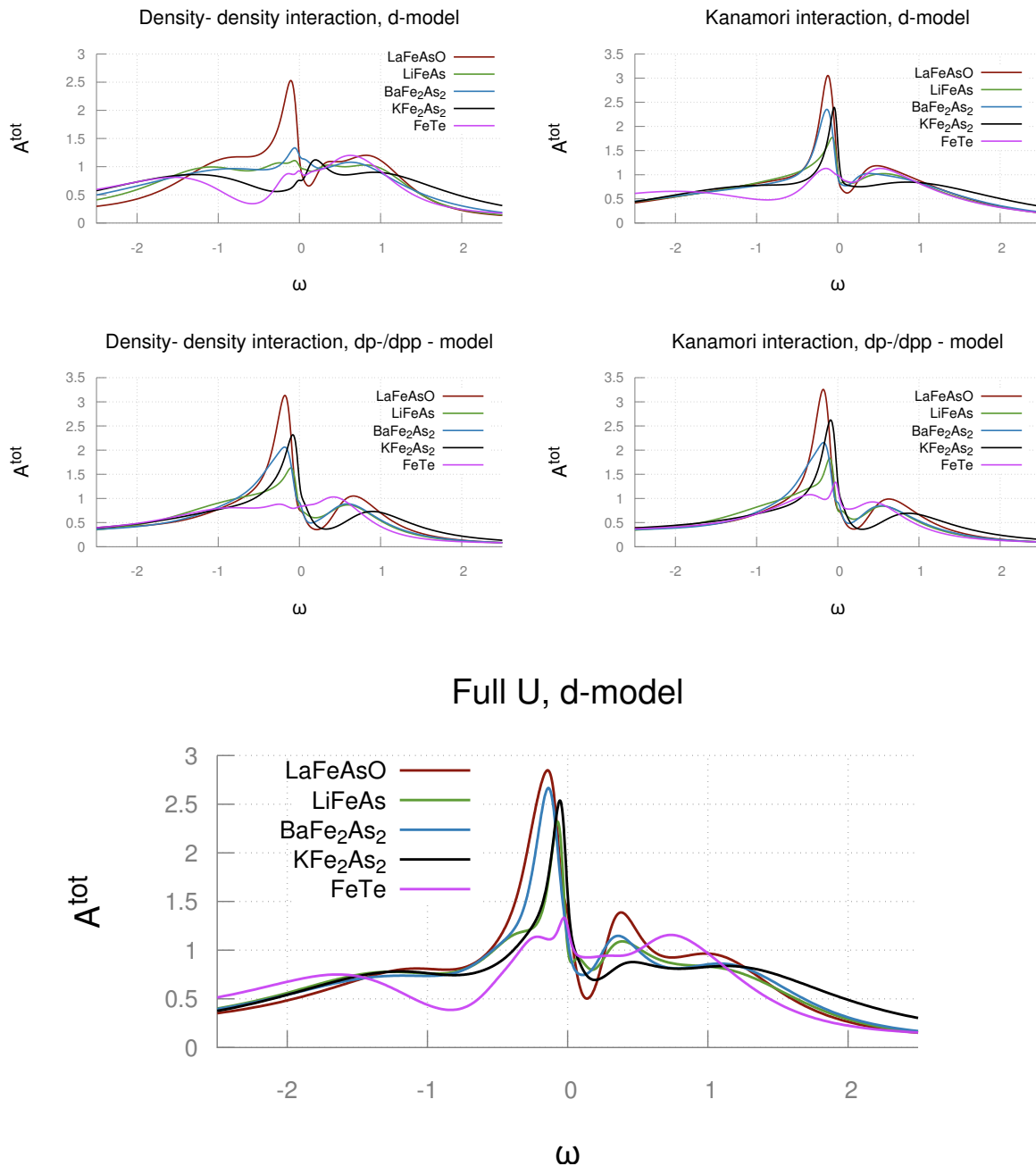


Figure 5.1: Comparison of the spectral functions on the real frequency-axis for the different materials considered. The analytical continuation of the QMC data has been performed with MaxEnt.

In Fig. 5.2 the orbital-resolved DFT+DMFT spectral function for the *full* $-U$ is shown in

comparison to the DFT-DOS. The DFT+DMFT results (shown as solid lines) were obtained with Bryan's MaxEnt [40] whereas the DFT+DMFT DOS was extracted directly from the DFT dispersion relation. As expected the DMFT-calculation changed the d -orbitals quite considerably. While this trend is found for all materials it is especially pronounced for FeTe (bottom right subfigure), which can be regarded, in fact, as the most correlated one. More specifically we find that spectral weight at $\omega = \epsilon_F = 0$ of the xy -orbital for all materials except FeTe to be almost negligible in comparison to the other orbitals. The others all display a peak with its maximum slightly below the Fermi-energy. Further for all materials except FeTe the $3z^2 - r^2$ orbital yields the largest contribution to this peak. (The spectral weight at the Fermi-level is, however, not necessarily dominated by this peak.)

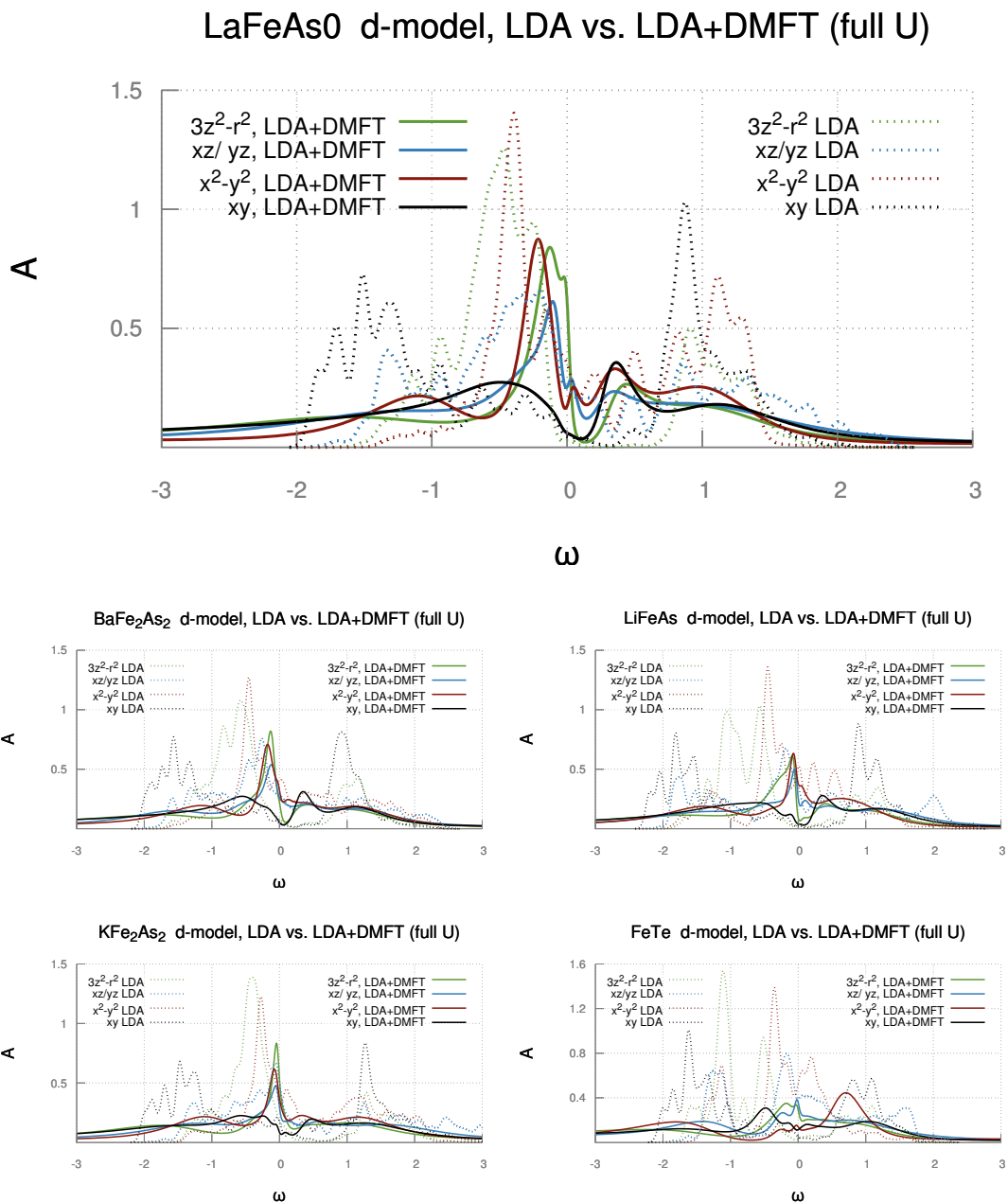


Figure 5.2: Comparison of the orbital-resolved spectral function on the real frequency-axis for the different materials. The plots show beside the d -model in $full U$ (solid lines) also the corresponding DFT-results in the corresponding Wannier basis (dashed lines).

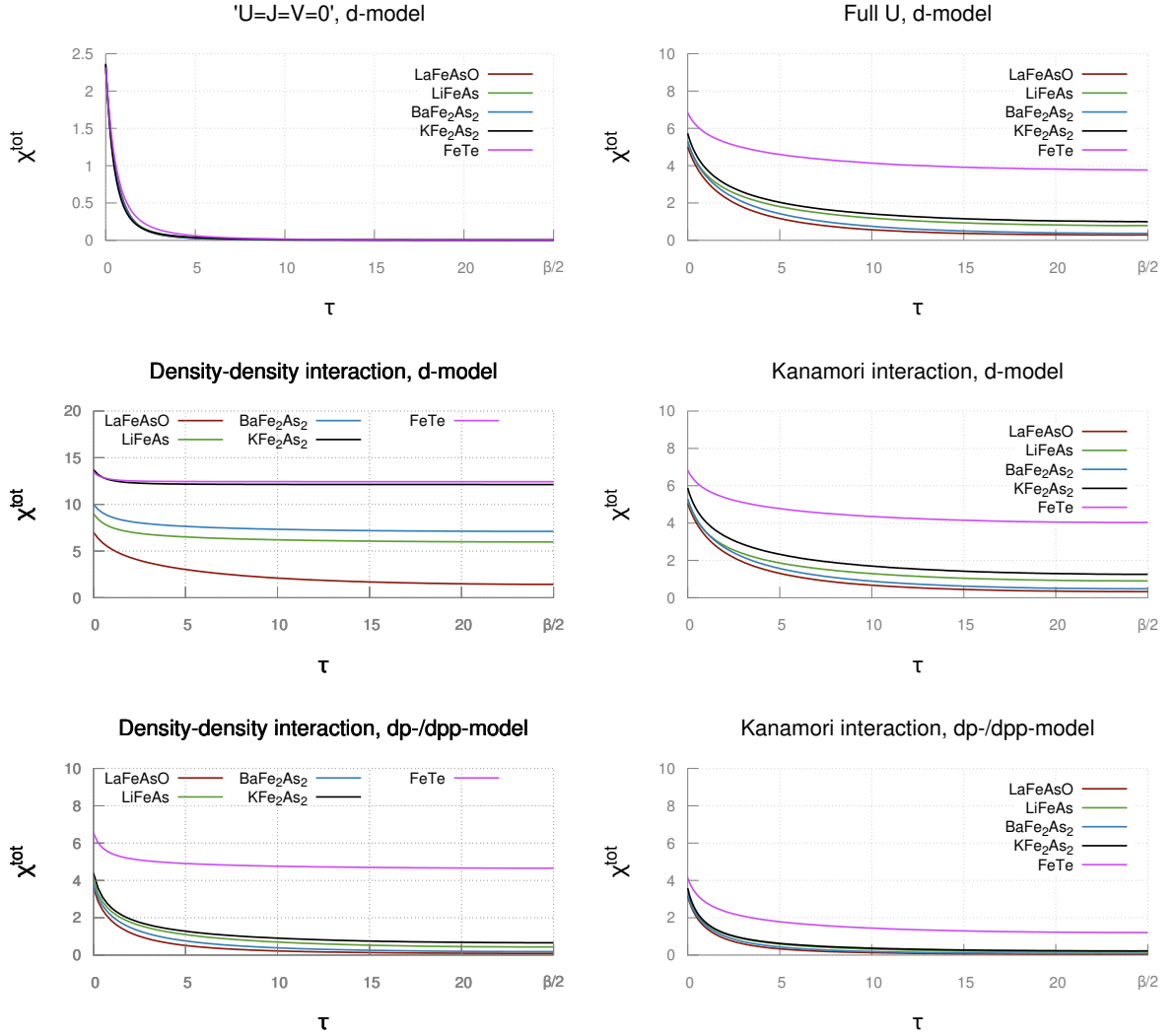


Figure 5.3: Comparison of the total spin-spin-susceptibility in imaginary time for the different materials considered. Note the different scales for "U=0" (top-left figure) and "Density-density, d-model" (mid-left figure).

Spin-spin-susceptibility In Fig. 5.3 the total spin-spin-susceptibility in imaginary time is shown. Fig. 5.4 shows the diagonal-contribution as a comparison. The "U=J=V=0" case shows a rapid decay of $\chi(\tau)$ (almost) independent of the material. The total contribution equals the diagonal contribution due to the absence of vertex corrections for $U = 0$. For the other five cases, where the rRPA results were used for the interaction terms, we find qualitatively an ordering of (the shape of the) curves as

$$\frac{\chi^{\text{FeTe}}(\tau)}{\chi^{\text{FeTe}}(0)} > \frac{\chi^{\text{KFe}_2\text{As}_2}(\tau)}{\chi^{\text{KFe}_2\text{As}_2}(0)} > \frac{\chi^{\text{LiFeAs}}(\tau)}{\chi^{\text{LiFeAs}}(0)} > \frac{\chi^{\text{BaFe}_2\text{As}_2}(\tau)}{\chi^{\text{BaFe}_2\text{As}_2}(0)} > \frac{\chi^{\text{LaFeAsO}}(\tau)}{\chi^{\text{LaFeAsO}}(0)}.$$

This order can be regarded as a rough estimate of the "degree of correlation" of the respective materials and is (almost) independent of the modelization (d vs dp/dpp) of the Wannier-basis and the used interaction-Hamiltonian. Qualitatively the effects of spin-screening can already be inferred from the decay of $\chi(\tau)$. In particular, we find more correlated electrons to exhibit longer spin-excitation life-times. For a more detailed analysis an analytical continuation is necessary (see Fig. 5.5 and following). Further by comparing the $\chi^{\text{tot}}(\tau)$ (Fig. 5.3) with $\chi^{\text{diag}}(\tau)$ (Fig. 5.4), we find the 20 off-diagonal contributions to outweigh the 5 diagonal ones for $\tau \gtrsim 2$. This is a clear effect of the *Hund's coupling*. We must also note that while the spin-spin-susceptibility must fulfill $\frac{d^2}{d^2\tau}\chi^{\text{diag}}(\tau) \geq 0$ and $\frac{d^2}{d^2\tau}\chi^{\text{tot}}(\tau) \geq 0$ there is no convex/concave-requirement for the off-diagonal terms (see sec. 2.3.1), except $\frac{d^2}{d^2\tau}\chi^{\text{offdiag}}(\tau) \geq -\frac{d^2}{d^2\tau}\chi^{\text{diag}}(\tau)$ of course. For small τ the diagonal contribution outweighs the off-diagonal one for Kanamori- and full- U -interaction. For density-density-type-interaction the situation appears, in some cases, reversed. Moreover, in this case, the off-diagonal contribution seems to be less τ -dependent in general. Since a constant $\chi(\tau)$ would correspond to a renormalized delta-peak at $\omega = 0$ (which would again correspond to an magnetic moment with infinite life-time; see sec. 2.3.3) one may assume that the off-diagonal-terms, are to a large extent responsible for the formation of a local magnetic moment. The importance of the off-diagonal terms hints, moreover, that the parent-compounds of Fe-based superconductors are J -dominated. This is further evidence that they are *Hunds*-metals.

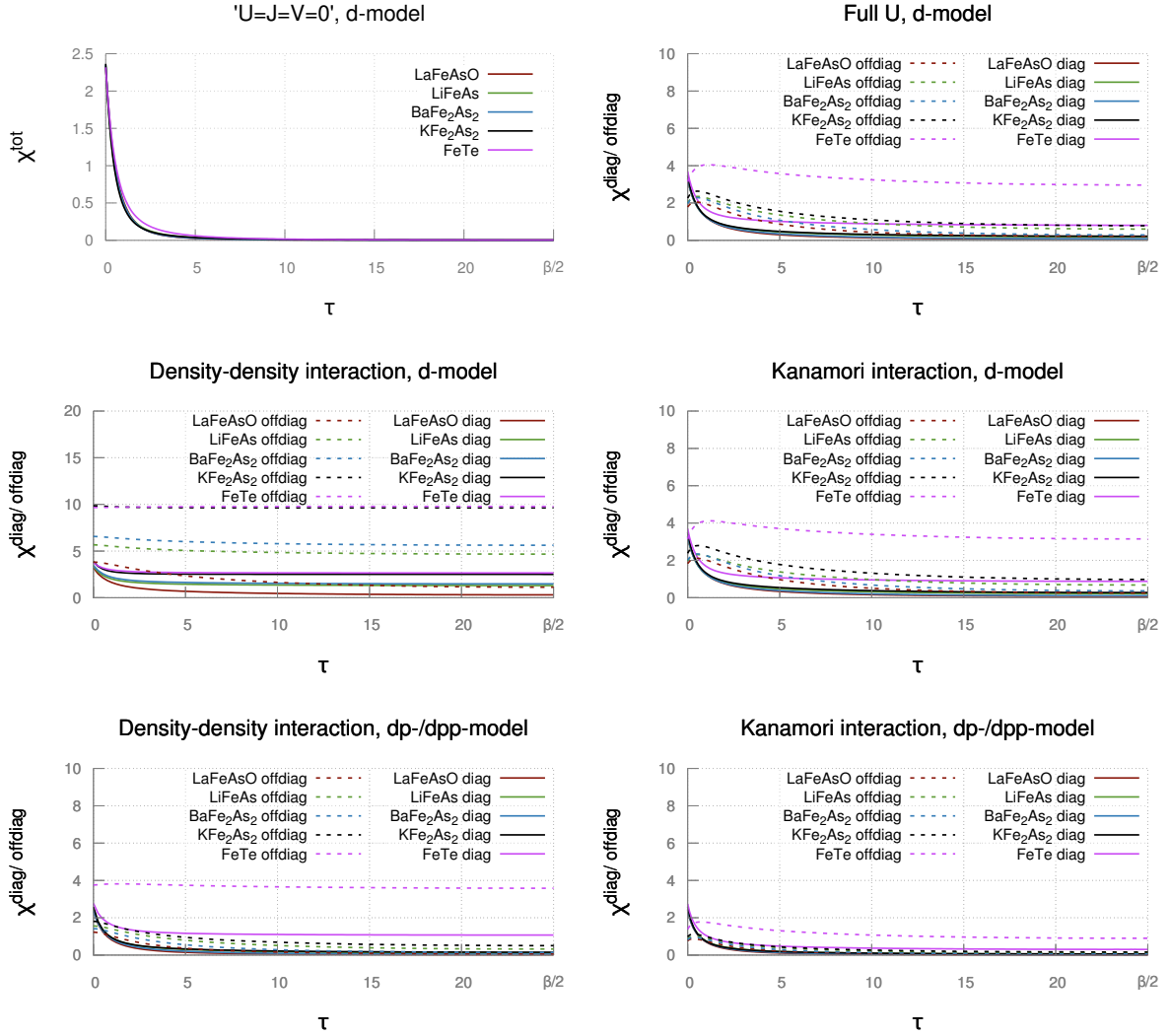


Figure 5.4: Comparison of the spin-spin-susceptibility in imaginary time for the different materials under consideration. Note the different scale for " $U=0$ " (top-left figure) and "Density-density, d -model" (mid-left figure).

In Fig. 5.5 we see a comparison of $\text{Im } \chi^{\text{tot}}(\omega)$ on the real frequency-axis (after the analytical continuation). It is not surprising that the "non-interacting case" displays a rather featureless spread out over the whole bandwidth (approximately 4eV). At the same time, if the interaction is included, we find the formation of local magnetic momentum features. More specifically a low-frequency peak forms. The more *correlated* a material is the more *narrow* the peak seems to be. Moreover, the location of the peak follows a definite trend, *moving to smaller energies* for more correlated materials. Regarding the different models and interactions we find "*full U*" to agree well with Kanamori (both in the d -model). The results for FeTe in density-density-

interaction don't agree very well with the Kanamori-results, neither in the d -model nor in the $dp - /dpp$ -model, with a difference much more severe than for the other materials. While the overall functions, in some case, display also *separated* high energy peaks, we believe these are most likely an artifact of the MEM procedure. For example for FeTe with Kanamori-interaction in the dp -model the second peak at 0.35meV, separated from the first one by a large gap, is unphysical.

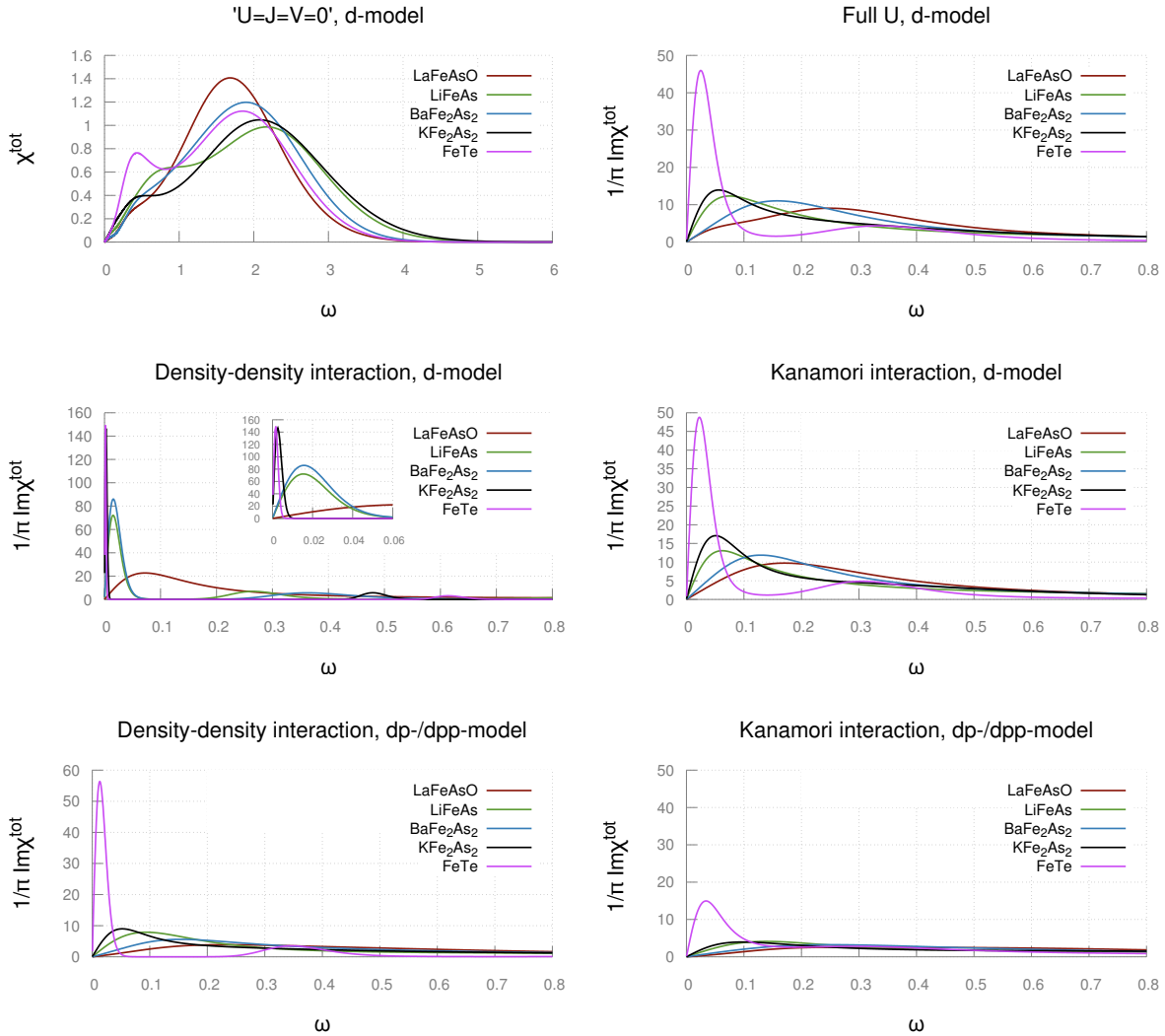


Figure 5.5: Comparison of the spin-spin-susceptibility in real frequencies with respect to the materials. (Obtained via MaxEnt)

The position as well as the width of the peaks in $\chi(\omega)$ correspond to time-scales of the spin-spin-correlation function. It is, however, not clear which one is dominant for each material.

To answer this question we have fitted a model to the peaks of the *full U* calculation to extract more quantitative results regarding the time scales. The results of this extra analysis are summarized in Tab. 5.1. Details regarding the fitting procedure can be found in the previous chapter (e.g. section 4.1.3).

As additional information for the fit we note that there are two qualitative different solutions of the Fourier-transform for the fitted model (under consideration of the KK-relation) depending on the relation between ω_0 and γ :

- underdamped regime:

$$\chi(t) = a\theta(t) \frac{e^{-\gamma t}}{\sqrt{\omega_0^2 - \gamma^2}} \sin(t\sqrt{\omega_0^2 - \gamma^2}) \quad \text{for } \omega_0^2 > \gamma^2 \ (\leftrightarrow t_{\omega_0} < t_\gamma)$$
- overdamped regime:

$$\chi(t) = a\theta(t) \frac{e^{-\gamma t}}{\sqrt{\gamma^2 - \omega_0^2}} \sinh(t\sqrt{\gamma^2 - \omega_0^2}) \quad \text{for } \omega_0^2 < \gamma^2 \ (\leftrightarrow t_{\omega_0} > t_\gamma)$$

(5.1)

To highlight the relevant damping time-scale we used a bold font in Tab.5.1. As seen from the above equations, $\chi(t)$ does not oscillate with ω_0 , but with an oscillation-frequency of $\omega = \sqrt{|\omega_0^2 - \gamma^2|}$. If the system is in the overdamped regime, observes thus an effective time-scale:

$$\chi(t) = a\theta(t) \frac{e^{-\gamma t}}{\sqrt{\gamma^2 - \omega_0^2}} \sinh(t\sqrt{\gamma^2 - \omega_0^2}) \propto e^{-t(\gamma - \sqrt{\gamma^2 - \omega_0^2})} \equiv e^{-t/t_{\tilde{\gamma}}}. \quad (5.2)$$

In the overdamped regime, this timescale is always the most relevant one for large times . One should also be aware of the relation between t_γ and t_ω . If $t_\omega < t_\gamma$ the *fluctuations could be misinterpreted as a damping*. For example see Fig. 5.7 for *LiFeAs* and for *KFe₂As₂* (for full U) there is a rapid decay at the beginning, but they get damped over a significantly longer timescale that the first few femtoseconds would suggest. E.g. for *LiFeAs* fluctuations occur at a time-scale of ≈ 1.7 fs, whereas the damping is on a timescale of ≈ 9.1 fs. Evidently, the shorter timescale should be considered when interpreting the results of an experimental spectroscopic probe with different time/energy resolutions. In Fig. 5.6 the retarded spin-spin-commutation correlation function is shown.

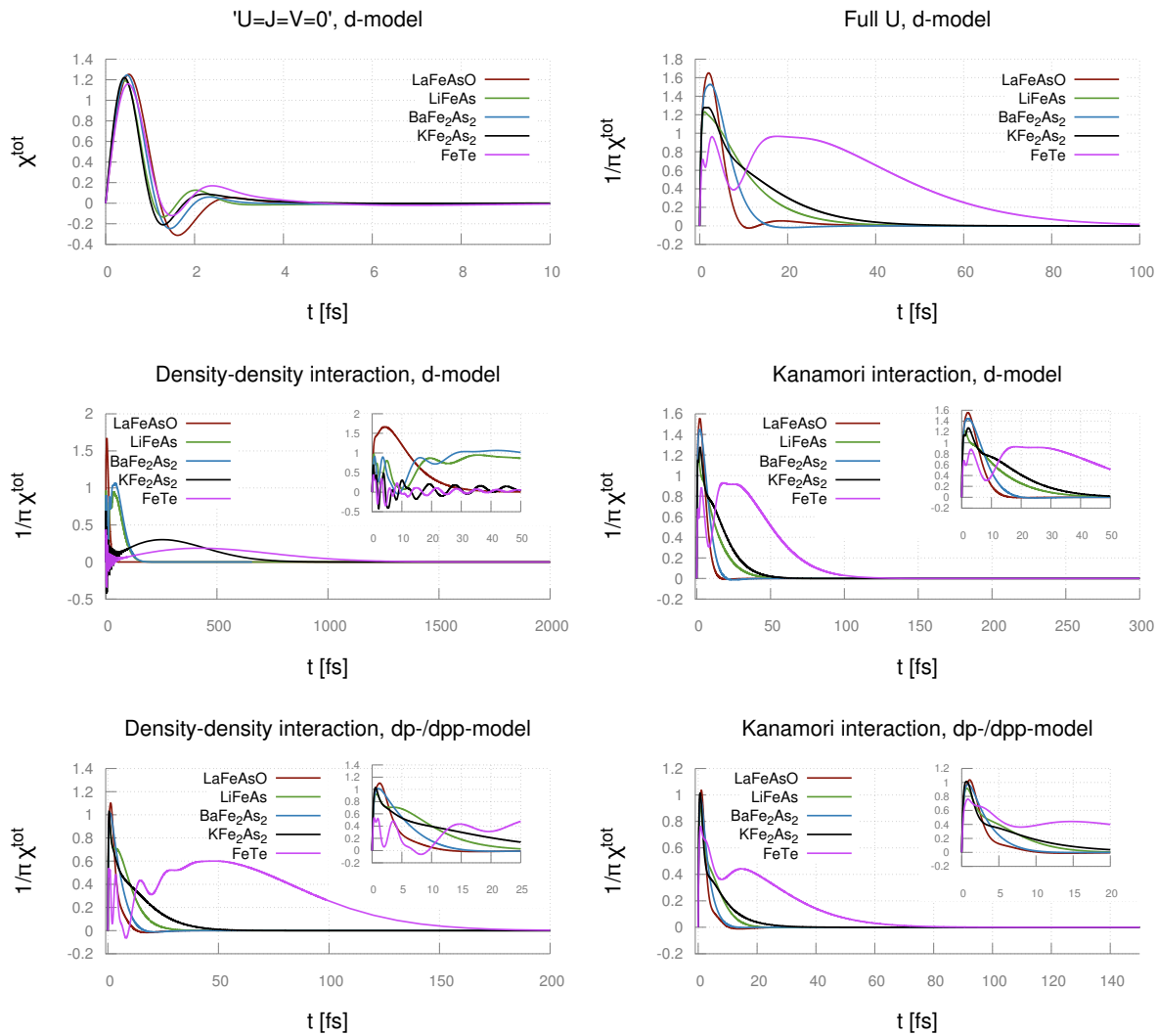


Figure 5.6: Comparison of the spin-spin-susceptibility in real time with respect to the materials.

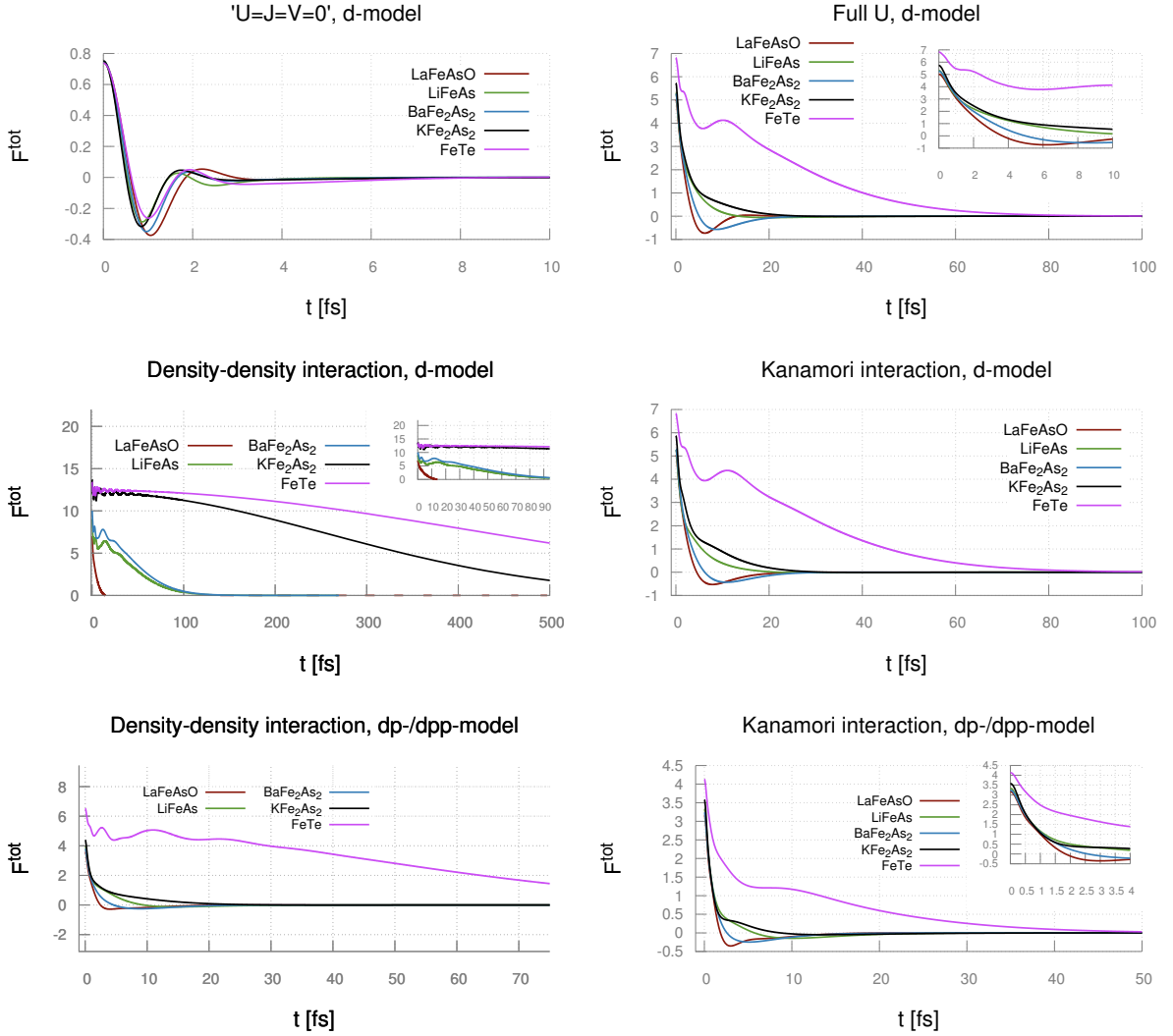


Figure 5.7: Comparison of the spin-spin-susceptibility in real time with respect to the materials.

Since in the linear response theory $\chi(t = 0) = 0$, per construction, the spin-screening processes (oscillation and damping) can be better visualized in the correlation function $F(t)$, which is symmetric with respect to time (due to time-translation invariance $\langle \hat{O}_i(t)\hat{O}_j(0) \rangle = \langle \hat{O}_i(0)\hat{O}_j(-t) \rangle$).¹

Comparing the fitted time-scales to the Fig. 5.7, we find good agreement regarding t_γ . The other time-scales are less easily estimated from the $F(t)$ data, but nonetheless, an overall qualitative agreement can be noticed. The progressive shift of the peaks (more correlated materials have their $\text{Im } \chi(\omega)$ peak at lower frequencies) is rather evident from the first row in Tab. 5.1. The corresponding timescale $t_{\text{max peak}} = \hbar/\omega_{\text{max peak}}$ is given in the second column. This timescale

¹Proves of the symmetries are given in sec. 2.3.1.

		LaFeAsO	BaFe ₂ As ₂	LiFeAs	KFe ₂ As ₂	FeTe
$\omega_{\max \text{ peak}_1}$	[meV]	248.83	157.42	75.15	56.25	24.46
$t_{\max \text{ peak}_1}$	[fs]	2.64	4.18	8.75	11.70	26.90
t_{γ_1}	[fs]	2.32	2.61	-	-	23.94
t_{ω_1}	[fs]	3.40	7.96	1.71	0.571	31.08
$t_{\tilde{\gamma}_1}$	[fs]	-	-	9.13	12.14	-
$\omega_{\max \text{ peak}_2}$	[eV]	-	-	-	-	322.76
$t_{\max \text{ peak}_2}$	[fs]	-	-	-	-	2.03
t_{γ_2}	[fs]	-	-	-	-	5.92
t_{ω_2}	[fs]	-	-	-	-	1.93
$t_{\tilde{\gamma}_2}$	[fs]	-	-	-	-	-

Table 5.1: Peak-locations of the MaxEnt data and timescales of the fits for all considered materials with *full* U -interaction in the d -model. The subscript 1/2 corresponds to the first/second peak.

$t_{\max \text{ peak}}$ is been sometimes used as an rough estimate for the spin-excitation lifetime t_γ . Our detailed analysis shows that t_γ sometimes agrees well with $t_{\max \text{ peak}}$, but not always. E.g., for $BaFe_2As_2$ the difference is about 60 %. It is unclear why we get reasonably good agreement between t_γ and $t_{\max \text{ peak}}$ for the other material. The expected material trend is, however, never

In the *full* U case, we find an interesting behavior. While some materials are in the overdamped regime ($LiFeAs$ and KFe_2As_2) the others are not. While in the underdamped regime the oscillation-timescale is always larger than the damping-timescale, the ratio t_ω/t_γ varies considerably. In fact, from the table of timescales (Tab. 5.1) and consistent with the numerical Fourier-transformed results (Fig. 5.6 and 5.7) we find that *damping* (width of the peaks) to be *more important* than the *oscillation frequencies*. This reflects the physical situation where only a small number of oscillations can take place before $\chi(t)$ and $F(t)$ are damped completely. Only on a *very short timescales* (for some of the materials less than 2 fs in $F(t)$) a large *local magnetic moment is present*.

Another important result, in the view of comparison to experiments, is the estimation of the local magnetic moment. Since we are in the paramagnetic phase we can assume isotropy in all directions. In fact, we recall that $m = g\sqrt{\langle S_x^2 \rangle + \langle S_y^2 \rangle + \langle S_z^2 \rangle} = \sqrt{3\langle S_z^2 \rangle} = \sqrt{3\chi^{\text{tot}}(\tau = 0)}$.

However, looking at Tab. 5.2 we observe something peculiar occurs for several materials. The maximum value of an effective spin in Fe with 6 d -electrons is $S_{\text{eff}}^{\text{max}} = 2$. This would give an upper bound to the local magnetic moment of $m_{\text{loc}}^{\text{max}} = g\sqrt{S_{\text{eff}}^{\text{max}}(S_{\text{eff}}^{\text{max}} + 1)}\mu_B = 2\sqrt{6}\mu_B \approx 4.9\mu_B$. In the table, however, the left column (H_{loc}^D) there are values greater than this upper bound. It should, however, be taken into account that isotropy is actually only given for a $SU(2)$ symmetric Hamiltonian. For our density-density calculations this symmetry is broken. In a density-density calculation not all directions are equally treated on, contrary to what we would expect for a material in the paramagnetic phase. For the least correlated material,

$m = \sqrt{3\chi(0)}$ [μ_B]	d-model			dp- / dpp-model with FLL DCC		Experiment
	H_U^D	H_U^K	$H_{FLL}^{\text{full}U}$	H_U^D	H_U^K	
LaFeAsO	3.88	3.89	3.88	3.29	3.08	0.3-0.6
BaFe ₂ As ₂	5.48	3.99	3.97	3.72	3.12	0.89
LiFeAs	5.21	3.98	3.99	3.47	3.16	0.9
KFe ₂ As ₂	6.42	4.20	4.15	3.63	3.28	-
FeTe	6.35	4.53	4.53	4.43	3.52	2.2

Table 5.2: Local magnetic moment m for all materials, models and Hamiltonians in units of μ_B . The experimental values shown in the right column are from [14],[15],[16] and[41]. For KFe_2As_2 no data was found.

LaFeAsO, this issue can be safely neglected since the SU(2) symmetric Kanamori-results are almost identical to the density-density-results. In fact the difference between the magnetic moment estimates is minimal: 3.88 instead of 3.89. This posteriori justifies the usage of a density-density-interaction term for *LaFeAsO* in the d -only model. Comparing the value for *LaFeAsO* to the previous results for a 4-orbital calculation[10], we find a good agreement ($3.68\mu_B$ vs. 3.88 - $3.89 \mu_B$). For all the other materials considered, however, we extract an unphysically large local magnetic moment. We must conclude, then, that for these materials the usage of a density-density interaction was not justified.

In the $dp - /dpp$ -model, the differences between Kanamori- and density-density-interaction are less severe. No unphysical results occur there, and by comparing the second- with the third column in Tab.5.2, we find *full U* to agree very well with Kanamori-calculations in the d -model. The $dp - /dpp$ -model gives in general smaller values for the local magnetic moment than the d -model. This is also consistent with the increased filling in the d -orbitals. The estimated filling of all materials in the dp -models were larger than 7 electrons, which correspond, for a perfect (Hund's) alignment to a maximum spin configuration of $S_{\text{max}} = 3/2$, whereas for in the d -only model the filling is 6 electrons, corresponding to $S_{\text{max}} = 2$.

The last remaining step is the comparison to experiments. Experimentally reported values for the local magnetic moment for different sources (references in the capture of Tab.5.2) are shown. They don't agree with our results, but our analysis can justify this disagreement. In fact, on basis of our findings we relate this to the limited energy-range Ω of the INS experiments. Typical experimental bounds are $\Omega = 100\text{meV}$. The rigorous determination of a local magnetic moment would require instead the integration, not up to 100eV, but up to infinity:

$$m_{\text{loc}} = g\sqrt{3 \int_{-\infty}^{\infty} d\omega \frac{1}{\pi} \frac{\text{Im} \chi(\omega)}{1 - e^{-\beta\omega}}}$$

This energy limitation is the cause for the difference between our calculated values and the experimentally found local magnetic moment. Moreover, looking at Tab.5.2 we find another interesting feature missing in the previous studies[10]. The relative disagreement between the experiment and the calculated values decreases the more correlated a material is.

We can explain this by the shift of the peaks: The more correlated a material is, the further its spin-excitation peak "move" to lower energies. (see Fig.5.5). Thus, the more spectral

weight (of the spin-susceptibility) is shifted into the observational window available to experiments. Our results show that from an qualitative point of view the experimental trend can be undermined. Moreover, one can now compare our quantitative results $\text{Im}\chi(\omega)$ to the INS measurements for a further close comparison of the experimental results all materials with the theoretical calculation up to a finite-cutoff frequency.

Chapter 6

Conclusions and outlook

Calculating one- and two-particle properties for strongly correlated materials in an ab-initio approach is a challenging but also valuable task. In fact, especially, in the case of realistic (multi-orbital) systems, the correlation effects may appear very different at the one- and two-particle level. This also applies to the systems of interest in this work, the *Fe-SC*, for which a full understanding of their unconventional superconductivity and the interplay between spin and orbital degrees of freedom appears particularly rich and interesting. In fact, especially in this Master thesis, we first discuss, our DFT+DMFT results for the self-energies $\Sigma(i\omega_n)$ and the one-particle spectral function $\mathcal{A}(\omega)$ which for all the analyzed Fe-based SC (parent compounds) show a (moderately corrected) metallic behavior. At the two-particle level, on the other hand, we found the formation of a large local magnetic moment for all materials subject to dynamically screening processes of different intensities. Comparing the $\chi^{\text{off-diag}}(\tau)$ to $\chi^{\text{diag}}(\tau)$ we found that the off-diagonal terms outweigh the diagonal ones, indicating the importance of the *Hund's* coupling J . This reflects the facts that the physics of the parent compounds of all of the considered families are well described by a local magnetic moment in a metallic background of itinerant electrons (*Hund's* metals)[42].

By analyzing the family-dependent spin-spin susceptibility $\text{Im} \chi(\omega)$ we found the major spectral weight (of $\text{Im} \chi(\omega)$) to be located at smaller energies for more correlated materials. Qualitatively, this matches very well the proposed solution [10][43][44] for the *big moment puzzle* (See section 5) and represents one of the main results of this master thesis. For a more qualitative analysis, of the underlying physics, we extracted the time-scales from the dissipative part of the spin-spin-susceptibility. We found that the "damping-timescale" t_γ , corresponding to the peak-width, dominates over the oscillation frequency t_ω . We showed, moreover, that while some materials are in the oscillating "underdamped" parameter regime, others are in the "overdamped" parameter regime, where not even a full spin-oscillation period can be completed. This would suggest that the picture of a strongly fluctuation long-lived magnetic excitation should be replaced by a short-lived weakly oscillating magnetic excitation.

The present results evidentially call for an cooperative reexamination of the INS-measurements for all the Fe-SC and an extension of the measurements of the spin-susceptibility to larger energy windows.

Bibliography

- [1] Onnes, K. (1911) Further experiments with liquid helium. C. On the change of electric resistance of pure metals at very low temperatures, etc. IV. The resistance of pure mercury at helium temperatures.. *Comm. Phys. Lab.*, **120**, b.
- [2] Bardeen, J., Cooper, L. N., and Schrieffer, J. R. (Apr, 1957) Microscopic Theory of Superconductivity. *Phys. Rev.*, **106**, 162–164.
- [3] Bednorz, J. G. and Müller, K. A. (Jun, 1986) Possible highTc superconductivity in the Ba-La-Cu-O system. *Zeitschrift für Physik B Condensed Matter*, **64**(2), 189–193.
- [4] Kamihara, Y., Hiramatsu, H., Hirano, M., Kawamura, R., Yanagi, H., Kamiya, T., and Hosono, H. (2006) Iron-Based Layered Superconductor: LaOFeP. *Journal of the American Chemical Society*, **128**(31), 10012–10013 PMID: 16881620.
- [5] Conder, K. (2016) A second life of the Matthias’s rules. *Superconductor Science and Technology*, **29**(8), 080502.
- [6] Chubukov, A. and Hirschfeld, P. J. (2015) Iron-based superconductors, seven years later. *Physics Today*, **68**(6), 46–52.
- [7] Sidis, Y., Pailhès, S., Hinkov, V., Fauquè, B., Ulrich, C., Capogna, L., Ivanov, A., Regnault, L.-P., Keimer, B., and Bourges, P. (09, 2007) Inelastic neutron scattering study of spin excitations in the superconducting state of high temperature superconductors. **8**, 745–762.
- [8] Hosono, H., Tanabe, K., Takayama-Muromachi, E., Kageyama, H., Yamanaka, S., Kumakura, H., Nahara, M., Hiramatsu, H., and Fujitsu, S. (2015) Exploration of new superconductors and functional materials and fabrication of superconducting tapes and wires of iron pnictides.
- [9] Wang, M., Zhang, C., Lu, X., Tan, G., Luo, H., Song, Y., Wang, M., Zhang, X., Goremychkin, E. A., Perring, T. G., Maier, T. A., Yin, Z., Haule, K., Kotliar, G., and Dai, P. (Dec, 2013) Doping dependence of spin excitations and its correlations with high-temperature superconductivity in iron pnictides. *Nature Communications*, **4**, 2874 EP – Article.
- [10] Toschi, A., Arita, R., Hansmann, P., Sangiovanni, G., and Held, K. (Aug, 2012) Quantum dynamical screening of the local magnetic moment in Fe-based superconductors. *Phys. Rev. B*, **86**, 064411.
- [11] Haule, K. and Kotliar, G. (2008) Coherence-incoherence crossover in the normal state of iron-oxypnictides and importance of the Hund’s rule coupling.

- [12] Mostofi, A. A., Yates, J. R., Pizzi, G., Lee, Y.-S., Souza, I., Vanderbilt, D., and Marzari, N. (2014) An updated version of wannier90: A tool for obtaining maximally-localised Wannier functions. *Computer Physics Communications*, **185**(8), 2309 – 2310.
- [13] Li, Y., Wang, W., Song, Y., Man, H., Lu, X., Bourdarot, F., and Dai, P. (2017) Spin excitation anisotropy in the paramagnetic tetragonal phase of BaFe₂As₂.
- [14] Ishida, K., Nakai, Y., and Hosono, H. (2009) To What Extent Iron-Pnictide New Superconductors Have Been Clarified: A Progress Report. *Journal of the Physical Society of Japan*, **78**(6), 062001.
- [15] Qureshi, N., Drees, Y., Werner, J., Wurmehl, S., Hess, C., Klingeler, R., Büchner, B., Fernández-Díaz, M. T., and Braden, M. (Nov, 2010) Crystal and magnetic structure of the oxypnictide superconductor LaFeAsO_{1-x}F_x: A neutron-diffraction study. *Phys. Rev. B*, **82**, 184521.
- [16] Huang, Q., Qiu, Y., Bao, W., Green, M. A., Lynn, J. W., Gasparovic, Y. C., Wu, T., Wu, G., and Chen, X. H. (Dec, 2008) Neutron-Diffraction Measurements of Magnetic Order and a Structural Transition in the Parent BaFe₂As₂ Compound of FeAs-Based High-Temperature Superconductors. *Phys. Rev. Lett.*, **101**, 257003.
- [17] Abrikosov, A., Gorkov, L., and Dzyaloshinski, I. (1975) *Methods of Quantum Field Theory in Statistical Physics*, Dover Books on Physics SeriesDover Publications, .
- [18] Parragh, N. Strongly Correlated Multi-Orbital Systems : A Continuous-Time Quantum Monte Carlo Analysis doctoralthesis Universität Würzburg (2013).
- [19] Wallerberger, M., Hausoel, A., Gunacker, P., Kowalski, A., Parragh, N., Goth, F., Held, K., and Sangiovanni, G. w2dynamics: Local one- and two-particle quantities from dynamical mean field theory. (2018).
- [20] Hafner J., K. G. (1997) The Vienna AB-Initio Simulation Program VASP: An Efficient and Versatile Tool for Studying the Structural, Dynamic, and Electronic Properties of Materials. In: Gonis A., Meike A., Turchi P.E.A. (eds) *Properties of Complex Inorganic Solids*, Springer, .
- [21] Miyake, T., Nakamura, K., Arita, R., and Imada, M. (2009) Comparison of Ab initio Low-Energy Models for LaFePO, LaFeAsO, BaFe₂As₂, LiFeAs, FeSe and FeTe: Electron Correlation and Covalency.
- [22] Pavarini, E., Koch, E., Vollhardt, D., and Lichtenstein, A. E. . (2011) The LDA+DMFT approach to strongly correlated materials: lecture notes of the autumn school 2011, hands-on LDA+DMFT ; autumn school organized by the DFG research unit 1346 dynamical mean-field approach with predictive power for strongly correlated materials at Forschungszentrum Jülich 4-7 October 2011, Vol. 1 of *Schriften des Forschungszentrums Jülich*. Reihe Modeling and simulation, Forschungszentrum, Zentralbibliothek, Jülich Record converted from JUWEL: 18.07.2013.
- [23] J., H. (1963) Electron correlations in narrow energy bands. *Proceedings of the Royal Society of London A: Mathematical, Physical and Engineering Sciences*, **276**(1365), 238–257.

- [24] Georges, A. and Kotliar, G. (Mar, 1992) Hubbard model in infinite dimensions. *Phys. Rev. B*, **45**, 6479–6483.
- [25] Metzner, W. and Vollhardt, D. (Jan, 1989) Correlated Lattice Fermions in $d = \infty$ Dimensions. *Phys. Rev. Lett.*, **62**, 324–327.
- [26] Gull, E., Millis, A. J., Lichtenstein, A. I., Rubtsov, A. N., Troyer, M., and Werner, P. (May, 2011) Continuous-time Monte Carlo methods for quantum impurity models. *Rev. Mod. Phys.*, **83**, 349–404.
- [27] Toschi, A. (2011) Strong Electronic Correlation in Dynamical Mean Field Theory and beyond (Habilitation Thesis), TU Wien, .
- [28] Parragh, N., Toschi, A., Held, K., and Sangiovanni, G. (Oct, 2012) Conserved quantities of $SU(2)$ -invariant interactions for correlated fermions and the advantages for quantum Monte Carlo simulations. *Phys. Rev. B*, **86**, 155158.
- [29] W., S. Y. On definite integrals and functions used in series expansions doctoralthesis St. Petersburg (1873).
- [30] Gubernatis, J. E., Jarrell, M., Silver, R. N., and Sivia, D. S. (Sep, 1991) Quantum Monte Carlo simulations and maximum entropy: Dynamics from imaginary-time data. *Phys. Rev. B*, **44**, 6011–6029.
- [31] Jarrell, M. and Gubernatis, J. (1996) Bayesian inference and the analytic continuation of imaginary-time quantum Monte Carlo data. *Physics Reports*, **269**(3), 133 – 195.
- [32] Otsuki, J., Ohzeki, M., Shinaoka, H., and Yoshimi, K. (2017) Sparse modeling approach to analytical continuation of imaginary-time quantum Monte Carlo data.
- [33] Parragh, N., Sangiovanni, G., Hansmann, P., Hummel, S., Held, K., and Toschi, A. (Nov, 2013) Effective crystal field and Fermi surface topology: A comparison of d- and dp-orbital models. *Phys. Rev. B*, **88**, 195116.
- [34] Hansmann, P., Parragh, N., Toschi, A., Sangiovanni, G., and Held, K. (2014) Importance of d-p Coulomb interaction for high T C cuprates and other oxides. *New Journal of Physics*, **16**(3), 033009.
- [35] Kihou, K., Saito, T., Ishida, S., Nakajima, M., Tomioka, Y., Fukazawa, H., Kohori, Y., Ito, T., Ichi Uchida, S., Iyo, A., Lee, C.-H., and Eisaki, H. (2010) Single Crystal Growth and Characterization of the Iron-Based Superconductor KFe_2As_2 Synthesized by KAs Flux Method. *Journal of the Physical Society of Japan*, **79**(12), 124713.
- [36] Grånäs, O., Marco, I. D., Thunström, P., Nordström, L., Eriksson, O., Björkman, T., and Wills, J. M. (2011) Charge self-consistent dynamical mean-field theory based on the full-potential linear muffin-tin orbital method: methodology and applications.
- [37] Kutepov, A., Haule, K., Savrasov, S. Y., and Kotliar, G. (2010) Self consistent GW determination of the interaction strength: application to the iron arsenide superconductors.
- [38] Aichhorn, M., Pourovskii, L., and Georges, A. (2011) Importance of electronic correlations for structural and magnetic properties of the iron pnictide superconductor $LaFeAsO$. *Physical Review B*, **84**(5), 054529.

- [39] Hausoel, A., Karolak, M., Sasioglu, E., Lichtenstein, A., Held, K., Katanin, A., Toschi, A., and Sangiovanni, G. (2017) Local magnetic moments in iron and nickel at ambient and Earth's core conditions.
- [40] Levy, R., LeBlanc, J. P. F., and Gull, E. (2016) Implementation of the Maximum Entropy Method for Analytic Continuation.
- [41] Gretarsson, H., Lupascu, A., Kim, J., Casa, D., Gog, T., Wu, W., Julian, S. R., Xu, Z. J., Wen, J. S., Gu, G. D., Yuan, R. H., Chen, Z. G., Wang, N. L., Khim, S., Kim, K. H., Ishikado, M., Jarrige, I., Shamoto, S., Chu, J. H., Fisher, I. R., and Kim, Y.-J. (2011) Revealing the dual nature of magnetism in iron pnictides and iron chalcogenides using x-ray emission spectroscopy.
- [42] Haule, K. and Kotliar, G. (2009) Coherence-incoherence crossover in the normal state of iron oxypnictides and importance of Hund's rule coupling. *New Journal of Physics*, **11**(2), 025021.
- [43] Hansmann, P., Arita, R., Toschi, A., Sakai, S., Sangiovanni, G., and Held, K. (May, 2010) Dichotomy between Large Local and Small Ordered Magnetic Moments in Iron-Based Superconductors. *Phys. Rev. Lett.*, **104**, 197002.
- [44] Liu, M., Harriger, L. W., Luo, H., Wang, M., Ewings, R. A., Guidi, T., Park, H., Haule, K., Kotliar, G., Hayden, S. M., and Dai, P. (2012) Nature of magnetic excitations in superconducting $\text{BaFe}_{1.9}\text{Ni}_{0.1}\text{As}_2$.